ISSN: 2376-2136 (Print)
ISSN: 2376-2144 (Online)

Trends in Renewable Energy

Volume 5, Issue 3, December 2019

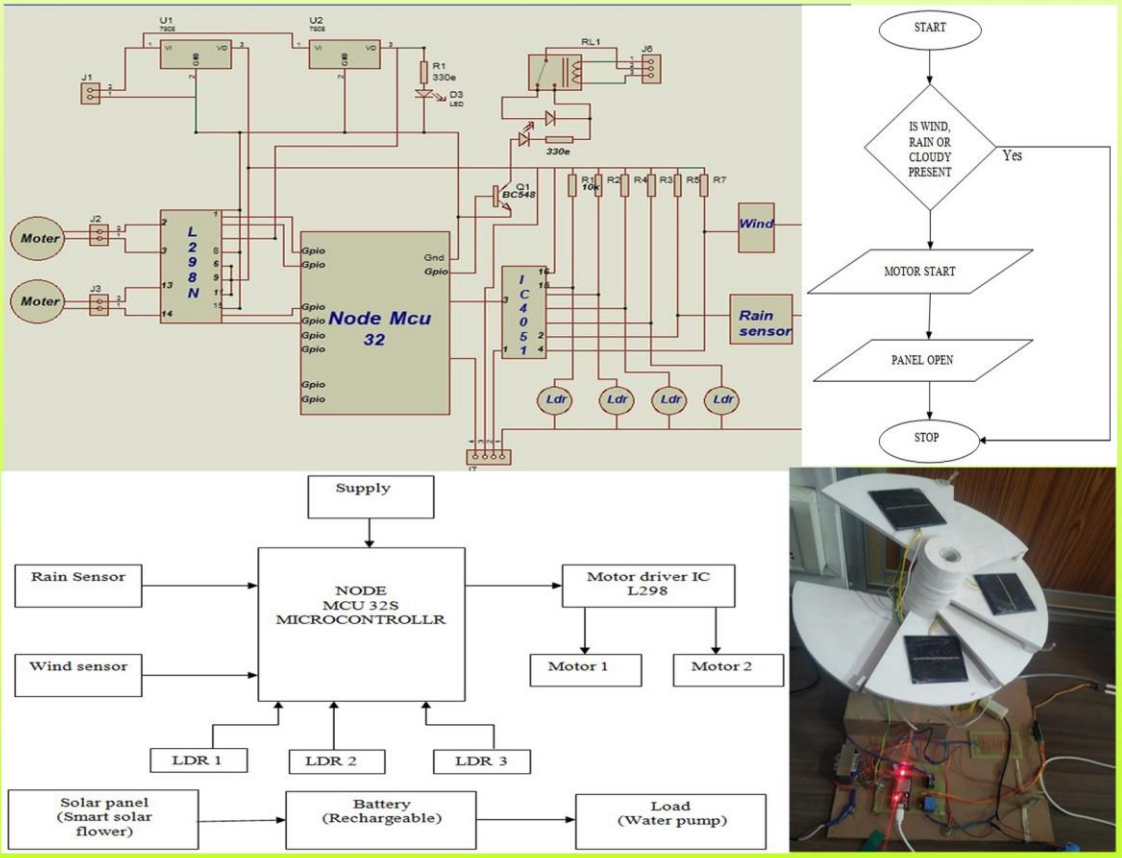

Cover image: IoT based smart solar flower water pump system, see article by Band and Ingole in this issue.

futureenergysp.com
thefutureenergy.org

Trends in Renewable Energy

ISSN: 2376-2136 (Print) ISSN: 2376-2144 (Online)

http://futureenergysp.com/

Trends in Renewable Energy is an open accessed, peer-reviewed semi-annual journal publishing reviews and research papers in the field of renewable energy technology and science.

The aim of this journal is to provide a communication platform that is run exclusively by scientists working in the renewable energy field. Scope of the journal covers: Bioenergy, Biofuel, Biomass, Bioprocessing, Biorefinery, Biological waste treatment, Catalysis for energy generation, Energy conservation, Energy delivery, Energy resources, Energy storage, Energy transformation, Environmental impact, Feedstock utilization, Future energy development, Green chemistry, Green energy, Microbial products, Physico-chemical process for Biomass, Policy, Pollution, Renewable energy, Smart grid, Thermo-chemical processes for biomass, etc.

The Trends in Renewable Energy publishes the following article types: peer-reviewed reviews, mini-reviews, technical notes, short-form research papers, and original research papers.

The article processing charge (APC), also known as a publication fee, is fully waived for the Trends in Renewable Energy.

Editorial Team of Trends in Renewable Energy

EDITORIAL BOARD

Dr. Utkucan Şahin	Assistant Prof., Department of Energy Systems Engineering, Faculty of Technology, Muğla Sıtkı Koçman University, Turkey
Dr. ALIASHIM ALBANI	School of Ocean Engineering, Universiti Malaysia Terengganu, Malaysia
Dr. Ashwini Kumar	Assistant Prof., College of Engineering, HSBPVT's Parikrama Group of Institutions, India
Dr. Hasan AYDOGAN	Associate Prof., Mechanical Engineering Department, Selcuk University, Turkey
Dr. Jiekang Wu	Professor, School of Automation, Guangdong University of Technology, China
Dr. Ong Huei Ruey	DRB-HICOM University of Automotive, Malaysia
Dr. Miguel Ángel Reyes Belmonte	IMDEA Energy Institute, Spain
Dr. Chitra Venugopal	Associate Professor in Electrical Engineering, University of Trinidad and Tobago, Trinidad
Dr. Amit Kumar Singh	Assistant Prof., Instrumentation & Control Engineering Department, Dr. B.R.A. National Institute of Technology, India
Dr. Suvanjan Bhattacharyya	University of Pretoria, South Africa
Dr. Karunesh Tiwari	Babu Banarasi Das University, India
Dr. Sharadrao A. Vhanalkar	Karmaveer Hire Arts, Science, Commerce and Education College, India
Dr. Prasenjit Chatterjee	Assistant Prof. and Head, MCKV Institute of Engineering, India
Dr. S. Balamurugan	Mindnotix Technologies, India
Dr. Mohammad Nurunnabi	University of Oxford, United Kingdom
Dr. Kenneth Okedu	Caledonian College of Engineering, Oman
Dr. Cheng Zhang	Sr. Materials Engineer, Medtronic, Inc., United States
Dr. Chandani Sharma	Assistant Prof., Department of Electrical Engineering, Graphic Era University, India
Dr. Kashif Irshad	Assistant Prof., Mechanical Engineering Department, King Khalid University, Saudi Arabia
Dr. Abhijit Bhagavatula	Principal Lead Engineer, Southern Company Services, United States
Dr. S. Sathish	Associate Prof., Department of Mechanical Engineering, Hindustan University, India
Mr. A. Avinash	Assistant Prof., KPR Institute of Engineering & Technology, India
Mr. Bindeshwar Singh	Assistant Prof., Kamla Nehru Institute of Technology, India
Dr. Yashar Hashemi	Tehran Regional Electric Company, Iran
Dr. Navanietha Krishnaraj R	South Dakota School of Mines and Technology, United States
Dr. SANDEEP GUPTA	JECRC University, India
Dr. Shwetank Avikal	Graphic Era Hill University, India
Dr. Xianglin Zhai	Poochon Scientific LLC, United States
Dr. Rui Li	Assistant Prof., College of Engineering, China Agricultural University, China
Dr. Adam Elhag Ahmed	National Nutrition Policy Chair, Department of Community Services, College of Applied Medical Sciences, King Saud University, Saudi Arabia
Dr. Jingbo Li	Massachusetts Institute of Technology, United States
Dr. Srikanth Mutnuri	Associate Prof., Department of Biological Sciences, Associate Dean for International Programmes and Collaboration, Birla Institute of Technology & Science, India
Dr. Bashar Malkawi	S.J.D., Associate Prof., College of Law, University of Sharjah, United Arab Emirates
Dr. Simona Silvia Merola	Istituto Motori - National Research Council of Naples, Italy
Dr. Hakan Caliskan	Faculty of Engineering, Department of Mechanical Engineering, Usak University, Turkey

Table of Contents

Volume 5, Issue No. 3, December 2019

Articles

IoT Based Smart Solar Flower Water Pump System

Prof B H Band[1*], Prof A D Ingole[2]

1: Assistant Professor, Electrical Engineering Department, PRMCEAM, Badnera, Maharashtra, India
2: Assistant Professor, Electronics and Tele-communication Engineering Department, PRMCEAM, Badnera, Maharashtra, India

Received June 11, 2019; Accepted July 18, 2019; Published July 26, 2019

The electric demand of the countries is increasing day by day and the available resources are quite insufficient to fulfill this demand. The reasons are that the conventional energy resources are diminishing and available with finite sources. Due to these reasons, the solar power is one of the promising alternatives that is easily available, pollution free and having higher operating life. The solar system also provides higher operating efficiency for the load, and the cost of the solar panel is minimum. To improve the switching technology used for the power conversion, we presented a smart flower system powered by photovoltaic panels that could supply standalone AC/DC load. In this system, solar panels produce a direct current, which can be converted into AC by the converter and used in home, industrial and agriculture applications. The output of the panels depends on the direction of sun's rays (solar energy), and the solar photovoltaic cell converts the solar energy into useful electrical energy. The aim of this paper is to develop the solar photovoltaic generation system based on a standard power electronics cell for micro industrial, commercial, home as well as agriculture applications. The proposed system is capable to provide protection from wind and rain, thereby the efficiency of the solar panels will increase. The generation of the electricity is more with trackers than stationary counterparts due to direct exposure to sun's rays. This increase can be as much as 25% depending upon the geographic location of the tracking system. The generated output voltage can be used for various purposes, and we used the store energy to run an agriculture water pump by using the internet of things (IoT).

Keywords: Solar Flower; Energy Generation; IoT; Water Pump; Motor; Solar Tracker

1. Introduction

The smart flower was named after its design, in which the solar cells are arranged on individual “petals” that open at the beginning of each day and look like a flower (https://news.energysage.com/smartflower-solar-complete-review/). After the sun sets, the petals of the smart flower fold up and the self-cleaning process begins. The smart flower system includes a dual-axis tracker that allows the petals to follow the sun through the sky throughout the day. According to smart flower’s survey, with this tracking feature, the smart flower system can generate 40% more electricity than a rooftop solar panel system of the same size. The smart flower system has the same solar power benefits as a regular solar system, as well as an integrated battery that provides more energy storage.

Corresponding author: bhushanband@gmail.com

Tr Ren Energy, 2019, Vol. 5, No.3, 229-236. doi: 10.17737/tre.2019.5.3.0098

It has been more than fifteen years since the term of Internet of Things (IoT) was introduced to the public. It is basically used to connect living and non living things with each other through the internet. IoT allows people and things to be connected anytime, anyplace, with anything and anyone, by using ideally in any path/network and any service.

As the non-renewable energy resources are decreasing, the use of renewable resources for producing electricity is increasing. Solar panel absorbs the energy from the Sun, converts it into electrical energy and stores the energy in a battery. This energy can be utilized when required or can be used as a direct alternative to the grid supply. The energy stored in batteries can be utilized for the agriculture pump. The coming sun's rays is varying in different directions due to the rotation of the Earth. For an efficient usage of the solar energy, the solar panels should absorb energy to a maximum extent. This can be done only if the panels are continuously placed towards the direction of the Sun. So, solar panels should continuously rotate in the direction of sun as we are introducing the smart flower with it.

2. Literature Review

In recent year, the solar energy system is one of the most popular things for the homes and also for the business in India. Believe it or not, this desire to use the Sun to power people's electricity needs is anything but new. Ever since scientists discovered materials that can produce the electrical current by simply being exposed to the light, people have been excited about this energy source. This article outlines the details of solar power generation and the expanding world.

The operating principles for modern photovoltaic (PV) cells were first discovered in 1839 by a French physicist named A.E. Becquerel. After that, a number of scientists played with and improved on Becquerel's original discovery. This technology soon found its way back down to earth for use in telecommunications applications in remote areas. People began using PV modules to charge batteries from the year 1970s and 1980s and then used these batteries to run various appliances in their remote homes. These discoveries help the people in today's environment [1, 2].

The first PV module isn't sufficient for various applications. They were also quite costly. Yet over the years, researchers and manufacturing companies increased efficiencies and reliability and managed to drive down costs drastically. All of these contributions have led to the widespread use of solar modules and their availability to you and me. In the following sections, we describe some common PV applications, a few brief pros and cons of PV systems, and the future of the PV industry.

The improvement in the PV systems can be found in a wide variety of applications, such as the power calculators, pump water, help offset the energy used by floodlights along highways, and, of course, power homes and businesses [3, 4].

The smart flower at the University of Applied Sciences Kufstein (FH Kufstein, Austria), also known as the 'FH smart flower', fulfills multiple purposes. The power generated from the FH smart flower is fed into the school's electrical grid and is also used as a tool for teaching in the discipline of applied energy data management. Its location in the city park makes it not only an eye catcher for employees and tourists, but also a catalyst for conversation about photo voltaic between students of all disciplines and their peers in the energy management program (https://www.pfisterenergy.com/

smartflower/). The smart flower has several photovoltaic panels that fan out like the petals of a flower during the day to capture energy from the Sun. Since solar panels are more efficient when they are pointed directly at the Sun, the smart flower tracks the sun east to west and up and down all day to provide the maximum possible energy from the available sunlight [5-7].

The cost of the solar system is always a concern to the public. The best way to compare solar panel system prices is to determine the cost per watt of electricity generation. The installed cost depends on distance of the installed smart flower from the home, whether a concrete slab foundation needs to be poured, and whether the installation requires additional electrical work. By comparison, the median price for a standard ground-mounted solar energy system without tracking capabilities on the Energy Sage Solar Marketplace was just $3.43/Watt, or $13,720 for a 4 kW system [8, 9].

In the literature of [10-12], the review report provided in this paper provides the best choice for a variety of technologies and agricultural pumps that can be used in pump systems. In other papers, it explains the applicability of motors to pump systems.

3. Proposed System

The design of the solar tracker system can be classified into three sections (Figure 1). There is the input stage that is composed of sensors and potentiometers, a program in embedded software in the microcontroller and lastly the driving circuit that has the servo motor. The input stage considers with two light dependent resistors (LDR) and that are assembled to form a voltage divider circuit. A ‘C’ program loaded into the Atmega328P microcontroller forms the embedded software. The all components are mounted in the metallic frame. The three stages are designed independently before being joined into one system. This approach similar to stepwise refinement in modular programming has been employed as it ensures an accurate and logical approach which is straight forward and easy to understand. This also ensures that if there are any errors, they are independently considered and corrected.

The main purpose to write the paper is to satisfy two main objectives:

• Design a solar system which can track the solar UV light for solar panels through the day.

• Design a tracking system for the solar panel to increase the efficiency of the system than the ordinary solar system.

The system is designed so that the sun's rays fall vertically on the solar panels to get the most solar energy. This is harnessed into the electrical power. Maximum energy is obtained between 1200 h and 1400 h, with the peak being around midday. At this time, the sun is directly overhead. At the same time, the least energy will be required to move the panel, which will further increase the system efficiency. The system is designed to address the challenge of low power, accurate and economical microcontroller-based tracking system which is implemented within the allocated time and with the available resources. It is supposed to track the sun’s movement in the sky. In order to save power, it is supposed to sleep during the night by getting back into a horizontal position. There is implementation of an algorithm that solves the motor control that is then written into C-program.

The main supply is fed to the load under normal conditions. When the main supply gets shut down, the supply from the battery connected to the system will be fed to

the load to fulfill the desired output. The battery is switched to the circuit by switching the relay. The main part of the system is that we are using two sources for charging the battery.

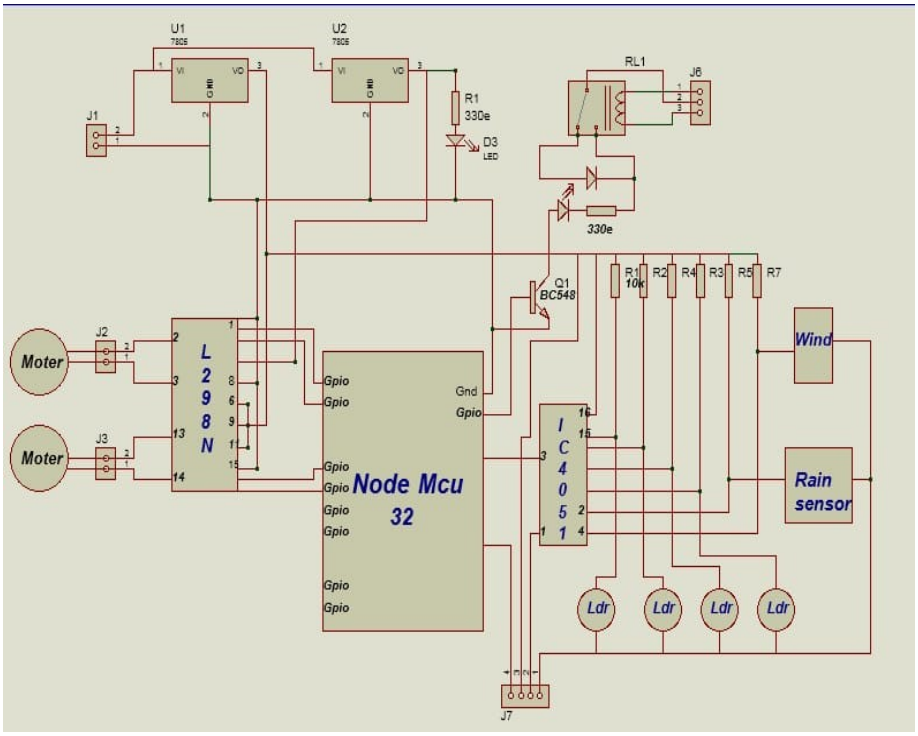

Figure 1. Designed circuit

The main supply is coming from the distribution board and the other is a power generated from the solar panel of the smart solar flower. Priority of a charging is given to the solar panel, *i.e.,* when the solar power generated exceeds the desired limit, it comes into the supply to get battery charged. The output voltage of the solar panel is kept at 12 V and is compared with the main voltage supply. When the solar panel voltage goes beyond 12 V, the battery starts charging on a solar energy. Transformer is used to step down the AC voltage 230V/12-0-12V. It is fed to the rectifier circuit which converts AC to pulsating DC. Further pulsating DC is made pure by connecting the filter in the circuit. Five V DC is fed to the Node MCU 32S and relay driving circuit. Relay switches the operations as per the instructions are given in the microcontroller ATmega328p programming. According to the relay, the motor will operate (Figure 2).

Here, we used a rain water sensor, which is connected in the circuit via two wires. One is from ground and the other is from the microcontroller's logic pin. Initially, logic is 1. But when water falls on chip, the logic will be zero and hence the flower will close. We also used a soil moisture sensor, in which initially there is logic 1 and when the logic became 0, the pump will operate. The relay used for switching purpose is electromagnetic in nature and the switching operation of the relay is performed by the controller.

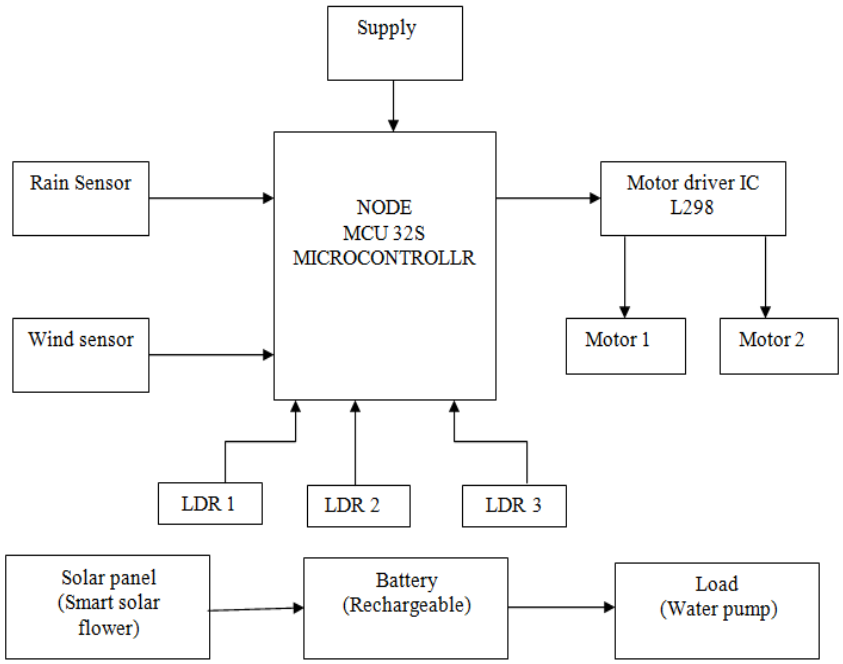

Figure 2. Block diagram of actual work

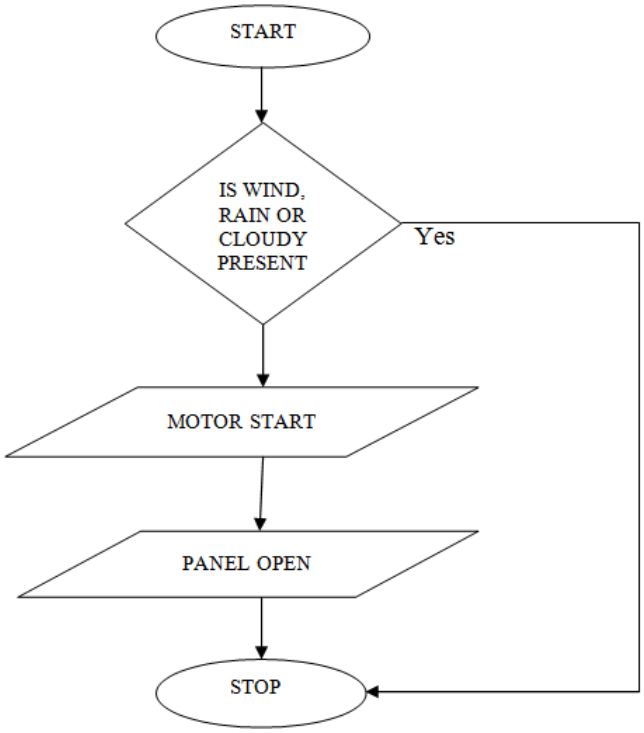

Figure 3. Working flowchart

The solar panel voltage is monitored by the microcontroller through an analog-to-digital (A/D) converter. The microcontroller is the main control core and adjusts the stepper motor so that the platform is optimally located for efficient electricity generation.

The system receives the sunlight onto the Light Dependent Resistor (LDR), where the LDR acts as the solar direction tracking sensor. The position of the LDR is obtained

when the two LDRs having the same light intensity. In the morning time, the right side LDR is turned on (as the small resistance is nearly shorted), which causes a signal to turn the motor to continuously move in clockwise until the two LDRs getting the same light intensity again. As the day slowly progresses, the left LDR is turned on and the motor turns counter clockwise. The cycle continues until the end of the day, or until the minimum detectable light level is reached. Figure 3 shows that when the sun is at the right to the solar panel, the right LDR has small value resistance, the left LDR has no light (large resistance), and the software in the micro-controller translates this to signals to control the stepper motor to rotate the panel to the right. There is a reset button for positioning the panel to an initial position which is at an inclination of 40 degrees. This is done preferably in the evening after the sun has set. It makes the LDR go back to an initial position, ready for tracking the sunlight on the next day. There is also a push button for initializing the servo motor. It switches it on, leaving it on standby mode. Pins number 7, 20 and 21 are used for powering the microcontroller. It requires 5 V. The inputs to the LDR are simulated.

The proposed model of the solar flower system is shown in Figure 4.

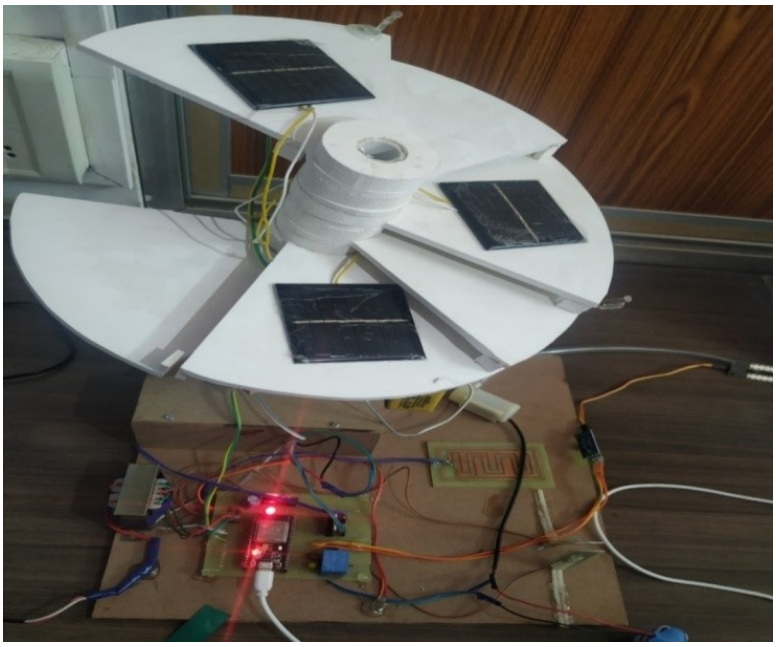

Figure 4. Proposed model

4. Results

We have gained the result that the system is more efficient as it includes the dual-axis solar tracking principle in it. Also, the system is smarter and safer as it contains the sensors such as wind sensor, soil moisture sensor, rainwater sensor and LDRs. Therefore, whenever there is a high wind or high raining, the solar flower unfolds its petals and hence protects the system from sudden damage. Since the IoT is used in this project, the project is usable in the remote areas. Due to the use of the soil moisture sensor, we could turn on or off the water pump. Here, it is a smarter energy management system with

strategy and planning based on real-time data collection and processing. This technology gave a high-tech makeover to the agriculture industry.

Advantages and disadvantages of this system include:

Advantages:

• Size of the system is small.

• System has a dual-axis tracking technology which helps in maximizing the solar energy absorption by continuously tracking the sun.

• No fuel burning in this system and therefore any pollution.

• The maintenance cost is very low.

• Because the use of solar energy is not limited, it can be used for longer period of time.

Disadvantage

• Cost of system is very high.

• The system is complex due to the batteries and motors. They are heavy and occupy more space and require time to time maintenance.

5. CONCLUSIONS

The system was designed for the benefits of various users and farmers. By using the IoT based irrigation system, it optimizes the usage of water by reducing wastage and human efforts. Proposed system is easy to implement and environment friendly solution for irrigating fields. The system was found to be successful when implemented for bore holes as they pump over the whole day. Solar pumps offer clean solutions with no danger of borehole contamination. The system has no maintenance and it also self-starting. The system can be used with application to provide energy for the pumping requirements for sprinkler irrigation. Even though there is a high capital investment required for this system to be implemented, the overall benefits are high and in long run this system is economical.

CONFLICTS OF INTEREST

The authors declare that there is no conflict of interests regarding the publication of this paper.

REFERENCES

[1] Kabalci, E., Gorgun, A., and Kabalci, Y. Design and implementation of a renewable energy monitoring system. In: *Proc., 4th International Conference on Power Engineering, Energy and Electrical Drives*, pp: 1071-1075. DOI: 10.1109/PowerEng.2013.6635759

[2] Jiju, K., Ramesh, P., Brijesh, P., Sreekumari, B. Development of Android based on-line monitoring and control system for Renewable Energy Sources. In: *Proc., 2014 International Conference on Computer, Communications, and Control Technology (I4CT)*, pp: 372-375. DOI: 10.1109/i4ct.2014.6914208

[3] Souza, A. M. C., and Amazonas, J. R. A. A Novel Smart Home Application Using an Internet of Things Middleware. In: *Proc., Smart SysTech 2013; European Conference on Smart Objects, Systems and Technologies*, pp: 1-7.
[4] Kelly, S. D. T., Suryadevara, N. K., and Mukhopadhyay, S. C. (2013). Towards the Implementation of IoT for Environmental Condition Monitoring in Homes. *IEEE Sensors Journal*, 13(10), 3846-3853. DOI: 10.1109/jsen.2013.2263379
[5] Iera, A., Floerkemeier, C., Mitsugi, J., and Morabito, G. (2010). The Internet of things [Guest Editorial]. *IEEE Wireless Communications*, 17(6), 8-9. DOI: 10.1109/mwc.2010.5675772
[6] Bikash, D. Solar powered lighting and ventilation of poultry house. *MS thesis,* Mymensingh: Bangladesh Agricultural University, Department of Farm Power and Machinery, Vol.19, March 2014.
[7] Roblin, S. (2016). Solar-powered irrigation: A solution to water management in agriculture? *Renewable Energy Focus*, 17(5), 205-206. DOI: 10.1016/j.ref.2016.08.013
[8] Hussain, M. I., and Lee, G. H. (2015). Utilization of solar energy in agricultural machinery engineering: A review. *Journal of Biosystems Engineering*, 40(3), 186-192.
[9] Jie, Y., Pei, J. Y., Jun, L., Yun, G., and Wei, X. Smart Home System Based on IOT Technologies. In: *Proc., 2013 International Conference on Computational and Information Sciences*, pp: 1789-1791. DOI: 10.1109/iccis.2013.468
[10] Band, B.H., Ingole, A.D. IOT and GSM based solar operated water pump system: a technical review. *INTERNATIONAL JOURNAL OF CURRENT ENGINEERING AND SCIENTIFIC RESEARCH (IJCESR)*, Volume 6, issue 3, 2019, pp: 170-172.
[11] Band, B.H., Ingole, A.D. Mathematical and Simulation Approach for Synchronization of Two Asynchronous Grids. *INTERNATIONAL JOURNAL OF ENGINEERING RESEARCH & TECHNOLOGY (IJERT),* Volume 7, issue 9, Sept-18, pp: 24-27
[12] Band, B.H., Ingole, A.D. Transfer of Power by using two Induction Machines. *INTERNATIONAL JOURNAL OF CURRENT ENGINEERING AND SCIENTIFIC RESEARCH (IJCESR)*, Volume 4, issue 8, 2017, pp: 36-40

Trends in Renewable Energy
OPEN ACCESS ISSN: 2376-2144
Peer-Reviewed Article futureenergysp.com/index.php/tre

Virtual Indicative Broadband over Power Lines Topologies for Respective Subclasses by Adjusting Channel Attenuation Statistical Distribution Parameters of Statistical Hybrid Models (Class Maps) – Part 1: Theory

Athanasios G. Lazaropoulos*

School of Electrical and Computer Engineering / National Technical University of Athens / 9 Iroon Polytechniou Street / Zografou, GR 15780

Received June 21, 2019; Accepted August 12, 2019; Published August 15, 2019

Based on a set of indicative overhead and underground medium voltage broadband over power lines (OV and UN MV BPL) topologies, initial statistical hybrid model (iSHM) and modified statistical hybrid model (mSHM) are statistical channel models suitable for the distribution BPL networks. Both iSHM and mSHM statistically process channel attenuation and capacity values of assumed indicative OV and UN MV BPL topologies by exploiting channel attenuation statistical distributions (CASDs). iSHM exploits a set of well-known CASDs (*i.e.*, Gaussian, Lognormal, Wald, Weibull and Gumbel CASDs) while mSHM exploits the Empirical CASD. Each indicative OV and UN MV BPL topology acts as the representative one of a respective OV and UN MV BPL topology class (*i.e.,* rural, suburban, urban and aggravated urban class) that consists of a number of respective statistically equivalent OV and UN MV BPL topologies. The contribution of this paper is the theoretical framework presentation of the creation of new virtual indicative OV and UN MV BPL topologies by appropriately adjusting the parameters of iSHM and mSHM CASDs. These new virtual indicative OV and UN MV BPL topologies will enrich the respective today's OV and UN MV BPL topology classes with respective OV and UN MV BPL topology subclasses while each subclass will be enriched by a number of respective statistically equivalent OV and UN MV BPL topologies. The procedure of defining new virtual distribution BPL topologies by applying iSHM and mSHM will allow a better capacity study of OV and UN MV BPL topology classes. Apart from the definition procedure of the virtual indicative OV MV and UN MV BPL topologies and their respective virtual subclasses by adjusting CASD parameters of iSHM and mSHM, the contribution of this paper is the class map that analytically describes the taxonomy of distribution BPL topology classes and subclasses.

Keywords: Smart Grid; Broadband over Power Lines (BPL) networks; Power Line Communications (PLC); Distribution Power Grids; Capacity; Statistics; Modeling

1. Introduction

**Corresponding author:* AGLazaropoulos@gmail.com

Tr Ren Energy, 2019, Vol.5, No.3, 237-257. doi: 10.17737/tre.2019.5.3.0099

The today's traditional power grid is evolving to an intelligent IP-based communications network enhanced with a plethora of broadband applications, widely referred to as smart grid [1]-[13]. Actually, smart grid can support two types of flows; say, a two-way power and a two-way information flow [14]-[16]. As the two-way power flow is concerned, apart from the traditional power flow from power generators to the customers, there is the power that is generated by the customers and be injected back into the power grid. As the two-way information flow is concerned, the proposed broadband applications can help either power utilities to monitor, meter, control and provide valuable real-time detailed information on actual operation of the power grid or customers to control dynamic power flows and meet more profitably their power demands. Among the available communications solutions that can support this two-way information flow of smart grid is the Broadband over Power Lines (BPL) technology that can play important role since it may support an electronic communications channel (*i.e.*, BPL channel) upon the already installed wired power grid infrastructure and, at the same time, interconnect with other already installed communications solutions of the smart grid through its wireline/wireless interfaces [3], [17]-[28].

Dealing with the BPL statistical channel modeling, the initial statistical hybrid model (iSHM) has been proposed in [17, 18], while the modified statistical hybrid model (mSHM) has been proposed in [29]. Both models consist of six phases (*i.e.*, Phase A-F) while their core is the deterministic hybrid model of Phase B that has extensively been validated in transmission and distribution BPL networks and comprises two interconnected submodules, namely: (i) the bottom-up approach module; and (ii) the top-down approach module [4], [23]-[27], [30]-[34]. The common input data basis is the consideration of a set of indicative distribution BPL topologies that acts as the representative topologies of a set of respective distribution BPL topology classes –*i.e.*, rural, suburban, urban and aggravated urban classes– where each distribution BPL topology class is filled with statistically equivalent BPL topologies [17], [18], [29]. The result of iSHM and mSHM is the capacity range of each distribution BPL topology class for given operation frequency range, power grid type, injected power spectral density (IPSD) limits, noise level, coupling scheme and channel attenuation statistical distribution (CASD). As the CASDs are concerned, iSHM applies five well-known CASDs of the communications literature, say, Gaussian, Lognormal, Wald, Weibull and Gumbel ones [17, 18], while mSHM applies the Empirical CASD [29]. The selection of a CASD plays a critical role during the capacity range computation of each distribution BPL topology class since it mainly affects the results of the random number generator module (Phase D of iSHM and mSHM) through the maximum likelihood estimators (MLE) computation module (Phase C of iSHM) or Empirical CASD module (Phase C of mSHM). As the Phase C of iSHM is concerned, MLE computation method helps towards the MLE estimation of the applied CASDs given the coupling scheme channel attenuation differences of the Phase B [17], while the Phase C of mSHM computes the cumulative density function (CDF) given the coupling scheme channel attenuation differences of the Phase B [29].

The issue that this paper is dealing with is the underrepresentation of the aforementioned distribution BPL topology classes, as defined in this paper, through the insertion of virtual indicative OV and UN MV BPL topologies and their respective subclasses. In fact, the indicative distribution BPL topologies, which have been presented

in [17], [18], [29], also stand in this paper and define the respective main indicative distribution BPL topology subclasses as well as the titles of the respective distribution topology classes. As the operation of iSHM and mSHM is concerned, each indicative distribution BPL topology is characterized by a set of parameters regarding either iSHM (*i.e.,* MLEs) or mSHM (*i.e.,* Empirical CDF). Based on the set of parameters of an indicative distribution BPL topology, the respective main indicative distribution BPL topology subclass is filled with statistically equivalent BPL topologies, which are generated by a random number generator and are characterized by the same parameters with the representative topology of the examined main subclass for given power grid type, coupling scheme and CASD. In fact, by appropriately adjusting the parameters of iSHM and mSHM, new virtual indicative distribution BPL topologies can be proposed that further define their respective distribution BPL topology subclasses, which will further be enriched with statistically equivalent BPL topologies. In this paper, distribution BPL topology classes are defined as capacity areas (*i.e.,* capacity ranges) that comprise distribution BPL topology subclasses, whose average capacities lie in the middle of the distribution BPL topology class capacity ranges. Hence, distribution BPL topology classes will be filled with respective subclasses while the capacity ranges of distribution BPL topology classes are going to define valid combinations of parameters of iSHM and mSHM (CASD parameter mapping). On the basis of the CASD parameter mapping, virtual distribution BPL topology subclasses are identified while these subclasses are categorized into appropriate distribution BPL topology classes in terms of their average capacities (Subclass and Class Mapping). The numerical results of the full deployment of class mapping are presented: (i) for OV MV and UN MV BPL networks in [35]; and (ii) for OV high-voltage (HV) BPL networks in [36].

The rest of this paper is organized as follows: In Section II, the usual OV MV and UN MV MTL configurations with a set of indicative BPL topologies are presented. Section III summarizes the basics of the iSHM and mSHM. In Section IV, the definition procedure of the virtual indicative OV MV and UN MV BPL topologies and their respective virtual subclasses, briefly denoted as definition procedure, by adjusting CASD parameters of iSHM and mSHM is detailed. Section V concludes this paper.

2. OV MV and UN MV MTL Configurations and BPL Topologies

In this section, a small briefing regarding the applied OV MV and UN MV MTL configurations is given while the topological characteristics of the indicative OV MV and UN MV BPL topologies are reported. Note that these indicative distribution BPL topologies will act either as the reference topologies so that the capacity ranges of the distribution BPL topology classes are defined or representative topologies of the first respective distribution BPL topology subclasses of the corresponding BPL topology classes (main subclasses). Also, various distribution BPL topologies are presented that are going to be classified in the proposed distribution BPL topology classes and will further help the analysis.

2.1 OV MV and UN MV MTL Configurations

The OV MV and UN MV distribution lines that are used in the first two papers

are depicted in Figs. 1(a) and 1(b) of [17], respectively. As the OV MV distribution lines are concerned, these lines consists of three parallel non-insulated phase conductors ($n^{\mathrm{OVMV}} = 3$) spaced by Δ^{OVMV} and hang at typical heights h^{OVMV} above lossy ground. As the UN MV distribution lines are concerned, these lines are the three-phase sector-type PILC distribution-class cable (8/10kV, 3×95mm^2 Cu, PILC) surrounded by the shield and the armor conductor ($n^{\mathrm{UNMV}} = 3$). The exact dimensions of the OV MV and UN MV MTL configurations are given in [30] as well as the ground properties, the applied grounding practices and the BPL signal propagation / transmission when a lossy ground is considered.

2.2 OV MV and UN MV BPL Topologies and Respective Topology Subclasses and Classes

With reference to Fig. 1, BPL networks are divided into cascaded BPL topologies. Each BPL topology is bounded by its transmitting and receiving end where BPL devices (*i.e.*, either injector or repeater or extractor) are installed. Depending on the power grid type environment of the BPL topology (*i.e.*, rural, suburban, urban or aggravated urban), different number of branches $k,\ k = 1, \cdots, N$, distribution cable lengths $L_k,\ k = 1, \cdots, N+1$ and branch lengths $L_{\mathrm{b}k},\ k = 1, \cdots, N$ are encountered across the BPL signal transmission path. To study distribution BPL topologies, hybrid model further divides the BPL topology into concatenated network modules [4], [23]-[27], [30].

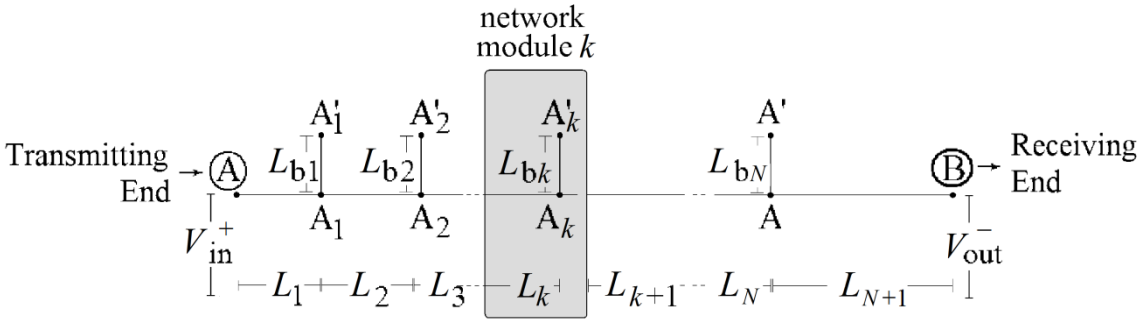

Fig. 1. Typical distribution BPL topology with *N* branches [17].

In accordance with [5], [17], [23]-[26], [30], five distribution BPL topology classes –*i.e.,* "Line-of-Sight" ("LOS"), rural, suburban, urban and aggravated urban– are required, so that a thorough analysis regarding the distribution BPL network performance is accomplished. Until now, an indicative distribution BPL topology has been adopted as the representative one for each distribution BPL topology class (say, urban case A, urban case B, suburban case, rural case and "LOS" case for distribution BPL typical urban, aggravated urban, suburban, rural and "LOS" topology class, respectively). In these papers, each indicative distribution BPL topology will act as the representative one for the main subclass of the respective distribution BPL topology class. In Tables 1 and 2, the indicative OV MV and UN MV BPL topologies of the main subclasses per each class, which are characterized by their unique topology number, are reported, respectively, as well as their corresponding topological characteristics. Also,

apart from the indicative OV MV and UN MV BPL topologies of the main subclasses per each class, two indicative OV MV and UN MV BPL topologies, which are also characterized by a unique topology number, are added per each OV MV and UN MV BPL topology class, respectively. Note that distribution "LOS" cases describe the Line-of-Sight BPL signal transmission path and for that reason, distribution "LOS" topology classes consist of only one topology; say, distribution "LOS" cases. In accordance with [5], [17], [23]-[26], [30], note that average long end-to-end connections of 1000 m and 200 m are assumed for the indicative OV MV and UN MV BPL topologies, respectively, as the typical case holds.

Table 1
Indicative OV MV BPL Topologies and Respective BPL Topology Classes [17], [5]

OV MV BPL Topology Class	**BPL Topology Number (and BPL Topology Subclass Number) (*l*)**	**BPL Topology Name (and BPL Topology Subclass Name)**	**Number of Branches**	**Length of Distribution Lines**	**Length of Branching Lines**
Typical OV MV BPL urban topology class	OV MV 1	OV MV Urban case A (main subclass)	3	L_1=500m, L_2=200m, L_3=100m, L_4=200m	L_{b1}=8m, L_{b2}=13m, L_{b3}=10m
Aggravated OV MV BPL urban topology class	OV MV 2	OV MV Urban case B (main subclass)	5	L_1=200m, L_2=50m, L_3=100m, L_4=200m, L_5=300m, L_6=150m	L_{b1}=12m, L_{b2}=5m, L_{b3}=28m, L_{b4}=41m, L_{b5}=17m
OV MV BPL suburban topology class	OV MV 3	OV MV Suburban case (main subclass)	2	L_1=500m, L_2=400m, L_3=100m	L_{b1}=50m, L_{b2}=10m
OV MV BPL rural topology class	OV MV 4	OV MV Rural case (main subclass)	1	L_1=600m, L_2=400m	L_{b1}=300m
OV MV BPL "LOS" topology class	OV MV 5	OV MV "LOS" case (main subclass)	0	L_1=1000m	-

Table 2
Indicative UN MV BPL Topologies and Respective BPL Topology Classes [17], [5]

UN MV BPL Topology Class	BPL Topology Number (and BPL Topology Subclass Number) (l)	BPL Topology Name (and BPL Topology Subclass Name)	Number of Branches	Length of Distribution Lines	Length of Branching Lines
Typical UN MV BPL urban topology class	UN MV 1	UN MV Urban case A (main subclass)	3	L_1=70m, L_2=55m, L_3=45m, L_4=30m	L_{b1}=12m, L_{b2}=7m, L_{b3}=21m
Aggravated UN MV BPL urban topology class	UN MV 2	OV MV Urban case B (main subclass)	5	L_1=40m, L_2=10m, L_3=20m, L_4=40m, L_5=60m, L_6=30m	L_{b1}=22m, L_{b2}=12m, L_{b3}=8m, L_{b4}=2m, L_{b5}=17m
UN MV BPL suburban topology class	UN MV 3	UN MV Suburban case (main subclass)	2	L_1=50m, L_2=100m, L_3=50m	L_{b1}=60m, L_{b2}=30m
UN MV BPL rural topology class	UN MV 4	UN MV Rural case (main subclass)	1	L_1=50m, L_2=150m	L_{b1}=100m
UN MV BPL "LOS" topology class	UN MV 5	UN MV "LOS" case (main subclass)	0	L_1=200m	-

3. The Basics of iSHM and mSHM

In this Section, the flowcharts of iSHM and mSHM, which are given in terms of business process modeling notation (BPMN) diagrams, are demonstrated. On the basis of these BPMN diagrams, the Phases of iSHM and mSHM are presented while the required modifications for creating virtual distribution BPL topologies (*i.e.,* definition procedure of virtual distribution BPL topologies) are also given.

3.1 iSHM

The BPMN diagram of iSHM flowchart is presented in Fig. 2(a). In accordance with [17] and with respect to Fig. 1(a), iSHM consists of six phases; say, Phase A-F. Each phase is depicted as a grey container while their corresponding modules and produced files are shown in light blue color. iSHM receives as inputs the distribution power grid type, the indicative distribution BPL topology, the respective distribution MTL configuration, the applied coupling scheme and the capacity related parameters while it gives as output the capacity range of each distribution BPL topology subclass $\mathbf{CR}_l^{\mathrm{G,C,D}} = [min\{\mathbf{C}_l^{\mathrm{G,C,D}}\} \;\; average\{\mathbf{C}_l^{\mathrm{G,C,D}}\} \;\; max\{\mathbf{C}_l^{\mathrm{G,C,D}}\}]$ where $[\cdot]^{\mathrm{G}}$ denotes the examined distribution power grid type (*i.e.,* OV MV or UN MV), $[\cdot]^{\mathrm{C}}$ denotes the applied coupling scheme (see Sec.3.2 of [17]), $[\cdot]^{\mathrm{D}}$ denotes the applied CASD (*i.e.,* Gaussian or Lognormal or Wald or Weibull or Gumbel distribution), $[\cdot]_l$ denotes the examined distribution BPL topology subclass number (see Tables 1 and 2) and $min\{\cdot\}$, $average\{\cdot\}$

and $max\{\cdot\}$ computes the minimum, the average and the maximum value of distribution BPL topology class capacity $\mathbf{C}_l^{G,C,D}$ that consists of all the capacities of its P+1 members of the examined distribution BPL topology subclass.

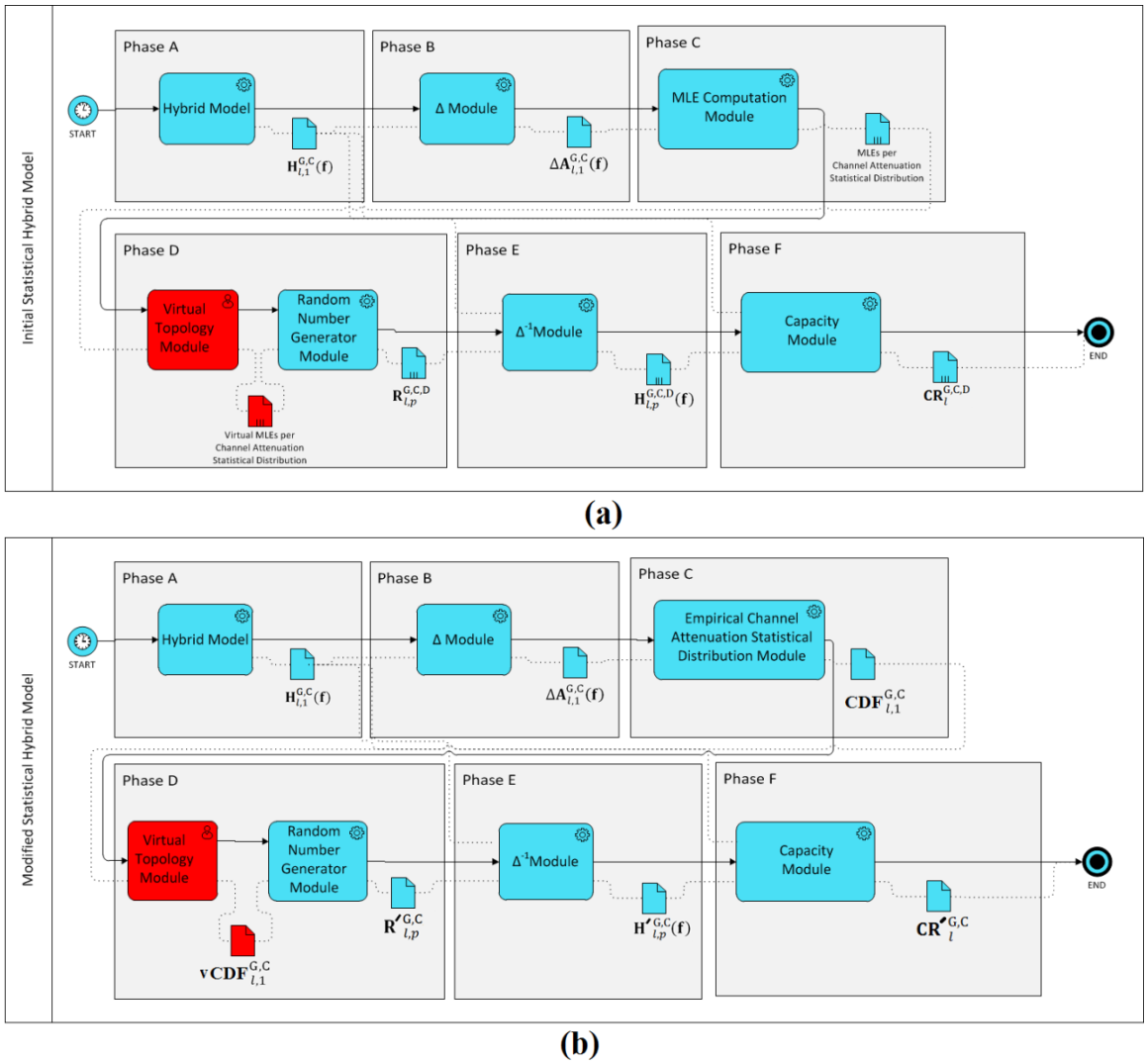

Fig. 2. Business Process Reengineering of the Statistical Hybrid Model. (a) BPMN diagram of the iSHM [17]. (b) BPMN diagram of the mSHM [29].

Although the Phases of iSHM and the input/output of iSHM are detailed in [17], the Phases that deserve further attention in this paper are Phases C and D since they are mainly affected by the definition procedure of virtual indicative OV MV and UN MV BPL topologies and their respective virtual subclasses. In fact, Phase C consists of the MLE computation module that receives as input the coupling scheme channel attenuation difference and gives as output the MLEs for each of the five CASDs for given indicative distribution BPL topology and coupling scheme where the coupling scheme channel attenuation difference of an indicative distribution BPL topology expresses the channel attenuation difference between the examined BPL topology and its respective "LOS"

case for given power grid type and coupling scheme. Then, the random number generator of Phase D receives as input the MLEs of each CASD and gives as output the random number $1\times Q$ line vector $\mathbf{R}_{l,p}^{\mathrm{G,C,D}}$ for given power grid type, coupling scheme and indicative distribution BPL topology where Q is the number of flat-fading subchannels in the examined 3-30MHz frequency range, p, p=1,…,P+1 is the member number in the BPL topology subclass and P is the member number of each subclass.

In Fig. 2(a), the additional BPMN elements, which will allow the application of the definition procedure of virtual indicative OV MV and UN MV BPL topologies and their respective virtual subclasses in iSHM, are shown in red color. More specifically, the required modifications of iSHM are gathered into the virtual topology module of Phase D. Then, the output of the virtual topology module (*i.e.*, virtual MLEs per channel attenuation statistical distribution) is delivered as the new input of the random number generator module. In fact, virtual topology module can operate by ignoring the MLEs per CASD so far defined by Phase A-C and introduce new pairs of MLEs (virtual MLEs) per CASD without the need for the applied indicative distribution BPL topology. Thus, the random number generator module is fed by virtual MLEs per CASD while it defines the corresponding P random number $1\times Q$ line vectors $\mathbf{R}_{l,p}^{\mathrm{G,C,D}}$ per virtual MLE pair set. In total, after the processing of the P+1 random number line vectors by the Phase E and F of the iSHM, a new virtual distribution BPL topology subclass rises with P+1 virtual topology members where the virtual indicative distribution BPL topology of the topology subclass is only characterized by its virtual MLEs proposed by the virtual topology module without any information concerning its topological characteristics.

In Sec.4.1, details concerning the operation of the virtual topology module of iSHM are given. More specifically, the definition procedure of virtual MLEs per CASD is presented as well as the restrictions that should be imposed so that valid virtual distribution BPL topologies can be defined in iSHM.

3.2 mSHM

The introduction of mSHM focuses on the application of only one CASD, say, the Empirical CASD, thus bypassing the time-consuming identification of the best CASD among the five CASDs of iSHM that anyway takes into consideration each time the current operation settings. Here it should be noted that the Empirical CASD is the distribution function associated with the Empirical measure of coupling scheme channel attenuation differences.

The BPMN diagram of mSHM flowchart is presented in Fig. 2(b). In accordance with [29] and with respect to Figs. 2(a) and 2(b), mSHM consists of six phases; say, Phase A-F, similarly to iSHM. Each phase is depicted as a grey container while their corresponding modules and produced files are shown in light blue color. Actually, Phases A, B, E and F remain identical between the iSHM and mSHM. Conversely, the cause of differences in the Phases C and D between iSHM and mSHM is the adoption of the Empirical CASD by mSHM. In fact, the adoption of Empirical CASD, which is only used by mSHM, has as a result the substitution of all the five applied CASDs of iSHM (*i.e.*, Gaussian or Lognormal or Wald or Weibull or Gumbel distribution). In accordance with [29], the adoption of Empirical CASD achieves comparable performances to the ones of the five applied CASDs of iSHM and, at the same time, this adoption bypasses the time loss required to identify the best CASD of iSHM by taking into consideration

each time the current operation settings. As the Phase differences between iSHM and mSHM are concerned, instead of the MLE computation module of iSHM in Phase C, the Empirical channel attenuation statistical distribution module is here added for mSHM that receives as input the coupling scheme channel attenuation difference while it gives as output the empirical CDF of the coupling scheme channel attenuation difference $\mathbf{CDF}_{l,1}^{G,C}$ for given distribution BPL topology and coupling scheme. In Phase D of mSHM, the random number generator receives as input the Empirical CDF of the examined coupling scheme channel attenuation difference instead of MLEs in iSHM. With reference to [37], [38], random number generator module performs an inverse interpolation to achieve CDF projection of the random values thus giving as output the random number $1\times Q$ line vector $\mathbf{R}'^{G,C}_{l,p}$ for given coupling scheme and indicative distribution BPL topology.

Similarly to iSHM, the additional BPMN elements, which will allow the application of the definition procedure of virtual indicative OV MV and UN MV BPL topologies and their respective virtual subclasses in mSHM, are shown in red color in Fig. 2(b). Again, the required modifications of mSHM are gathered into the virtual topology module of Phase D. In contrast with iSHM, the output of the virtual topology module that is a virtual CDF is delivered as the new input of the random number generator module. To operate, virtual topology module needs CDF so far defined by Phase A-C and can introduce new CDFs (virtual CDFs) by vertically and horizontally shifting CDF of the applied indicative distribution BPL topology. Thus, the random number generator module is fed by virtual CDFs while it defines the corresponding P random number $1\times Q$ line vectors $\mathbf{R}'^{G,C}_{l,p}$. In total, the new virtual distribution BPL topology subclass of mSHM with P+1 virtual topology members is defined where the virtual indicative distribution BPL topology of the topology subclass is only characterized by its virtual Empirical CDF proposed by the virtual topology module without any information concerning its topological characteristics.

In Sec.4.2, details concerning the operation of the virtual topology module of mSHM are given. More specifically, the definition procedure of a virtual CDF per indicative distribution BPL topology is presented in mathematical terms as well as the restrictions that should be imposed to the horizontal and vertical shifts of the virtual CDF so that valid virtual distribution BPL topologies can be defined in mSHM.

4. CASD Parameters Adjustment for Defining Virtual Distribution BPL Topologies and Respective Subclasses

In this Section, the definition procedure of the virtual indicative OV MV and UN MV BPL topologies and their respective virtual subclasses by adjusting CASD parameters of iSHM and mSHM is detailed while the required restrictions concerning the proper definition are presented.

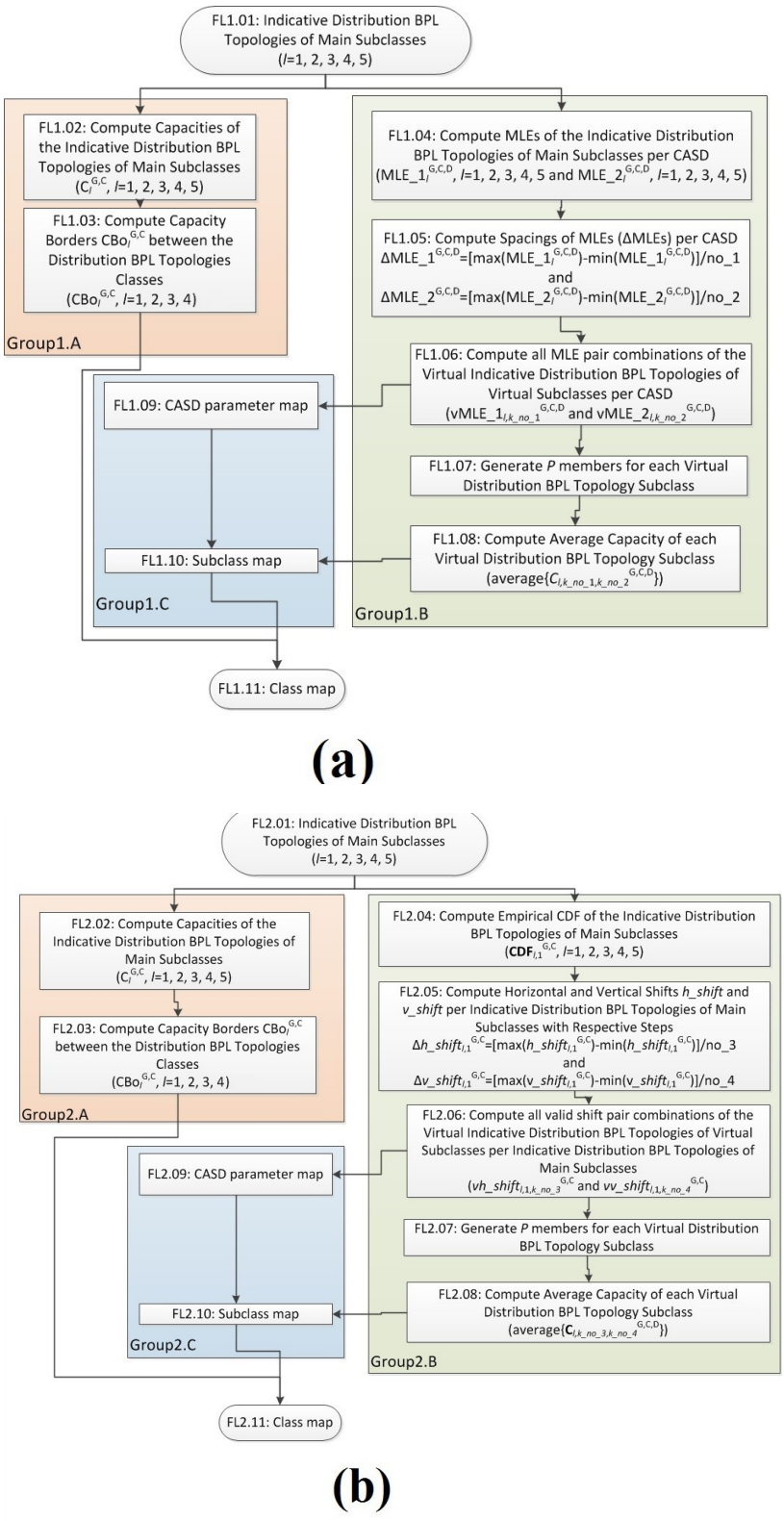

Fig. 3. Flowcharts of the CASD parameter adjustment for defining virtual distribution BPL topologies and subclasses of the Statistical Hybrid Model.
(a) Definition procedure flowchart for the iSHM. (b) Definition procedure flowchart for the mSHM.

4.1 Definition Procedure of iSHM

Actually, in this subsection, the operation of the virtual topology module of Phase D of Fig. 2(a) is studied as well as its output, say virtual MLEs per CASD. In fact, the internal operation of the virtual topology module cannot be seen without the flow of its output until the end and for that reason all this procedure is demonstrated through the flowchart of Fig. 3(a).

In accordance with Fig. 3(a), there are eleven steps so that the class map, which is the result of the definition procedure, can be plotted where class map is a two-dimensional contour plot that depicts the average capacity of each possible virtual distribution BPL topology subclass classified in specific classes. Note that indicative distribution BPL topologies of main subclasses of Tables 1 and 2 are explicitly demonstrated in the class map while these BPL topologies become crucial for defining the borders between the adjacent distribution BPL topology classes as presented in the following analysis. With reference to Fig. 3(a), after the definition of the indicative distribution BPL topologies of main subclasses of Tables 1 and 2 (step FL1.01), the result of class mapping is accomplished through three groups of steps, namely:

1. *Group1.A*: This group consists of two steps (FL1.02 and FL1.03). First, the capacities of the indicative distribution BPL topologies of main subclasses $C_l^{G,C}, l = 1,2,3,4,5$ are computed in the step FL1.02. Second, given the capacities of the indicative distribution BPL topologies of main subclasses from FL1.02, which anyway act as the representative BPL topologies of the respective distribution BPL topology classes, the capacity borders between the adjacent distribution BPL topology classes $CBo_l^{G,C}, l = 1,2,3,4$ are determined by

$$\mathbf{CBo}^{G,C} = \left[CBo_l^{G,C}\right], l = 1,2,3,4 = \left[\frac{C_{1,1}^{G,C}+C_{2,1}^{G,C}}{2} \quad \frac{C_{2,1}^{G,C}+C_{3,1}^{G,C}}{2} \quad \frac{C_{3,1}^{G,C}+C_{4,1}^{G,C}}{2} \quad C_5^{G,C}\right] \quad (1)$$

From eq. (1), it is evident that $CBo_4^{G,C}$, which is equal to the capacity of the distribution BPL "LOS" topology case $C_5^{G,C}$, describes the capacity upper limit that can be achieved for given power grid type and coupling scheme. As the other distribution BPL topology class capacity borders are considered, these are treated as the mean capacity value of the neighboring indicative distribution BPL topologies of the main subclasses of Tables 1 and 2. Note that $CBo_l^{G,C}, l = 1,2,3,4$ describe the borders: (i) between the aggravated distribution BPL urban topology class and typical distribution BPL urban topology class; (ii) between the typical distribution BPL urban topology class and the distribution BPL suburban topology class; (iii) between the typical distribution BPL suburban topology class and the distribution BPL rural topology class; (iv) between the typical distribution BPL rural topology class and the distribution BPL "LOS" topology class; and (v) the upper capacity bound that is equal to the capacity of the distribution BPL "LOS" case, respectively. In total, the capacities of the indicative distribution BPL topologies of main subclasses and the capacity borders between the adjacent distribution BPL topology classes remain crucial elements during the class mapping since they define the placement of the capacities of the virtual distribution BPL topology subclasses.
2. *Group1.B*: This group consists of five steps (FL1.04-FL1.08). At step FL1.04, the MLE estimation of the applied CASD given the coupling scheme channel

attenuation differences of the examined distribution BPL topology is accomplished at Phase B of iSHM, as described in Fig. 2(a). Actually, according to the step FL1.04, the MLE computation module provides a MLE pair given the indicative distribution BPL topologies of main subclasses of Tables 1 and 2 per CASD. Literally, each MLE pair of the indicative distribution BPL topologies of the main subclasses per CASD consists of $MLE\_1_l^{G,C,D}, l = 1,2,3,4,5$ and $MLE\_2_l^{G,C,D}, l = 1,2,3,4,5$. At step FL1.05, the accuracy of the class mapping can be adjusted by the length of horizontal and vertical spacings, say

$$\Delta MLE\_1_l^{G,C,D} = \frac{max\left\{MLE\_1_l^{G,C,D}\right\} - min\left\{MLE\_1_l^{G,C,D}\right\}}{no\ 1}, l = 1,2,3,4,5 \quad (2)$$

$$\Delta MLE\_2_l^{G,C,D} = \frac{max\left\{MLE\_2_l^{G,C,D}\right\} - min\left\{MLE\_2_l^{G,C,D}\right\}}{no\ 2}, l = 1,2,3,4,5 \quad (3)$$

, respectively, where no_1 and no_2 are the number of spacings for the horizontal and vertical axis, respectively. At step FL1.06, all $(no\_1 + 1) \times (no\_2 + 1)$ MLE pair combinations of the virtual indicative distribution BPL topologies of virtual classes per CASD $\left[vMLE\_1_{l,k\_no\_1}^{G,C,D} \quad vMLE\_2_{l,k\_no\_1}^{G,C,D}\right], k\_no\_1 = 0,1,\cdots,no\_1, k\_no\_2 = 0,1,\cdots,no\_2$

, which are anyway computed by taking into account the horizontal and vertical spacings of eqs. (2) and (3), respectively, are computed, namely:

$$vMLE\_1_{l,k\ no\ 1}^{G,C,D} = min\left\{MLE\_1_l^{G,C,D}\right\} + k\_no\_1 \cdot \Delta MLE\_1_l^{G,C,D}, l = 1,2,3,4,5, \quad k\_no\_1 = 0,1,\cdots,no\_1 \quad (4)$$

$$vMLE\_2_{l,k\ no\ 2}^{G,C,D} = min\left\{MLE\_2_l^{G,C,D}\right\} + k\_no\_2 \cdot \Delta MLE\_2_l^{G,C,D}, l = 1,2,3,4,5, \quad k\_no\_2 = 0,1,\cdots,no\_2 \quad (5)$$

Anyway, MLE pair combinations of the virtual indicative distribution BPL topologies of virtual subclasses per CASD are considered as the output of the virtual topology module of Phase D of Fig. 2(a) and as the essential modification of iSHM towards the enrichment of the distribution BPL topology subclasses. In fact, at step FL1.07, the random number generator of Phase D of Fig.2(a) exploits the MLE pair combinations of the virtual indicative distribution BPL topologies of virtual classes per CASD and it generates *P* members for each distribution BPL topology subclass. Finally, step FL1.08 synopsizes the operation of Phases E and F of iSHM as described in Fig. 2(a) while the output of step FL1.08 is the average capacity value average$\{ C_{l,k\ no\ 1,k\ no\ 2}^{G,C,D} \}$, $k\_no\_1 = 0,1,\cdots,no\_1$, $k\_no\_2 = 0,1,\cdots,no\_2$ of each distribution BPL topology subclass. The output of steps FL1.06 and FL1.08 seed the Group1.C that is responsible for the mapping of the results.

3. *Group1.C*. This group consists of two steps (FL1.09 and FL1.10) and is the responsible one for the class mapping. First, step FL1.09 receives as input the output of the step FL1.06, say, all $(no\_1 + 1) \times (no\_2 + 1)$ MLE pair combinations of the virtual indicative distribution BPL topologies of virtual classes per CASD $\left[vMLE\_1_{l,k\_no\_1}^{G,C,D} \quad vMLE\_2_{l,k\_no\_1}^{G,C,D}\right], k\_no\_1 = 0,1,\cdots,no\_1, k\_no\_2 = 0,1,\cdots,no\_2$

. Hence, the minimum and maximum values of horizontal and vertical axes of the

2D contour plot of the class map are well defined per CASD as well as all the possible combinations of the horizontal and vertical values. This procedure is denoted as CASD parameter mapping. Second, FL1.10 receives: (i) the CASD parameters from FL1.09; and (ii) the average capacity values average$\{C^{G,C,D}_{l,k\ no\ 1,k\ no\ 2}\}$, $k\_no\_1 = 0,1,\cdots,no\_1$, $k\_no\_2 = 0,1,\cdots,no\_2$ of each distribution BPL topology subclass that correspond to all possible combinations of horizontal values k_no_1 and vertical values k_no_2. Actually, the existing CASD parameter map of FL1.09 is enriched by the average capacities of all distribution BPL topology subclasses and the subclass map is treated as the output of FL1.10 and, thus, Group1.C.

The last step of the definition procedure of the virtual indicative OV MV and UN MV BPL topologies and their respective virtual subclasses is step FL1.11. By synthesizing its inputs into a 2D contour plot, step FL1.11 receives the CASD parameter map from Group1.C and the capacities of the indicative distribution BPL topologies of main subclasses accompanied with the capacity borders between the adjacent distribution BPL topology classes from Group1.A and gives as output the class map that is the result of the definition procedure of the virtual indicative OV MV and UN MV BPL topologies and their respective virtual subclasses of iSHM.

4.2 Definition Procedure of mSHM

Similarly to iSHM, in this subsection, the operation of the virtual topology module of Phase D of Fig. 2(b) is studied as well as its output. Conversely to virtual MLEs per CASD of iSHM, the output of the virtual tropology module of mSHM is the virtual Empirical CDF $\mathbf{vCDF}^{G,C}_{l,1}, l = 1,2,3,4,5$ of the examined coupling scheme channel attenuation difference. Similarly to Sec.4.1, the flow of the virtual topology module of Phase D until the end is demonstrated through the flowchart of Fig. 3(b).

In accordance with Fig. 3(b), class mapping consists of eleven steps (FL2.01-FL2.11) that are further classified into three groups (Group2.A-Group2.C). Similarly to the definition procedure of iSHM of Fig. 3(a), with reference to Fig. 3(b), after the definition of the indicative distribution BPL topologies of main subclasses of Tables 1 and 2 (step FL2.01), the result of class mapping is accomplished through three groups of steps, namely:

1. *Group2.A*: This group consists of two steps (FL2.02 and FL2.03). Both FL2.02 and FL2.03 are the same with FL1.02 and FL1.03, respectively. In general, the input of the definition procedure of mSHM, which is the output of the step FL2.01, remains the same one with the definition procedure of iSHM and the output of the definition procedure of mSHM, which is the capacity borders between the adjacent distribution BPL topology classes $CBo^{G,C}_{l}, l = 1,2,3,4,5$ as given in eq.(1), again remains the same one with the definition procedure of iSHM.
2. *Group2.B*: This group consists of five steps (FL2.04-FL2.08). At step FL2.04, the Empirical CDFs $\mathbf{CDF}^{G,C}_{l,1}, l = 1,2,3,4,5$ of the indicative distribution BPL topologies of main subclasses are delivered by the Empirical Channel Attenuation Statistical Distribution module of Phase C of mSHM. Similarly to the role of CASD selection of iSHM, the selection of the reference distribution BPL

topology among the available indicative distribution BPL topologies of the main subclasses will define either the calculations of FL2.05-FL2.08 or the final class map. At step FL2.05, the Empirical CDF of the virtual distribution BPL topologies of subclasses can be adjusted by the spacing of horizontal shift $h\_shift_{l,1}^{G,C}$ and vertical shift $v\_shift_{l,1}^{G,C}$ of the Empirical CDFs; the horizontal shift $h\_shift_{l,1}^{G,C}$ ranges from $min\{h\_shift_{l,1}^{G,C}\}$ to $max\{h\_shift_{l,1}^{G,C}\}$ with step

$$\Delta h\_shift_{l,1}^{G,C} = \frac{max\{h\_shift_{l,1}^{G,C}\} - min\{h\_shift_{l,1}^{G,C}\}}{no\ 3}, l = 1,2,3,4,5 \quad (6)$$

while the vertical shift $v\_shift_{l,1}^{G,C}$ ranges from $min\{v\_shift_{l,1}^{G,C}\}$ to $max\{v\_shift_{l,1}^{G,C}\}$ with step

$$\Delta v\_shift_{l,1}^{G,C} = \frac{max\{v\_shift_{l,1}^{G,C}\} - min\{v\_shift_{l,1}^{G,C}\}}{no\ 4}, l = 1,2,3,4,5 \quad (7)$$

where no_3 and no_4 are the number of spacings for the horizontal and vertical axis, respectively. Given the horizontal and vertical shift spacings of eqs. (6) and (7), the possible horizontal and vertical spacings can be computed by:

$$vh\_shift_{l,1,k\ no\ 3}^{G,C} = min\{h\_shift_{l,1}^{G,C}\} + k\_no\_3 \cdot \Delta h\_shift_{l,1}^{G,C}, l = 1,2,3,4,5, \quad k\_no\_3 = 0,1,\cdots,no\_3 \quad (8)$$

$$vv\_shift_{l,1,k\ no\ 4}^{G,C} = min\{v\_shift_{l,1}^{G,C}\} + k\_no\_4 \cdot \Delta v\_shift_{l,1}^{G,C}, l = 1,2,3,4,5, \quad k\_no\_4 = 0,1,\cdots,no\_4 \quad (9)$$

, respectively. In order to explain the operation of the horizontal and vertical shifts during the definition of the Empirical CDF of a virtual distribution BPL topology, there is first the need for understanding the definition of the Empirical CDF of the reference indicative distribution BPL topology by the Empirical channel attenuation statistical distribution module of Phase C, as presented in Fig. 2(b). In fact, with reference to Phase B of Fig. 2(b), Phase C receives as input the $1\times Q$ line vector coupling scheme channel attenuation difference between the reference indicative distribution BPL topology l and its respective "LOS" case, say

$$\Delta\mathbf{A}_{l,1}^{G,C}(\mathbf{f}) = -[\mathbf{H}_{l,1}^{G,C}(\mathbf{f}) - \mathbf{H}_{5,1}^{G,C}(\mathbf{f})] \quad (10)$$

In fact, the Empirical CDF $\mathbf{CDF}_{l,1}^{G,C}$ is an increasing function of the coupling scheme channel attenuation difference between the reference indicative distribution BPL topology l and its respective "LOS" case $\Delta\mathbf{A}_{l,1}^{G,C}(\mathbf{f})$ sorted in ascending order, say $\mathbf{CDF}_{l,1}^{G,C}\left(\{\Delta\mathbf{A}_{l,1}^{G,C}(\mathbf{f})\}_{\mathbf{asc}}\right)$ where $\{\cdot\}_{\mathbf{asc},q}$ is an operator that sorts a line vector in ascending order and returns the element at row q. Note that the number of elements of line vector $\{\Delta\mathbf{A}_{l,1}^{G,C}(\mathbf{f})\}_{\mathbf{asc}}$ is equal to Q reduced by the number of duplicate values dv_1. Hence, the Empirical CDF $\mathbf{CDF}_{l,1}^{G,C}$ consists of the elements $CDF_{l,1,q}^{G,C}\left(\{\Delta\mathbf{A}_{l,1}^{G,C}(\mathbf{f})\}_{\mathbf{asc},q}\right)$, $q = 1,\cdots,Q - dv_1$. At step FL2.06, all the shift pair combinations of the virtual indicative distribution BPL topologies of virtual subclasses per indicative distribution BPL topology of main subclass $[vh\_shift_{l,1,k\_no\_3}^{G,C} \quad vv\_shift_{l,1,k\_no\_4}^{G,C}], k\_no\_3 = 0,1,\cdots,no\_3, k\_no\_4 = 0,1,\cdots,no\_4$ are first computed as well as the virtual Empirical CDF $\mathbf{vCDF}_{l,1}^{G,C}$ per each shift pair combination. In general, virtual Empirical CDF is a

$(no\_3+1)\times(no\_4+1)\times(Q-dv_1-dv_2)$ array while Empirical CDF can be treated as a $1\times(Q-dv_1-dv_2)$ line vector for given horizontal and vertical shift pair. Empirical CDF consists of $vCDF_{l,1,q}^{G,C}$, $q=1,\cdots,Q-dv_1-dv_2$, is related with the Empirical CDF of the reference indicative distribution BPL topology and depends on the horizontal shift $vh\_shift_{l,1,k\ no\ 3}^{G,C}$ and vertical shift $vv\_shift_{l,1,k\ no\ 4}^{G,C}$, namely:

$$vCDF_{l,1,q}^{G,C}\left(vh\_shift_{l,1,k\_no\_3}^{G,C}, vv\_shift_{l,1,k\_no\_4}^{G,C}, max\left\{1\times10^{-11}, \left\{\Delta A_{l,1}^{G,C}(\mathbf{f})\right\}_{asc,q} + vh\_shift_{l,1,k\_no\_3}^{G,C}\right\}\right) = min\left\{CDF_{l,1,q}^{G,C}\left(\left\{\Delta A_{l,1}^{G,C}(\mathbf{f})\right\}_{asc,q}\right) + vv\_shift_{l,1,k\_no\_4}^{G,C}, 1\right\},$$
$$q=1,\cdots,Q-dv_1-dv_2, k\_no\_3=0,1,\cdots,no\_3, k\_no\_4=0,1,\cdots,no\_4 \quad (11)$$

where dv_2 is the number of duplicate values of $\mathbf{vCDF}_{l,1}^{G,C}\left(vh\_shift_{l,1,k\ no\ 3}^{G,C}, vv\_shift_{l,1,k\ no\ 4}^{G,C}\right)$.

Note that eq.(11) synopsizes all the necessary checks from FL2.06 so that valid shift pair combinations can be defined, namely:

- *Non-negative coupling scheme channel attenuation differences for the Virtual Empirical CDFs*. As already been mentioned in [17], [18], only values greater or equal than zero are expected for the coupling scheme channel attenuation differences while in the scarce cases of negative coupling scheme channel attenuation differences and in "LOS" cases, the coupling scheme channel attenuation differences are assumed to be equal to an arbitrarily low value, say 1×10^{-11}. Instead of zero, the value 1×10^{-11} has been assumed in [18] so that MLEs of Lognormal, Wald and Weibull channel attenuation distributions, which comprise natural logarithms and denominators, can be calculated and for that reason this assumption is also made in this paper through $max\left\{1\times10^{-11}, \left\{\Delta A_{l,1}^{G,C}(\mathbf{f})\right\}_{asc,q} + vh\_shift_{l,1,k\_no\_3}^{G,C}\right\}$ of eq.(11). Note that this assumption is not assumed during the computation of MLEs of indicative distribution "LOS" cases that was anyway out of the scope of [17], [18] but is of interest in these papers.
- *The maximum value of a CDF is equal to 1.* By definition, the maximum value of a CDF is equal to 1 and, for that reason, the virtual empirical CDF is upper bounded by $min\left\{CDF_{l,1,q}^{G,C}\left(\left\{\Delta A_{l,1}^{G,C}(\mathbf{f})\right\}_{asc,q}\right) + vv\_shift_{l,1,k\_no\_4}^{G,C}, 1\right\}$ of eq.(11) for given horizontal and vertical shift.

At step FL2.07, the random number generator of Phase D of Fig.2(b) exploits the Empirical CDF of the virtual indicative distribution BPL topologies of virtual main subclasses per horizontal and vertical shift set and it generates *P* members for each distribution BPL topology subclass. Finally, step FL2.08 synopsizes the operation of Phases E and F of mSHM as described in Fig. 2(b) while the output of step FL2.08 is the average capacity value average$\{C_{l,k\ no\ 3,k\ no\ 4}^{G,C,D}\}$, $k\_no\_3=0,1,\cdots,no\_3$, $k\_no\_4=0,1,\cdots,no\_4$ of each distribution BPL topology subclass. Similarly to the definition procedure of iSHM, the output of

steps FL2.06 and FL2.08 seed the Group2.C that is responsible for the mapping of the results.

3. *Group2.C*. Similarly to Group1.C of iSHM, this group consists of two steps (FL2.09 and FL2.10) and is the responsible group for the class mapping. First, step FL2.09 receives as input the output of the step FL2.06, say, all $(no\_3+1)\times(no\_4+1)$ shift pair combinations of the virtual indicative distribution BPL topologies of virtual classes per representative indicative distribution BPL topology of the main subclasses $\left[vh\_shift^{G,C}_{l,1,k\_no\_3} \quad vv\_shift^{G,C}_{l,1,k\_no\_4}\right], k\_no\_3 = 0,1,\cdots,no\_3, k\_no\_4 = 0,1,\cdots,no\_4$. Hence, the minimum and maximum values of horizontal and vertical axes of the 2D contour plot of the class map are well defined per representative indicative distribution BPL topology of the main subclasses as well as all the possible combinations of the horizontal and vertical values. This procedure is denoted as CASD parameter mapping. Second, FL2.10 receives: (i) the CASD parameters from FL2.09; and (ii) the average capacity values $\text{average}\{C^{G,C,D}_{l,k\ no\ 3,k\ no\ 4}\}, k\_no\_3 = 0,1,\cdots,no\_1, k\_no\_4 = 0,1,\cdots,no\_2$ of each distribution BPL topology subclass that correspond to all possible combinations of horizontal values k_no_3 and vertical values k_no_4. Actually, average capacities of all distribution BPL topology subclasses enrich the existing CASD parameter map of FL2.09. The existing contour plot is the subclass map that is delivered by the step FL2.11.

The last step of the definition procedure of the virtual indicative OV MV and UN MV BPL topologies and their respective virtual subclasses is step FL2.11. The output of the step FL2.11 that coincides with the output of the definition procedure of mSHM is the synthesis of inputs of the current step into a 2D contour plot. Similarly to iSHM, step FL2.11 receives the CASD parameter map from Group2.C and the capacity borders between the adjacent distribution BPL topology classes from Group2.A and gives as output the class map that is the result of the definition procedure of the virtual indicative OV MV and UN MV BPL topologies and their respective virtual subclasses of mSHM.

Synopsizing this Section, the definition procedure of the virtual indicative distribution BPL topologies and their respective virtual subclasses by adopting iSHM and mSHM allows the class enrichment with distribution BPL topologies that are statistically tested without the need for searching topological characteristic combinations that may fit any performance requirements. By consulting the class map and selecting appropriate CASD parameters, coupling channel attenuation and capacity data can be assumed for any class and further being processed. Finally, it is obvious that power grid types and the two different versions of SHM have different impact on class maps and to investigate the result behavior of the definition procedure, numerical results are presented in the companion paper of [35] for OV MV and UN MV BPL topologies. In [36], iSHM and mSHM are first applied to OV HV BPL networks while the results of the definition procedure and the class map are first demonstrated.

5. Conclusions

In this paper, the definition procedure of virtual indicative OV MV and UN MV BPL topologies and their respective virtual subclasses has been analyzed through the prism of iSHM and mSHM. In fact, on the basis of the theoretical framework and the BPMN diagrams of iSHM and mSHM, the respective definition procedure flowcharts have been proposed as well as the required theoretical framework. As the theory of the definition procedure is concerned, it has been shown that the definition procedures of iSHM and mSHM consist of three groups and eleven steps each where the statistical processing and the graphical representation of indicative distribution BPL topologies are accomplished. By exploiting the knowledge of the deterministic hybrid model, iSHM and mSHM, CASD parameter map, subclass map and class map have been proposed. Class map, which is a 2D contour plot and the output of the definition procedure, illustrates the borders between the neighboring distribution BPL topology classes and correspond each CASD parameter pair to its distribution BPL topology subclass average capacity for given power grid type, coupling scheme, IPSD limits and noise levels. The numerical results of the definition procedure are presented for distribution and transmission BPL networks in [35] and [36], respectively.

CONFLICTS OF INTEREST

The author declares that there is no conflict of interests regarding the publication of this paper.

References

[1] A. G. Lazaropoulos, "Factors Influencing Broadband Transmission Characteristics of Underground Low-Voltage Distribution Networks," *IET Commun.*, vol. 6, no. 17, pp. 2886-2893, Nov. 2012.

[2] F. Aalamifar and L. Lampe, "Optimized WiMAX profile configuration for smart grid communications," *IEEE Transactions on Smart Grid*, vol. 8, no. 6, pp. 2723-2732, 2017.

[3] A. G. Lazaropoulos, "Deployment Concepts for Overhead High Voltage Broadband over Power Lines Connections with Two-Hop Repeater System: Capacity Countermeasures against Aggravated Topologies and High Noise Environments," *Progress in Electromagnetics Research B*, vol. 44, pp. 283-307, 2012. [Online]. Available: http://www.jpier.org/PIERB/pierb44/13.12081104.pdf

[4] A. G. Lazaropoulos, "Towards Broadband over Power Lines Systems Integration: Transmission Characteristics of Underground Low-Voltage Distribution Power Lines," *Progress in Electromagnetics Research B*, vol. 39, pp. 89-114, 2012. [Online]. Available: http://www.jpier.org/PIERB/pierb39/05.12012409.pdf

[5] A. G. Lazaropoulos, "Broadband Performance Metrics and Regression Approximations of the New Coupling Schemes for Distribution Broadband over Power Lines (BPL) Networks," *Trends in Renewable Energy*, vol. 4, no. 1, pp.

43-73, Jan. 2018. [Online]. Available: http://futureenergysp.com/index.php/tre/article/view/59/pdf

[6] A. G. Lazaropoulos, "Wireless Sensor Network Design for Transmission Line Monitoring, Metering and Controlling Introducing Broadband over PowerLines-enhanced Network Model (BPLeNM)," *ISRN Power Engineering*, vol. 2014, Article ID 894628, 22 pages, 2014. doi:10.1155/2014/894628. [Online]. Available: http://www.hindawi.com/journals/isrn.power.engineering/2014/894628/

[7] A. G. Lazaropoulos, "Improvement of Power Systems Stability by Applying Topology Identification Methodology (TIM) and Fault and Instability Identification Methodology (FIIM)–Study of the Overhead Medium-Voltage Broadband over Power Lines (OV MV BPL) Networks Case," *Trends in Renewable Energy*, vol. 3, no. 2, pp. 102-128, Apr. 2017. [Online]. Available: http://futureenergysp.com/index.php/tre/article/view/34

[8] A. G. Lazaropoulos, "Main Line Fault Localization Methodology in Smart Grid–Part 1: Extended TM2 Method for the Overhead Medium-Voltage Broadband over Power Lines Networks Case," *Trends in Renewable Energy*, vol. 3, no. 3, pp. 2-25, Dec. 2017. [Online]. Available: http://futureenergysp.com/index.php/tre/article/view/36

[9] A. G. Lazaropoulos, "Main Line Fault Localization Methodology in Smart Grid–Part 2: Extended TM2 Method, Measurement Differences and L1 Piecewise Monotonic Data Approximation for the Overhead Medium-Voltage Broadband over Power Lines Networks Case," *Trends in Renewable Energy*, vol. 3, no. 3, pp. 26-61, Dec. 2017. [Online]. Available: http://futureenergysp.com/index.php/tre/article/view/37

[10] A. G. Lazaropoulos, "Main Line Fault Localization Methodology in Smart Grid–Part 3: Main Line Fault Localization Methodology (MLFLM)," *Trends in Renewable Energy*, vol. 3, no. 3, pp. 62-81, Dec. 2017. [Online]. Available: http://futureenergysp.com/index.php/tre/article/view/38

[11] A. G. Lazaropoulos, "Main Line Fault Localization Methodology (MLFLM) in Smart Grid–The Underground Medium- and Low-Voltage Broadband over Power Lines Networks Case," *Trends in Renewable Energy*, vol. 4, no. 1, pp. 15-42, Dec. 2017. [Online]. Available: http://futureenergysp.com/index.php/tre/article/view/45

[12] A. G. Lazaropoulos, "Smart Energy and Spectral Efficiency (SE) of Distribution Broadband over Power Lines (BPL) Networks – Part 1: The Impact of Measurement Differences on SE Metrics," *Trends in Renewable Energy*, vol. 4, no. 2, pp. 125-184, Aug. 2018. [Online]. Available: http://futureenergysp.com/index.php/tre/article/view/76/pdf

[13] A. G. Lazaropoulos, "Smart Energy and Spectral Efficiency (SE) of Distribution Broadband over Power Lines (BPL) Networks – Part 2: L1PMA, L2WPMA and L2CXCV for SE against Measurement Differences in Overhead Medium-Voltage BPL Networks," *Trends in Renewable Energy*, vol. 4, no. 2, pp. 185-212, Aug. 2018. [Online]. Available: http://futureenergysp.com/index.php/tre/article/view/77/pdf

[14] M. H. Rehmani, M. Reisslein, A. Rachedi, M. Erol-Kantarci, and M. Radenkovic, "Integrating renewable energy resources into the smart grid: recent developments in information and communication technologies," *IEEE Transactions on Industrial Informatics*, vol. 14, no. 7, pp. 2814-2825, 2018.

[15] F. R. Yu, P. Zhang, W. Xiao, and P. Choudhury, "Communication systems for grid integration of renewable energy resources," *IEEE Network*, vol. 25, no. 5, pp. 22–29, Sep. 2011.

[16] B. Heile, "Smart grids for green communications [industry perspectives]," *IEEE Wireless Commun.*, vol. 17, no. 3, pp. 4–6, Jun. 2010.

[17] A. G. Lazaropoulos, "Statistical Broadband over Power Lines Channel Modeling – Part 1: The Theory of the Statistical Hybrid Model," *Progress in Electromagnetics Research C*, vol. 92, pp. 1-16, 2019. [Online]. Available: http://www.jpier.org/PIERC/pierc92/01.19012902.pdf

[18] A. G. Lazaropoulos, "Statistical Broadband over Power Lines (BPL) Channel Modeling – Part 2: The Numerical Results of the Statistical Hybrid Model," *Progress in Electromagnetics Research C*, vol. 92, pp. 17-30, 2019. [Online]. Available: http://www.jpier.org/PIERC/pierc92/02.19012903.pdf

[19] A. G. Lazaropoulos, "Underground Distribution BPL Connections with (N + 1)-hop Repeater Systems: A Novel Capacity Mitigation Technique," *Elsevier Computers and Electrical Engineering*, vol. 40, pp. 1813-1826, 2014.

[20] A. G. Lazaropoulos, "Review and Progress towards the Capacity Boost of Overhead and Underground Medium-Voltage and Low-Voltage Broadband over Power Lines Networks: Cooperative Communications through Two- and Three-Hop Repeater Systems," *ISRN Electronics*, vol. 2013, Article ID 472190, pp. 1-19, 2013. [Online]. Available: http://www.hindawi.com/isrn/electronics/aip/472190/

[21] A. G. Lazaropoulos, "Broadband over Power Lines (BPL) Systems Convergence: Multiple-Input Multiple-Output (MIMO) Communications Analysis of Overhead and Underground Low-Voltage and Medium-Voltage BPL Networks (Invited Paper)," *ISRN Power Engineering*, vol. 2013, Article ID 517940, pp. 1-30, 2013. [Online]. Available: http://www.hindawi.com/isrn/power.engineering/2013/517940/

[22] A. Nazem and M. R Arshad, "An Approach in Full Duplex Digital Multipoint Systems Using Large Signal Power Line Communication," *Bentham Recent Patents on Electrical & Electronic Engineering*, vol. 6, no. 2, pp. 138-146, 2013.

[23] A. G. Lazaropoulos and P. G. Cottis, "Transmission characteristics of overhead medium voltage power line communication channels," *IEEE Trans. Power Del.*, vol. 24, no. 3, pp. 1164-1173, Jul. 2009.

[24] A. G. Lazaropoulos and P. G. Cottis, "Capacity of overhead medium voltage power line communication channels," *IEEE Trans. Power Del.*, vol. 25, no. 2, pp. 723-733, Apr. 2010.

[25] A. G. Lazaropoulos and P. G. Cottis, "Broadband transmission via underground medium-voltage power lines-Part I: transmission characteristics," *IEEE Trans. Power Del.*, vol. 25, no. 4, pp. 2414-2424, Oct. 2010.

[26] A. G. Lazaropoulos and P. G. Cottis, "Broadband transmission via underground medium-voltage power lines-Part II: capacity," *IEEE Trans. Power Del.*, vol. 25, no. 4, pp. 2425-2434, Oct. 2010.

[27] A. G. Lazaropoulos, "Broadband transmission and statistical performance properties of overhead high-voltage transmission networks," *Hindawi Journal of Computer Networks and Commun.*, 2012, article ID 875632, 2012. [Online]. Available: http://www.hindawi.com/journals/jcnc/aip/875632/

[28] A. S. de Beer, A. Sheri, H. C. Ferreira, and A. H. Vinck, "Channel frequency response for a low voltage indoor cable up to 1GHz," In *Power Line Communications and its Applications (ISPLC), 2018 IEEE International Symposium on*, pp. 1-6, 2018.

[29] A. G. Lazaropoulos, "Enhancing the Statistical Hybrid Model Performance in Overhead and Underground Medium Voltage Broadband over Power Lines Channels by Adopting Empirical Channel Attenuation Statistical Distribution," *Trends in Renewable Energy*, vol. 5, no. 2, pp. 181-217, 2019. [Online]. Available: http://futureenergysp.com/index.php/tre/article/view/96/pdf

[30] A. G. Lazaropoulos, "Towards Modal Integration of Overhead and Underground Low-Voltage and Medium-Voltage Power Line Communication Channels in the Smart Grid Landscape: Model Expansion, Broadband Signal Transmission Characteristics, and Statistical Performance Metrics (Invited Paper)," *ISRN Signal Processing*, vol. 2012, Article ID 121628, pp. 1-17, 2012. [Online]. Available: http://www.hindawi.com/isrn/sp/2012/121628/

[31] P. Amirshahi and M. Kavehrad, "High-frequency characteristics of overhead multiconductor power lines for broadband communications," *IEEE J. Sel. Areas Commun.*, vol. 24, no. 7, pp. 1292-1303, Jul. 2006.

[32] T. Sartenaer, "Multiuser communications over frequency selective wired channels and applications to the powerline access network" *Ph.D. dissertation*, Univ. Catholique Louvain, Louvain-la-Neuve, Belgium, Sep. 2004.

[33] T. Calliacoudas and F. Issa, ""Multiconductor transmission lines and cables solver," An efficient simulation tool for plc channel networks development," presented at the *IEEE Int. Conf. Power Line Communications and Its Applications*, Athens, Greece, Mar. 2002.

[34] T. Sartenaer and P. Delogne, "Deterministic modelling of the (Shielded) outdoor powerline channel based on the multiconductor transmission line equations," *IEEE J. Sel. Areas Commun.*, vol. 24, no. 7, pp. 1277-1291, Jul. 2006.

[35] A. G. Lazaropoulos, "Virtual Indicative Broadband over Power Lines Topologies for Respective Subclasses by Adjusting Channel Attenuation Statistical Distribution Parameters of Statistical Hybrid Models – Part 2: Numerical Results for the Overhead and Underground Medium-Voltage Power Grids," *Trends in Renewable Energy*, vol. 5, no. 3, pp 258-281, Aug. 2019. DOI: 10.17737/tre.2019.5.3.00100

[36] A. G. Lazaropoulos, "Virtual Indicative Broadband over Power Lines Topologies for Respective Subclasses by Adjusting Channel Attenuation Statistical Distribution Parameters of Statistical Hybrid Models – Part 3: The Case of Overhead Transmission Power Grids," *Trends in Renewable Energy*, vol. 5, no. 3, pp 282-306, Aug. 2019. DOI: 10.17737/tre.2019.5.3.00101

[37] Matlabtricks (2014) Generate random numbers with a given distribution, http://matlabtricks.com/post-44/generate-random-numbers-with-a-given-distribution (accessed on 8/14/2019)
[38] J. Denker (2008) Randomly Generating Numbers with an Arbitrary Distribution http://www.av8n.com/physics/arbitrary-probability.htm (accessed on 8/14/2019)

Trends in Renewable Energy
OPEN ACCESS ISSN: 2376-2144
Peer-Reviewed Article futureenergysp.com/index.php/tre

Virtual Indicative Broadband over Power Lines Topologies for Respective Subclasses by Adjusting Channel Attenuation Statistical Distribution Parameters of Statistical Hybrid Models (Class Maps) – Part 2: Numerical Results for the Overhead and Underground Medium-Voltage Power Grids

Athanasios G. Lazaropoulos*

School of Electrical and Computer Engineering / National Technical University of Athens / 9 Iroon Polytechniou Street / Zografou, GR 15780

Received June 21, 2019; Accepted August 12, 2019; Published August 16, 2019

With reference to the initial statistical hybrid model (iSHM) and modified statistical hybrid model (mSHM), the theory of the definition procedure of new virtual indicative distribution BPL topologies by appropriately adjusting the channel attenuation statistical distributions (CASDs) parameters of iSHM and mSHM has been presented in [1]. In this paper, the results of the definition procedure for the OV and UN MV BPL networks are first presented through the prism of the proposed class maps of iSHM and mSHM.

Keywords: Smart Grid; Broadband over Power Lines (BPL) networks; Power Line Communications (PLC); Distribution Power Grids; Capacity; Statistics; Modeling

1. Introduction

This set of papers deals with two fervent issues of the broadband over power lines (BPL) statistical channel modelling, say: (i) the underrepresentation of the BPL topology classes during the BPL statistical channel modelling through the insertion of virtual indicative BPL topologies and their respective subclasses; and (ii) the graphical representation of the BPL topology classes and subclasses in terms of their average capacity through the proposed class maps of the first paper [1]. First, as the BPL statistical channel modelling is concerned, two versions of the hybrid statistical model have already been proposed, say the initial statistical hybrid model (iSHM), which has been presented in [2], [3], and the modified statistical hybrid model (mSHM), which has been presented in [4]. The basic component of both hybrid statistical models is the deterministic hybrid model that has exhaustively been validated in a plethora of transmission and distribution BPL network cases [5]-[15]. Apart from the deterministic hybrid model, iSHM applies five well-known channel attenuation statistical distribution (CASDs) of the communications literature, say, Gaussian, Lognormal, Wald, Weibull and Gumbel ones [2], [3], while mSHM applies the Empirical CASD [4] so that BPL topology classes *–i.e.*, rural, suburban, urban and aggravated urban subclass– and

**Corresponding author:* AGLazaropoulos@gmail.com

Tr Ren Energy, 2019, Vol.5, No.3, 258-281. doi: 10.17737/tre.2019.5.3.00100

respective subclasses can be defined. Second, as the underrepresentation of the BPL topology classes is concerned, by appropriately adjusting the CASD parameters of iSHM and mSHM –*i.e.*, CASD maximum likelihood estimators (MLEs) and Empirical cumulative density function (CDF) for iSHM and mSHM, respectively–, new virtual indicative distribution BPL topologies can be proposed that are added to the existing real ones and further define their respective distribution BPL topology subclasses enriched with corresponding statistically equivalent BPL topologies. In [1], the theoretical framework for the definition procedure of the virtual indicative BPL topologies and their respective virtual subclasses, briefly denoted as definition procedure hereafter, has been detailed. Third, as the graphical capacity representation of the real and virtual subclasses is concerned, the main output of the definition procedure of [1] is the class map, which is a 2D contour plot for given power grid type, coupling scheme, injected power spectral density (IPSD) limits and noise levels, that is the graphical synthesis of the CASD parameter and subclass map; say, real and virtual distribution BPL subclasses are graphically categorized into suitable BPL topology class areas in terms of their corresponding average capacities where the axes of the contour plot are proper adjustments of CASD parameters of iSHM and mSHM. The numerical results of the full deployment of class mapping are first presented in this paper for overhead medium voltage (OV MV) and underground medium voltage (UN MV) BPL networks while the BPL statistical channel modelling concept along with the class map is first applied to OV high-voltage (HV) BPL networks in [16].

The rest of this paper is organized as follows: Section II synopsizes the default settings that are required for the fine operation of the deterministic hybrid model, iSHM, mSHM and the definition procedure. In Section III, the numerical results of the definition procedure of iSHM and mSHM are demonstrated on the basis of the class maps of the OV MV and UN MV BPL networks. Section IV concludes this paper.

2. The Operation Settings of Class Mapping

To coexist the deterministic hybrid model, iSHM and mSHM with the definition procedure, a set of operation settings, which have already been reported in [2]-[4], should be assumed. In this Section, a synopsis of these assumptions is given as well as the set of scenarios that is studied in this paper.

2.1 Operation Settings Concerning the Operation of the Deterministic Hybrid Model

With reference to Fig. 1 of [1], the five indicative OV MV and UN MV BPL topologies, which are reported in Tables 1 and 2 of [1], respectively, are considered as the representative ones of the respective main OV MV and UN MV BPL topology subclasses. Note that with reference to [5], [8], [10], [17], the indicative OV MV and UN MV BPL topologies concern average long end-to-end connections of 1000m and 200m, respectively.

As the the circuital parameters of the above indicative OV MV and UN MV BPL topologies are concerned for the operation of the deterministic hybrid model, these are detailed in [5], [7]-[15], [18]-[33]. Synoptically, the required assumptions can be

synopsized as follows: (i) the branching cables are assumed identical to the distribution cables; (ii) the interconnections between the distribution and branch conductors are fully activated; say all the phase and the neutral conductors of the branching cables are connected to the respective ones of the distribution cables; (iii) the transmitting and the receiving ends are assumed matched to the characteristic impedance of the modal channels; and (iv) the branch terminations are assumed open circuit since MV/LV transformers are assumed to be installed.

2.2 iSHM Operation Settings

Already been identified in [3], the distribution power grid type, the BPL topology class, CASD, electromagnetic interference (EMI) policy, noise level and applied coupling scheme are factors that should be carefully selected during the operation of the deterministic hybrid model and iSHM. Hence, additional details should be given for iSHM operation settings as reported in this subsection.

First, the BPL operation frequency range and the flat-fading subchannel frequency spacing are assumed to be equal to 3-30 MHz and 0.1 MHz (i.e, f_s =0.1 MHz), respectively. Hence, there are 270 subchannels in the frequency range of interest (*i.e.*, Q =270). In accordance with [8], [10], [11], [19], [21], [34], the assumption of the flat-fading subchannels, which is a typical scenario, remains a crucial element towards the capacity computation of the examined distribution BPL topologies, that is anyway the output measure of iSHM.

Second, to compute coupling scheme channel attenuations of the distribution BPL topologies, CS2 module, which has been detailed in [35], [36], is applied as the default coupling scheme system of the deterministic hybrid model. Among the available coupling schemes that are supported by CS2 module, WtG[1] and StP[1] coupling schemes are assumed to be the default ones for the assessment of OV MV and UN MV BPL topology subclasses, respectively, so that a direct comparison between the results of this paper and those of [3] and [4], can be achieved.

Third, during the computation of the coupling scheme channel attenuation differences in the Phase B of [2], values that are greater or equal to zero are expected in the vast majority of the cases. However, in the scarce cases of negative coupling scheme channel attenuation differences and in "LOS" cases, the coupling scheme channel attenuation differences are assumed to be equal to an arbitrarily low value, say 1×10^{-11}. This assumption is made in order to prevent the presence of infinite terms due to the natural logarithms and denominators of Lognormal, Wald and Weibull channel attenuation distributions in iSHM.

Fourth, as the members of each BPL topology subclass are concerned in Phase D, 100 member distribution BPL topologies (*i.e.*, P=100) are assumed to be added in each BPL topology subclass per CASD through the statistical hybrid model procedure described in [2].

Fifth, during the capacity computations of iSHM, FCC Part 15 is considered as the default IPSD limit proposal concerning EMI policies for BPL systems in this paper. Among the available EMI policies, which are FCC Part 15, German Reg TP NB30 and the BBC / NATO Proposal and their impact on the performance of hybrid statistical models has already been studied in [3], [4], FCC Part 15 is assumed to be the default EMI policy in this paper due to its proneness to the broadband character of BPL networks and

its high performance results of statistical hybrid models. In the frequency range 3-30 MHz of this paper, -60 dBm/Hz and -40 dBm/Hz are the FCC Part 15 IPSD limits $p(\cdot)$ suitable for the operation of OV MV and UN MV BPL topologies, respectively [8], [10], [37].

Sixth, during the capacity computations, uniform additive white Gaussian noise (AWGN) PSD levels are assumed in accordance with the FL noise model of [38], [39]. As it regards the noise properties of OV MV and UN MV BPL networks in the 3-30MHz frequency range [8], [10], [19], [34], [40], -105dBm/Hz and -135dBm/Hz are the appropriate AWGN PSD limit levels $N(\cdot)$ for OV MV and UN MV BPL networks, respectively.

Seventh, in accordance with [3], [4], the performance of iSHM and the accuracy of its capacity results significantly depend on the selection of the CASD. Based on the findings of Table 3 of [3], it has been demonstrated for the iSHM that Weibull and Wald CASDs perform the best capacity estimations in OV MV and UN MV power grid types, respectively, regardless of the examined BPL topology subclass when the aforementioned operation settings concerning EMI policy, noise level and applied coupling scheme are assumed. These two CASDs are going to be only adopted by the following definition procedure and during the iSHM study in this paper.

2.3 mSHM Operation Settings

Similarly to iSHM, the distribution power grid type, the BPL topology class, the reference indicative distribution BPL topology, EMI policy, noise level and applied coupling scheme are factors that are involved during the operation of the deterministic hybrid model and mSHM [4]. In contrast with iSHM operation settings, only one CASD, say, the Empirical CASD, is adopted by mSHM by default and, hence, CASD selection is not considered among the mSHM operation settings.

As the BPL operation frequency range, flat-fading subchannel spacing, coupling scheme system, the member number of each BPL topology subclass, EMI policy and noise level are considered, their properties described in Sec. 2.2 for iSHM are assumed to be the same with the ones of mSHM. For comparison reasons between iSHM and mSHM and in accordance with [2], [3], [4], the infinity prevention assumption remains for the mSHM.

In general, each indicative distribution BPL topology is characterized by a set of parameters regarding either iSHM (*i.e.*, MLEs) or mSHM (*i.e.*, Empirical CDF). As already been mentioned in Sec.2.2 for iSHM, Weibull and Wald CASD MLEs perform the best capacity estimations in OV MV and UN MV power grid types, respectively, and these MLEs are going to be adopted for the rest of this paper. As mSHM CASD parameters are concerned, the Empirical CDF of a reference distribution BPL topology among the indicative distribution BPL topologies of the main subclasses acts as the mSHM CASD parameter that is going to be delivered to the following definition procedure.

2.4 Operation Settings for the Definition Procedure

In accordance with [1], the BPMN diagrams of iSHM and mSHM flowchart are presented in Figs. 2(a) and 2(b) of [1], respectively. With reference to the aforementioned figures, the additional BPMN elements (*i.e.*, the virtual topology modules and their

corresponding outputs), which will allow the application of the definition procedure, are shown in red color. Apart from the BPMN diagrams, the interaction of the virtual topology modules with the remaining iSHM and mSHM steps is depicted through the flowcharts of Figs. 3(a) and 3(b) of [1], respectively. By comparing Figs. 3(a) and 3(b) of [1], several differences concerning these flowcharts can be observed, especially: (i) between steps FL1.04 and FL2.04; and (ii) between steps FL1.05 and FL2.05. Due to the previous differences, the operation settings concerning the definition procedure can be divided into two groups, namely:

1. *iSHM definition procedure*: With reference to [2], [3], since Weibull CASD performs the best capacity estimations in OV MV BPL networks, $\hat{\alpha}_{\mathbf{MLE}}^{\mathbf{Weibull}}$ and $\hat{\beta}_{\mathbf{MLE}}^{\mathbf{Weibull}}$ are Weibull CASD MLEs that are used in FL1.04 of Fig. 3(a) of [1]. When UN MV BPL topologies are studied, $\hat{\mu}_{\mathbf{MLE}}^{\mathbf{Wald}}$ and $\hat{\lambda}_{\mathbf{MLE}}^{\mathbf{Wald}}$ are the Wald CASD MLEs that are used in FL1.04 of Fig. 3(a) of [1]. In accordance with FL1.04 of Fig. 3(a) of [1], MLEs of the indicative distribution BPL topologies of main subclasses are computed. To compute the MLE spacings per distribution power grid type in FL1.05 of Fig. 3(a) of [1], no_1 and no_2, which are the number of spacings for the horizontal and vertical axis, respectively, should be assumed. In this paper, the number of spacings for the horizontal and vertical axis is assumed to be equal to 10 in both cases regardless of the distribution power grid type while this selection is going to be proven critical for the simulation time of class mapping (see Sec.3.5).
2. *mSHM definition procedure*: In contrast with iSHM definition procedure, there is only one CASD that is used across the mSHM definition procedure, say Empirical CASD, but Empirical CASD is characterized by its CDF and not by corresponding MLEs [4]. In accordance with FL2.04 of Fig. 3(b) of [1], Empirical CDFs of the indicative distribution BPL topologies of main subclasses are computed. Conversely to iSHM, mSHM definition procedure demands the assumption of a reference indicative distribution BPL topology among the indicative ones so that suitable horizontal and vertical shifts can be added and the class map can be plotted. To compute the horizontal and vertical shift spacings in FL2.05 of Fig. 3(b) of [1] given the reference indicative distribution BPL topology, no_3 and no_4, which are the number of spacings for the horizontal and vertical axis, respectively, should be assumed. In this paper, the number of spacings for the horizontal and vertical axis is assumed to be equal to 10 in both cases regardless of the distribution power grid type examined. At this step of the definition procedure, same number of horizontal and vertical spacings is considered between iSHM and mSHM definition procedures for duration comparison reasons. Note that the maximum and minimum horizontal shift is assumed to be equal to 30 dB and -30 dB, respectively, while the maximum and minimum vertical shift is assumed to be equal to 1 and 0, respectively.

Since all the required assumptions concerning the operation settings of iSHM, mSHM and definition procedure have been reported in this Section, the numerical results of iSHM and mSHM definition procedure are presented in the following Section for the OV MV and UN MV BPL topologies as well as the class maps.

3. Numerical Results and Discussion

In this Section, numerical results concerning the definition procedure of iSHM and mSHM are presented. Taking into account the already identified default operation settings of Secs.2.1-2.4, four different scenarios concerning the class mapping are presented, namely: (i) iSHM definition procedure for OV MV BPL topologies; (ii) iSHM definition procedure for UN MV BPL topologies; (iii) mSHM definition procedure for OV MV BPL topologies; and (iv) mSHM definition procedure for UN MV BPL topologies. This Section ends with observations concerning the simulation time of the aforementioned four scenarios.

3.1 iSHM Definition Procedure for OV MV BPL topologies

With reference to Table 3 of [3], Weibull CASD achieves the best capacity estimations in OV MV BPL topologies with average absolute percentage change that is equal to 0.47% and remains the smallest one among the five examined CASDs. For the five indicative OV MV BPL topologies of the main subclasses of Table 1 of [1], the respective $\hat{\alpha}_{\mathbf{MLE}}^{\mathbf{Weibull}}$ and $\hat{\beta}_{\mathbf{MLE}}^{\mathbf{Weibull}}$, which are the Weibull CASD MLEs, are reported in Table 1 of [3] while the respective capacities are given in Table 3 of [3]. On the basis of the Weibull CASD MLEs and capacities of the five indicative OV MV BPL topologies of the main subclasses of Table 1 of [1], the spacings for the horizontal and vertical axis, as dictated by FL1.05 of Fig. 3(a) of [1], are equal to $\frac{19.40-1\times10^{-11}}{10}=1.94$ and $\frac{1.34-0}{10}=0.134$, respectively, while the capacity borders between the adjacent distribution BPL topology classes $CBo_l^{G,C}, l=1,2,3,4$, as dictated by FL1.03 of Fig. 3(a) of [1], are equal to 245Mbps, 289Mbps, 332Mbps and 379Mbps, respectively. Summarizing the aforementioned analysis, the class map of OV MV BPL topologies is plotted in Fig. 1 with respect to $\hat{\alpha}_{\mathbf{MLE}}^{\mathbf{Weibull}}$ and $\hat{\beta}_{\mathbf{MLE}}^{\mathbf{Weibull}}$ when the operation settings of Sec.2 are assumed. In the same 2D contour plot, the Weibull CASD MLEs of the five indicative OV MV BPL topologies of the main subclasses of Table 1 of [1] with the corresponding capacities are also shown.

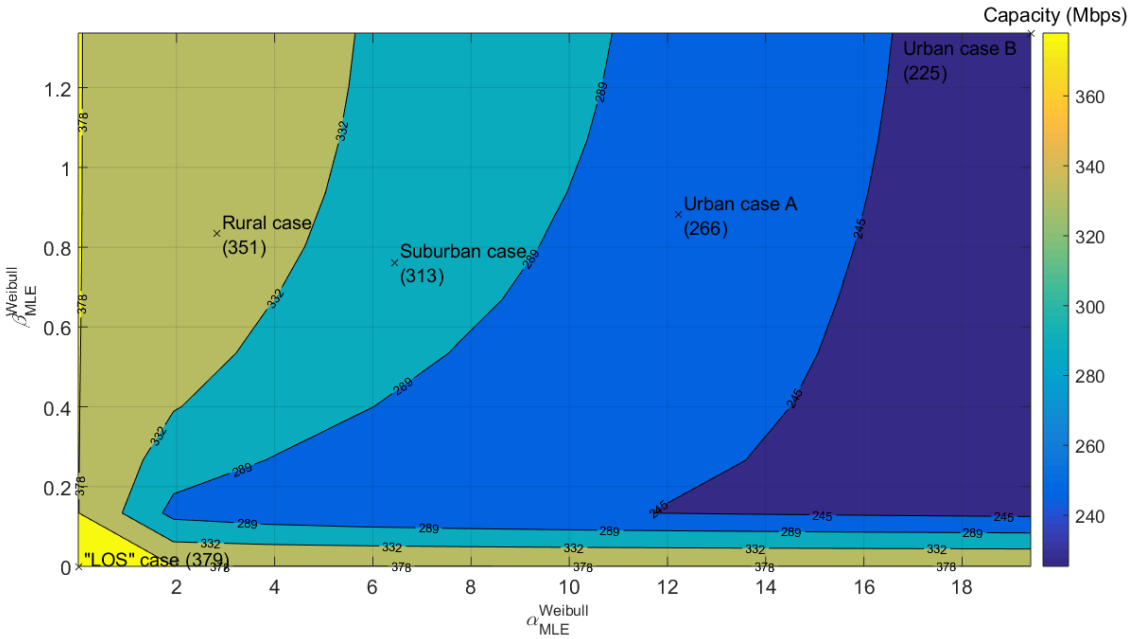

Fig. 1. iSHM class map of the OV MV BPL topologies in the 3-30MHz frequency band when WtG[1] coupling scheme is deployed and FCC Part 15 is applied.

By observing Fig. 1, several useful findings can be pointed out for the class map of iSHM, namely:

- Different combinations of Weibull CASD MLEs entail different capacities for the corresponding virtual OV MV BPL topologies. With reference to the computed capacity borders between the adjacent distribution BPL topology classes, five capacity areas between these borders can be clearly delineated in the class map; say, the OV MV BPL "LOS" class, OV MV BPL rural class, OV MV BPL suburban class, OV MV BPL urban case A class and OV MV BPL urban case B class.
- As it is obvious, the indicative OV MV BPL topologies of the main subclasses of Table 1 of [1] are located in the homonymous title class areas. Note that the $\hat{\beta}_{\mathbf{MLE}}^{\mathbf{Weibull}}$ value of the OV MV BPL "LOS" case has been arbitrarily chosen to be equal to zero since a narrow OV MV BPL "LOS" class area extents from the zero value up to the infinity of $\hat{\beta}_{\mathbf{MLE}}^{\mathbf{Weibull}}$. Similarly, a narrow OV MV BPL "LOS" class area extents from the zero value up to the infinity of $\hat{\alpha}_{\mathbf{MLE}}^{\mathbf{Weibull}}$ creating a capacity fluctuation till the second $\hat{\beta}_{\mathbf{MLE}}^{\mathbf{Weibull}}$ value of study (say, second $\hat{\beta}_{\mathbf{MLE}}^{\mathbf{Weibull}}$ value is equal to 0.134). In mathematical terms, this is explained by the definition of the Weibull CASD CDF in eqs. (A10)-(A12) of [2] and the involvement of $\hat{\alpha}_{\mathbf{MLE}}^{\mathbf{Weibull}}$ and $\hat{\beta}_{\mathbf{MLE}}^{\mathbf{Weibull}}$.
- As the multipath environment of the examined OV MV BPL topologies becomes richer (*i.e.*, more frequent and deeper spectral notches [5]-[6], [9], [41]), this has as a result the value increase of $\hat{\alpha}_{\mathbf{MLE}}^{\mathbf{Weibull}}$. Hence, OV MV BPL urban topologies tend to be located at the upper right areas of the class map while the OV MV BPL rural topologies tend to be located at the lower left areas. Anyway, $\hat{\alpha}_{\mathbf{MLE}}^{\mathbf{Weibull}}$ is

more sensitive to the multipath environment aggravation in contrast with $\hat{\beta}_{\mathbf{MLE}}^{\mathbf{Weibull}}$ that remains relatively insensitive. The last remark is validated by the fact that indicative OV MV BPL rural, OV MV BPL suburban and OV MV BPL urban case A topologies of Table 1 of [1] are characterized by approximately equal values of $\hat{\beta}_{\mathbf{MLE}}^{\mathbf{Weibull}}$.

- Note that for given $\hat{\alpha}_{\mathbf{MLE}}^{\mathbf{Weibull}}$, the capacity of the virtual OV MV BPL topologies increases with respect to the $\hat{\beta}_{\mathbf{MLE}}^{\mathbf{Weibull}}$. This is explained by studying Fig. (2) of [4], eq. (A10) of [2] and the behavior of Weibull CASD CDF; since $\hat{\alpha}_{\mathbf{MLE}}^{\mathbf{Weibull}}$ receives values that are significantly greater than 1 for the practical cases of interest, the term $\frac{\Delta A_q}{\hat{\alpha}_{\mathbf{MLE}}^{\mathbf{Weibull}}}$ of eq. (10) of [2] can be considered to be greater than 1 in the majority of the cases examined in Fig. (2) of [4] where ΔA_q is the coupling scheme channel attenuation difference between the examined OV MV BPL topology and its respective "LOS" case at q flat-fading subchannel. As $\hat{\alpha}_{\mathbf{MLE}}^{\mathbf{Weibull}}$ increases, $-\left(\frac{\Delta A_q}{\hat{\alpha}_{\mathbf{MLE}}^{\mathbf{Weibull}}}\right)^{\hat{\beta}_{\mathbf{MLE}}^{\mathbf{Weibull}}}$ increases from -1 to infinity and, thus, $1-exp\left[-\left(\frac{\Delta A_q}{\hat{\alpha}_{\mathbf{MLE}}^{\mathbf{Weibull}}}\right)^{\hat{\beta}_{\mathbf{MLE}}^{\mathbf{Weibull}}}\right]$ starts from $[1-exp(-1)]$ and fast tends to 1. The last observation has as a result the improvement of the capacities of the virtual OV MV BPL topologies that are characterized by greater $\hat{\beta}_{\mathbf{MLE}}^{\mathbf{Weibull}}$ values for given $\hat{\alpha}_{\mathbf{MLE}}^{\mathbf{Weibull}}$. Anyway, the capacity improvement is more evident for the cases of low $\hat{\alpha}_{\mathbf{MLE}}^{\mathbf{Weibull}}$ because the term $\frac{\Delta A_q}{\hat{\alpha}_{\mathbf{MLE}}^{\mathbf{Weibull}}}$ remains significantly greater than 1 and this explains the appearance of the class area edges at the bottom of the class map and the steep and almost vertical class area borders for $\hat{\beta}_{\mathbf{MLE}}^{\mathbf{Weibull}}$ greater than 1.2.

3.2 iSHM Definition Procedure for UN MV BPL topologies

With reference to Table 3 of [3], Wald CASD achieves the best capacity estimations in UN MV BPL topologies with average absolute percentage change that is equal to 0.01% and remains the smallest one among the five examined CASDs. For the five indicative UN MV BPL topologies of the main subclasses of Table 2 of [1], the respective $\hat{\mu}_{\mathbf{MLE}}^{\mathbf{Wald}}$ and $\hat{\lambda}_{\mathbf{MLE}}^{\mathbf{Wald}}$, which are the Wald CASD MLEs, are reported in Table 1 of [3] while the respective capacities are given in Table 3 of [3]. By observing the extent of $\hat{\lambda}_{\mathbf{MLE}}^{\mathbf{Wald}}$ values of Table 2 of [1], which ranges from 20.93 to 2.62×10^3, and taking under consideration the number of spacings that is equal to 10, the proper selection for the vertical axis is the representation of $\left(\hat{\lambda}_{\mathbf{MLE}}^{\mathbf{Wald}}\right)^{-1}$ and the corresponding vertical spacings. Therefore, on the basis of the Wald CASD MLEs and capacities of the five indicative OV MV BPL topologies of the main subclasses of Table 2 of [1], the spacings for the horizontal and vertical axis, as dictated by FL1.05 of Fig. 3(a) of [1], are equal to $\frac{19.96-1\times10^{-6}}{10}=1.996$ and $\frac{\left(\frac{1}{20.93}\right)-\left(\frac{1}{2.62\times10^3}\right)}{10}=0.0047$, respectively, while the capacity borders between the adjacent distribution BPL topology classes $CBo_l^{C,C}, l=1,2,3,4$, as dictated by FL1.03 of Fig. 3(a) of [1], are equal to 561Mbps, 619Mbps, 651Mbps and 699Mbps, respectively. Summarizing the aforementioned analysis, the class map of UN MV BPL topologies is plotted in Fig. 2 with respect to

$\hat{\mu}_{\mathbf{MLE}}^{\mathbf{Wald}}$ and $\left(\hat{\lambda}_{\mathbf{MLE}}^{\mathbf{Wald}}\right)^{-1}$ when the operation settings of Sec.2 are assumed. In the same 2D contour plot, the Wald CASD MLEs of the five indicative UN MV BPL topologies of the main subclasses of Table 2 of [1] with the corresponding capacities are also shown.

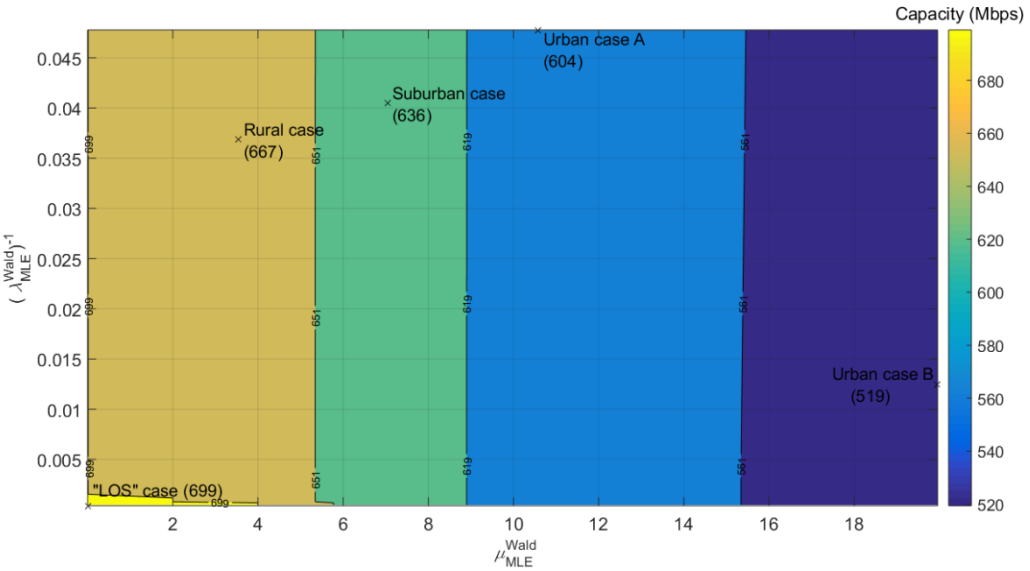

Fig. 2. iSHM class map of the UN MV BPL topologies in the 3-30MHz frequency band when StP[1] coupling scheme is deployed and FCC Part 15 is applied.

By observing Fig. 2, additional findings for the class map of iSHM can be added to the ones of Sec. 3.1, namely:

- Similarly to the iSHM class map of OV MV BPL topologies, five capacity areas between the computed borders are clearly delineated in the iSHM class map of UN MV BPL topologies; say, the UN MV BPL "LOS" class, UN MV BPL rural class, UN MV BPL suburban class, UN MV BPL urban case A class and UN MV BPL urban case B class. Each of the five capacity areas consists of the homonymous indicative UN MV BPL topology of Table 2 of [1]. Also, in accordance with eq. (A7) of [2], a narrow UN MV BPL "LOS" class area extents from zero up to the infinity when $\hat{\mu}_{\mathbf{MLE}}^{\mathbf{Wald}}$ is equal to zero. This is explained by studying eq. (A7) of [2] and the behavior of Wald CASD CDF; since $\hat{\mu}_{\mathbf{MLE}}^{\mathbf{Wald}}$ receives values that are significantly greater than 0 for the practical cases of interest, the terms where $\hat{\mu}_{\mathbf{MLE}}^{\mathbf{Wald}}$ is involved as a denominator receive values that are different than infinity. The zero theoretical value of $\hat{\mu}_{\mathbf{MLE}}^{\mathbf{Wald}}$ entails the special behaviors of the Wald CASD CDF and capacity regardless of the $\left(\hat{\lambda}_{\mathbf{MLE}}^{\mathbf{Wald}}\right)^{-1}$ value.
- As the multipath environment of the examined UN MV BPL topologies becomes richer (*i.e.*, more frequent and deeper spectral notches [7], [9], [5], [6], [41]), this has as a result the value increase of $\hat{\mu}_{\mathbf{MLE}}^{\mathbf{Wald}}$. Hence, UN MV BPL urban topologies tend to be located at the right areas of the class map while the UN MV BPL rural topologies tend to be located at the left areas. Similarly to the class map of OV

MV BPL topologies, $\hat{\mu}_{\mathbf{MLE}}^{\mathbf{Wald}}$ behaves similarly to $\hat{a}_{\mathbf{MLE}}^{\mathbf{Weibull}}$ (*i.e.*, CASD MLEs that are sensitive to the multipath environment aggravation) while $\left(\hat{\lambda}_{\mathbf{MLE}}^{\mathbf{Wald}}\right)^{-1}$ behaves similarly to $\hat{\beta}_{\mathbf{MLE}}^{\mathbf{Weibull}}$ (*i.e.*, CASD MLEs that do not depend on the multipath environment aggravation). Conversely to iSHM class map of OV MV BPL topologies, iSHM class map of UN MV BPL topologies does not comprise class area edges of the extent demonstrated in OV MV BPL topologies.

3.3 mSHM Definition Procedure for OV MV BPL topologies

With reference to Table 3 of [4], Empirical CASD of mSHM achieves better capacity estimations than the ones of Weibull CASD of iSHM in OV MV BPL topologies when OV MV BPL urban case A, OV MV BPL suburban case and OV MV BPL rural case are examined while the capacity estimation difference between Empirical and Weibull CASDs remains relatively small when OV MV BPL urban case B is examined. In total, Empirical CASD of mSHM achieves better average absolute percentage change (*i.e.*, 0.09%) than Weibull CASD of iSHM (*i.e.*, 0.47%).

In accordance with [1], similarly to the role of CASD selection of iSHM, the selection of the reference distribution BPL topology among the available indicative distribution BPL topologies of the main subclasses defines the class map of mSHM. In contrast with iSHM where one CASD excels over the others in terms of the capacity estimation performance (say, Weibull CASD and Wald CASD for the OV MV and UN MV BPL topologies, respectively) and is finally selected, all the four indicative OV MV BPL topologies of the main subclasses of Table 1 of [1], except for the OV MV "LOS" case, should be examined separately during the preparation of mSHM class maps.

For the reference indicative OV MV BPL urban case A of Table 1 of [1], the horizontal shift $h\_shift_{1,1}^{\mathbf{C,C}}$ and vertical shift $v\_shift_{1,1}^{\mathbf{C,C}}$ of its corresponding Empirical CDF, hereafter denoted simply as h_shift and v_shift, respectively, are assumed to be both equal to zero while the respective capacity is given in Table 3 of [3]. On the basis of the horizontal and vertical shifts of the Empirical CDF and the capacity of the reference indicative OV MV BPL urban case A, the spacing for the horizontal axis $\Delta h\_shift_{1,1}^{\mathbf{C,C}}$ and the spacing for the vertical axis $\Delta v\_shift_{1,1}^{\mathbf{C,C}}$, as dictated by FL2.05 of Fig. 3(b) of [1], are equal to $\frac{30-(-30)}{10} = 0.6$ and $\frac{1-0}{10} = 0.1$, respectively, while the capacity borders between the adjacent distribution BPL topology classes $CBo_l^{\mathbf{C,C}}, l = 1, 2, 3, 4$, as dictated by FL2.03 of Fig. 3(a) of [1], are equal to 245Mbps, 289Mbps, 332Mbps and 379Mbps, respectively. Note that the capacity borders between the adjacent distribution BPL topology classes remain the same during the design of iSHM and mSHM class maps. Summarizing the aforementioned analysis, the class map of OV MV BPL topologies is plotted in Fig. 3(a) with respect to the horizontal shift h_shift and vertical shift v_shift when the operation settings of Sec.2 are assumed. In the same 2D contour plot, the capacity borders between the adjacent distribution BPL topology classes and the capacity of the reference indicative OV MV BPL urban case A of Table 1 of [1] are also shown. In Figs. 3(b)-(d), same plots with Fig. 3(a) are given but for the case of the reference indicative urban case B, suburban case and rural case of Table 1 of [1], respectively.

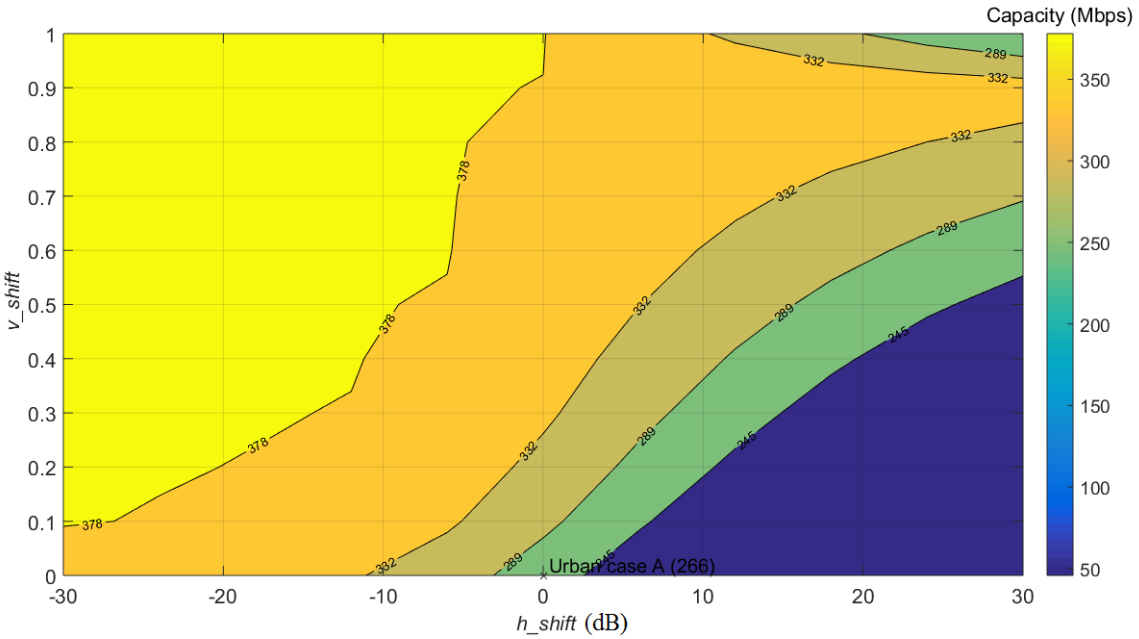
Capacity (Mbps)
v_shift
h_shift (dB)
Urban case A (266)

(a)

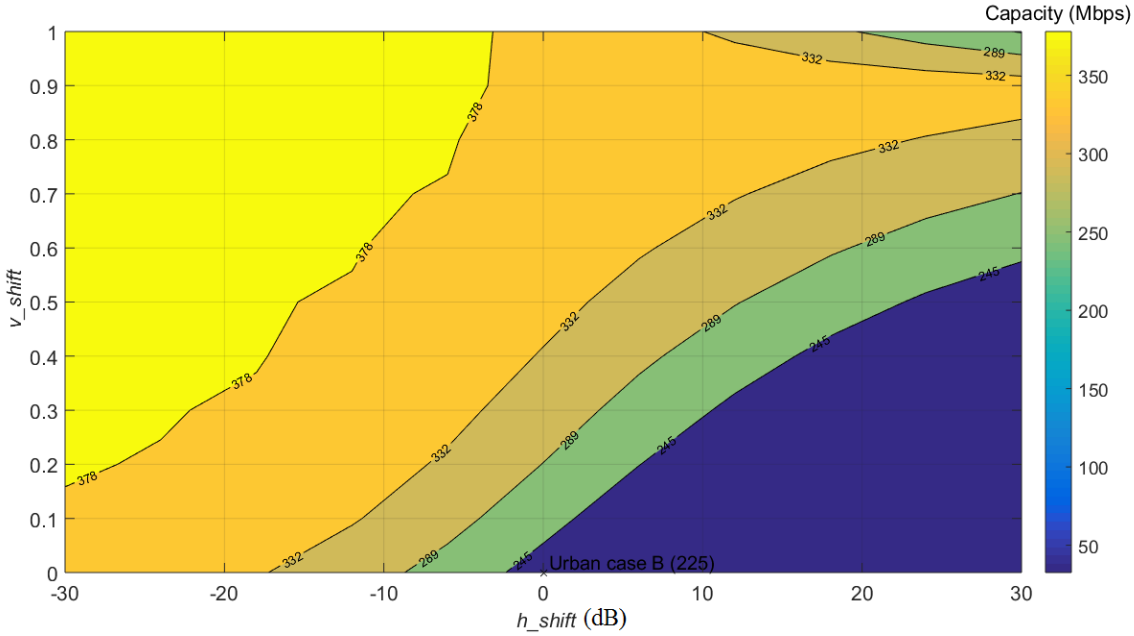
Capacity (Mbps)
v_shift
h_shift (dB)
Urban case B (225)

(b)

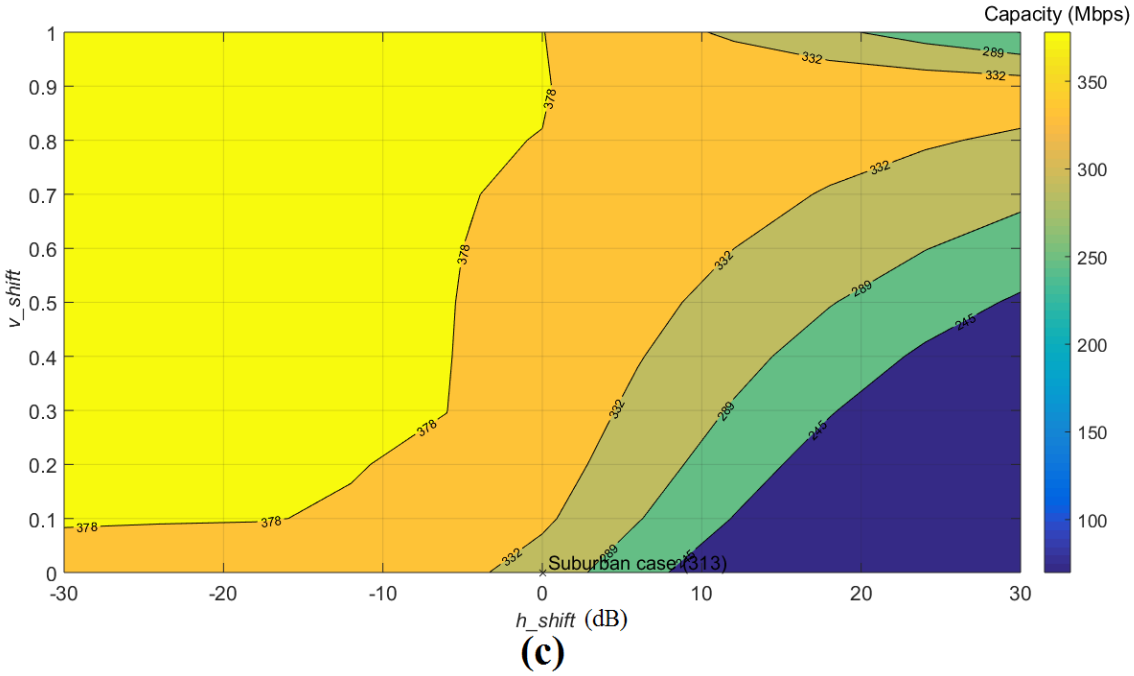

Fig. 3. mSHM class map of the OV MV BPL topologies in the 3-30MHz frequency band when WtG[1] coupling scheme is deployed and FCC Part 15 is applied for different reference indicative OV MV BPL topologies. (a) OV MV BPL urban case A. (b) OV MV BPL urban case B. (c) OV MV BPL suburban case. (d) OV MV BPL rural case.

From Figs. 3(a)-(d), several interesting remarks can be pointed out concerning the mSHM class maps, namely:

- Similarly to the iSHM class map of OV MV BPL topologies, five capacity areas between the computed borders can be clearly delineated in the mSHM class map

of OV MV BPL topologies; say, the OV MV BPL "LOS" class, OV MV BPL rural class, OV MV BPL suburban class, OV MV BPL urban case A class and UN MV BPL urban case B class. The virtual OV MV BPL topologies that are members of the aforementioned OV MV BPL topology classes can be defined by the suitable combined horizontal and vertical shift adjustment of the reference indicative OV MV BPL topology with reference to Figs. 3(a)-(d).

- As the procedure of the Empirical CDF shifting is concerned in this paper, the vertical shift is first taken into account and the horizontal shift is second executed. This sequence of shifts ensures that the shape of the Empirical CDF retains its characteristics as reported in eq.(11) of [1] and its accompanying two restrictions regarding the definition of valid shift pair combinations. Anyway, since the vertical and horizontal shifts can be considered as linear transformations of the Empirical CDFs, the sequence of shifts can be reversed without class map modifications if the new horizontal values are not modified during the vertical shifts.
- The vertical shifts that are assumed during the preparation of the mSHM class maps are considered to be positive and range from 0 to 1 while the horizontal shifts are assumed to range from -30 dB to 30 dB regardless of the examined distribution BPL topology. As the vertical shifts are concerned, the positive values up to 1, which are combined with the CDF maximum value restriction of 1, imply that the virtual Empirical CDF that is produced after the valid shift pair combination reaches up to 1. As the horizontal shifts are concerned, since coupling scheme channel attenuation differences of the reference indicative OV MV BPL topology take values greater than 1×10^{-11} dB, the negative horizontal shifts imply that the virtual OV MV BPL topology is characterized by lower channel attenuation than the one of the reference indicative OV MV BPL topology while the positive horizontal shifts imply the opposite result. Anyway, after the horizontal shift, the virtual coupling scheme channel attenuation difference always remains lower bounded by 1×10^{-11} dB.
- Regardless of the examined reference indicative OV MV BPL topology, higher capacities are observed in the upper left areas of the mSHM class map. Since restrictions concerning the virtual Empirical CDF and virtual coupling scheme channel attenuation differences have been already reported, the great areas of the OV MV BPL "LOS" topology class are observed in the upper left areas of the mSHM class map. As the examined reference indicative OV MV BPL topology is characterized by high capacity, there is no need for high boost of the Empirical CDF (*i.e.*, vertical shift) so that the capacity of the virtual OV MV BPL topology reaches up to the capacity maximum that is the capacity of OV MV BPL "LOS" topology class. The latter explanation justifies the area expansion of the OV MV BPL "LOS" topology class up to the lower left areas of the mSHM class maps when OV MV BPL rural and OV MV BPL suburban topology classes are illustrated in Figs. 3(c) and 3(d), respectively.
- Regardless of the examined reference indicative OV MV BPL topology, lower capacities are observed especially in the lower right areas of the mSHM class map but also, in a certain extent, in upper right areas of the mSHM class map. As the lower right areas of the mSHM class map are examined, the high imposed

coupling scheme channel attenuation differences by the high values of the horizontal shifts that are combined with the relatively low increase of Empirical CDF due to the low values of the vertical shifts normally reduce the capacities of the virtual OV MV BPL topologies. Here, there is no restriction to the imposed coupling scheme channel attenuation differences and, therefore, the capacities of the virtual OV MV BPL topologies tend to zero as the horizontal shifts significantly increase. As the upper right of the mSHM class map, which can be treated as a special case of the low capacity behavior, are investigated, the capacities of the virtual OV MV BPL topologies are observed to be decreased but remain higher than the capacities observed in the lower right areas of the mSHM class map when vertical shifts exceed 0.9. The behavior of the capacities of the virtual OV MV BPL topologies in the upper right areas of the mSHM class map is explained by the fact that, for given the maximum vertical shift (e.g., 1), as the horizontal shift increases above 0dB this implies that the virtual Empirical CDF is characterized by a step function of magnitude 1 while the step position is located at the examined horizontal step value. Due to the shape of the virtual Empirical CDF, the virtual coupling scheme channel attenuation difference is fixed and equal to the examined horizontal step value. As the examined horizontal shift increases, so does the fixed virtual coupling scheme channel attenuation difference, thus having an effect of the reduction of the capacity of the examined virtual OV MV BPL topology.

- By identifying the five capacity areas between the computed borders in each of the mSHM class maps of Figs. 3(a)-(d), it is obvious that a plethora of virtual OV MV BPL topologies can enrich the different OV MV BPL topology classes by adopting different reference indicative OV MV BPL topologies when suitable combined horizontal and vertical shift adjustments that comply with the respective mSHM class map areas and Empirical CDFs are followed.

3.4 mSHM Definition Procedure for UN MV BPL topologies

With reference to Table 3 of [4], Empirical CASD of mSHM does not achieve better capacity estimations than the ones of Wald CASD of iSHM in UN MV BPL topologies but the percentage change differences in all the examined cases remain significantly low. Anyway, the average absolute percentage change between the Empirical CASD of mSHM (*i.e.*, 0.07%) and Wald CASD of iSHM (*i.e.*, 0.01%) again remains significantly low while the main advantage of the Empirical CASD against Wald CASD remains its execution time (as reported in Sec.3.5).

In accordance with [1] and similarly to Sec.3.3, all the four indicative UN MV BPL topologies of the main subclasses of Table 2 of [1], except for the UN MV "LOS" case, are examined separately during the preparation of mSHM class maps. As the horizontal shifts, vertical shifts, horizontal shift spacings and vertical shift spacings of the mSHM class maps of UN MV BPL topologies are considered, these are assumed to receive the same values with the respective ones of the mSHM class maps of OV MV BPL topologies. Also, the capacity borders between the adjacent distribution BPL topology classes $CBo_l^{G,C}, l = 1, 2, 3, 4$, which are adopted during the preparation of the mSHM class maps, are equal to 561 Mbps, 619 Mbps, 651 Mbps and 699 Mbps,

respectively, and remain the same ones with the respective capacity borders during the preparation of the iSHM class maps already presented in Sec.3.2. The class map of UN MV BPL topologies is plotted in Fig. 4(a) with respect to the horizontal shift h_shift and vertical shift v_shift when the operation settings of Sec.2 are assumed. In the same 2D contour plot, the capacity borders between the adjacent distribution BPL topology classes and the capacity of the reference indicative UN MV BPL urban case A of Table 2 of [1] are also shown. In Figs. 4(b)-(d), same plots with Fig. 4(a) are given but for the case of the reference indicative UN MV BPL urban case B, UN MV BPL suburban case and UN MV BPL rural case of Table 2 of [1], respectively.

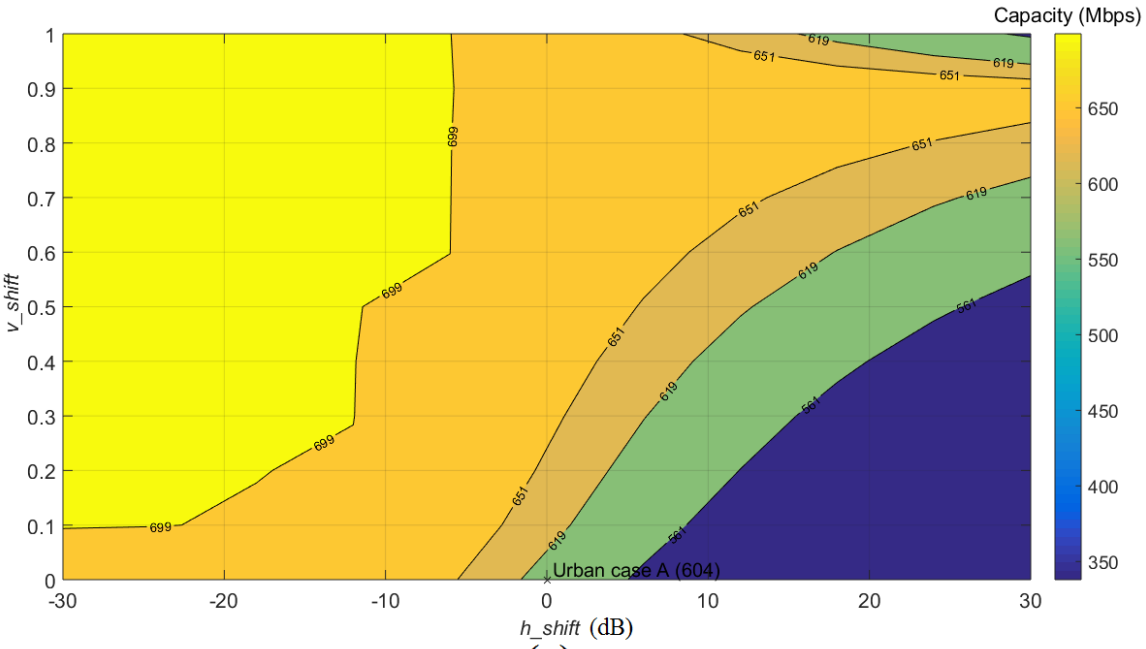
Capacity (Mbps)
v_shift
h_shift (dB)
Urban case A (604)
699
651
619
561

(a)

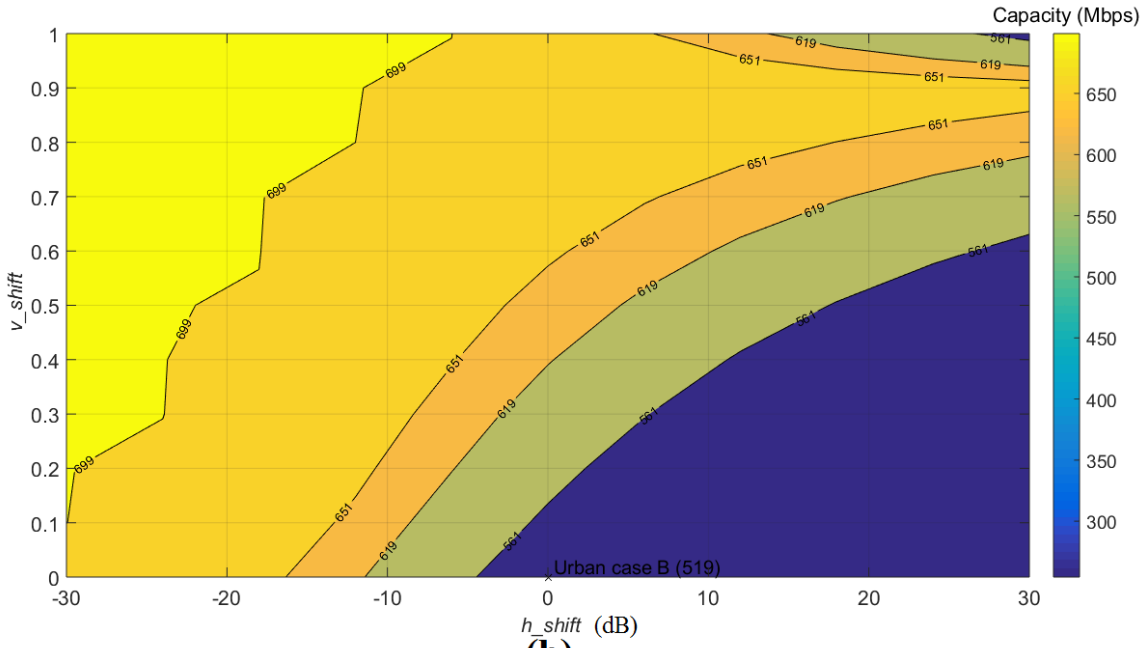
Capacity (Mbps)
v_shift
h_shift (dB)
Urban case B (519)
699
651
619
561

(b)

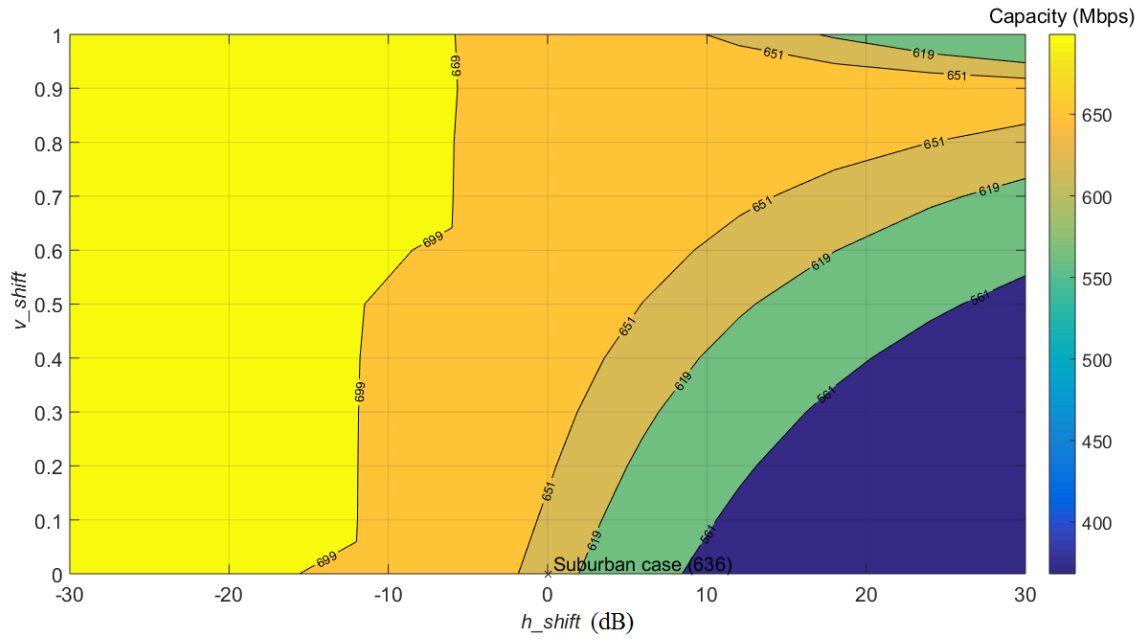

(c)

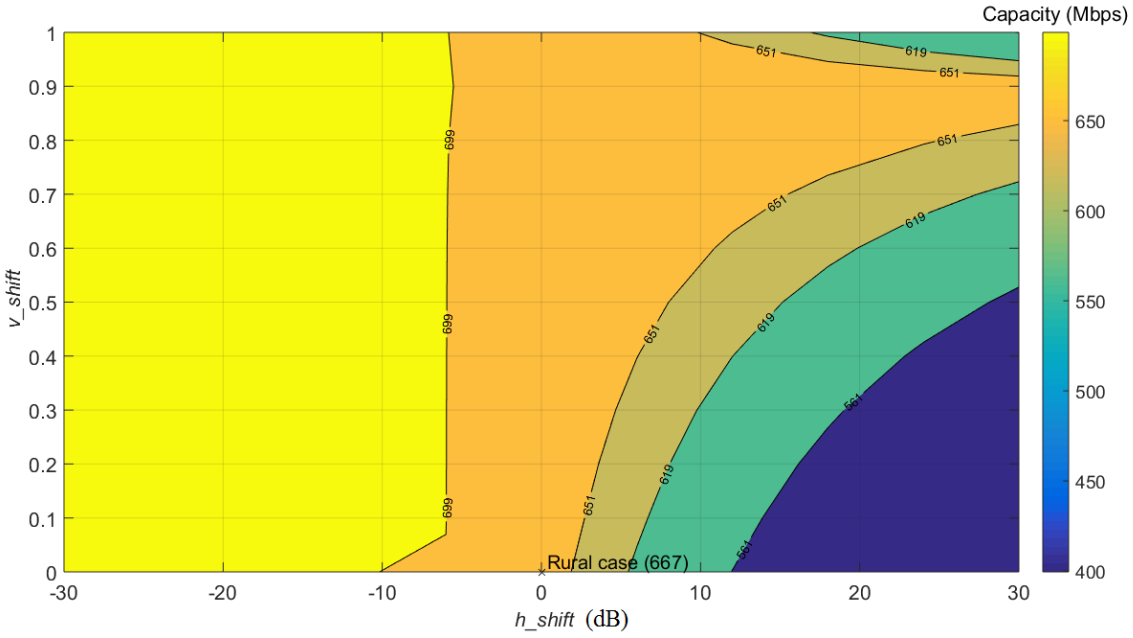

(d)

Fig. 4. mSHM class map of the UN MV BPL topologies in the 3-30MHz frequency band when StP[1] coupling scheme is deployed and FCC Part 15 is applied for different reference indicative UN MV BPL topologies. (a) UN MV BPL urban case A. (b) UN MV BPL urban case B. (c) UN MV BPL suburban case. (d) UN MV BPL rural case.

By observing Figs. 4(a)-(d), several interesting conclusions can be reported concerning the mSHM class maps, namely:

- Similarly to the mSHM class maps of OV MV BPL topologies, five capacity areas between the computed borders are clearly delineated in the mSHM class

map of UN MV BPL topologies whose planning remains the same as that of mSHM class maps of OV MV BPL topologies in Figs. 3(a)-(d).

- Similarly to mSHM class maps of the OV MV BPL topologies, the reference indicative UN MV BPL topology of each of the illustrated mSHM class maps is located at the axis center of each class map while the capacities of the virtual UN MV BPL topologies, which are defined with reference to the Empirical CDF of the reference indicative UN MV BPL topology, increase as the horizontal shift decreases (*i.e.*, coupling scheme channel attenuation differences decrease) or the vertical shift increases (*i.e.*, Empirical CDF shifts upward).
- By comparing the OV MV BPL "LOS" class areas of Figs. 3(a)-(d) against the UN MV BPL "LOS" class areas of Figs. 4(a)-(d), differences concerning the location of the right borderline of these areas, which are more clear when high values of vertical shifts are adopted, are here mentioned. By comparing Figs. 2 and 3 of [4], the coupling scheme channel attenuation differences of the UN MV BPL topologies are characterized by a fixed difference (*i.e.*, the minimum of the coupling scheme channel attenuation difference remains above a channel attenuation difference threshold) across the examined frequency range in contrast with the coupling scheme channel attenuation differences of the OV MV BPL topologies whose minima are equal to zero. This behavior of the coupling scheme channel attenuation differences of the UN MV BPL topologies is reflected on the class maps where the upper right UN MV BPL "LOS" class area borderline is located at the horizontal shift that is equal to the aforementioned channel attenuation difference threshold. As it is evident this channel attenuation difference threshold is included across the entire right UN MV BPL "LOS" class area borderline which is not so evident when the vertical shift is significantly lower than 1.
- Similarly to the mSHM class map of OV MV BPL topologies, by identifying the five capacity areas between the computed borders in each of the mSHM class maps of Figs. 4(a)-(d), it is obvious that a plethora of virtual UN MV BPL topologies can again be defined in order to enrich the different UN MV BPL topology classes. By selecting among the different reference indicative OV MV BPL topologies and applying suitable combined horizontal and vertical shift adjustments in compliance with the respective mSHM class maps, virtual UN MV BPL topologies of different Empirical CDF forms that anyway are members of the same UN MV BPL topology class can be defined.

3.5 Class Mapping and Simulation Time

With reference to Table 3 of [4], different CASDs and power grid types are characterized by different capacity estimation performances (*i.e.*, different percentage and average absolute percentage changes). Apart from the different capacity estimation performances, class mapping of Secs. 3.1-3.4 requires different simulation times that depend primarily on the applied CASD and secondarily on the power grid type given the operation settings of Sec. 2. More analytically, in Table 1, the required simulation times for the class mapping of Secs. 3.1-3.4, which have been recorded during the class map implementation, are reported.

Table 1
The Simulation Time of iSHM and mSHM Class Maps

SHM Type	Power Grid Type	CASD	Simulation Time (s)	Paper Section and Class Map Figure
iSHM	OV MV	Weibull	407	Sec. 3.1 / Fig. 1
	UN MV	Wald	22,137	Sec. 3.2 / Fig. 2
mSHM	OV MV	Empirical	817	Sec. 3.3 / Figs. 3(a)
	UN MV	Empirical	758	Sec. 3.4 / Figs. 4(a)

By combining the findings of Secs. 3.1-3.4 and the simulation time data of Table 1, several useful conclusions can be expressed regarding the trade-off between the performance and the speed of iSHM and mSHM CASDs, more specifically:

- As the Empirical CASD is the only CASD that is applied by mSHM, the simulation time that is required for the class mapping of OV MV and UN MV BPL topologies remains approximately the same (*i.e.*, from 758 s to 817 s). The small difference between the OV MV and UN MV BPL topology simulation times comes from the operation of the deterministic hybrid model. This is an evident outcome since the mSHM BPMN diagram of Fig. 2(b) of [1] and the mSHM definition procedure flowchart of Fig. 3(b) of [1] anyway remain the same regardless of the examined power grid type.
- With respect to the capacity estimation performance, different CASDs are applied by iSHM in order to create the class maps of OV MV and UN MV BPL topologies. Actually, Weibull and Wald CASDs are the suitable CASDs for the OV MV and UN MV BPL topologies, respectively, while the complexity of the respective MLE computation, as indicated in Secs. A.4 and A.3 of [2], differs. The different complexity of Weibull and Wald CASD MLE computation is reflected on the different simulation times of Table 1 for the iSHM class maps of OV MV and UN MV BPL topologies. In fact, with reference to Sec. A.3 of [2], the computation of Wald CASD CDF by twice using the Gaussian CDF $\Phi\{\cdot\}$ (see eq. A7 of [2]) skyrockets the required simulation time for the class mapping of UN MV BPL topologies (*i.e.*, approximately 6.15 hours for iSHM class map of UN MV BPL topologies against approximately 7 min for iSHM class map of OV MV BPL topologies).
- Apart from the applied CASD and the power grid type, the simulation times, which are presented in Table 1, critically depend on the number of spacings, which remains the critical parameter of the operation settings presented in Sec. 2. At this moment, the number of spacings for the horizontal and vertical axes for iSHM and mSHM is assumed to be equal to 10. This implies that $(10+1)\times(10+1)=121$ different MLE pair combinations and shift pair combinations are evaluated for the preparation of iSHM and mSHM class maps, respectively, while the required simulation times are presented in Table 1. If the number of spacings for the horizontal and vertical axes increases to 100, $(100+1)\times(100+1)=10{,}201$ different MLE pair combinations and shift pair combinations are required for the preparation of iSHM and mSHM class maps,

respectively,
while the simulation times are expected to be increased by approximately 84 times. By analyzing the simulation time data of Table 1, this becomes a prohibitive task for the iSHM class mapping of UN MV BPL topologies (*i.e.*, the simulation time is expected to be equal to approximately 21.5 days).

- By considering the capacity estimation performance and the simulation data of the different CASDs for the class mapping of UN MV BPL topologies, an interesting trade-off can be established between Empirical CASD of mSHM and the Wald CASD of iSHM. Although the capacity estimation performance of Wald CASD of iSHM presents slightly improved results with respect to the capacity estimation performance in relation with the Empirical CASD of mSHM, the simulation time of Wald CASD is six times greater than the one of Empirical CASD. Therefore, the slight improved capacity estimation performance is exchanged at significantly worse simulation times. Conversely, the same trade-off issue holds in OV MV BPL topologies between the Empirical CASD of mSHM and the Weibull CASD of iSHM.

By concluding this Section, it is evident that the definition of class maps of distribution BPL topologies can successfully enrich the existing distribution BPL topology classes with a plethora of statistically equivalent virtual distribution BPL topologies. However, the selection among different CASDs and different SHM types offers a diversity regarding the capacity estimation performance and the simulation time.

4. Conclusions

In this paper, the numerical results concerning the class mapping of OV MV and UN MV BPL topologies have been presented on the basis of iSHM and mSHM flowcharts and definition procedures, which have been analyzed in [1]. In accordance with the proposed class maps, it has been verified that distribution BPL topology classes can be further enriched with respective distribution BPL topology subclasses that further consist of a plethora of corresponding distribution BPL topologies that remain statistically equivalent with the indicative distribution BPL topology of the examined subclass. Apart from the definition of virtual distribution BPL topologies in terms of their capacity by simply selecting appropriate CASD parameters, the capacity estimation performance and the simulation time of iSHM and mSHM CASDs have been examined revealing an interesting trade-off between the aforementioned two parameters. After the class map definition, the statistical approach of SHM can be considered to be more robust since a great number of indicative distribution BPL topologies, which can act as representative topologies of respective distribution BPL topology subclasses, can be assumed.

CONFLICTS OF INTEREST

The author declares that there is no conflict of interests regarding the publication of this paper.

References

[1] A. G. Lazaropoulos, "Virtual Indicative Broadband over Power Lines Topologies for Respective Subclasses by Adjusting Channel Attenuation Statistical Distribution Parameters of Statistical Hybrid Models – Part 1: Theory," *Trends in Renewable Energy*, vol. 5, no. 3, pp 237-257, Aug. 2019. DOI: 10.17737/tre.2019.5.3.0099

[2] A. G. Lazaropoulos, "Statistical Broadband over Power Lines Channel Modeling – Part 1: The Theory of the Statistical Hybrid Model," *Progress in Electromagnetics Research C*, vol. 92, pp. 1-16, 2019. [Online]. Available: http://www.jpier.org/PIERC/pierc92/01.19012902.pdf

[3] A. G. Lazaropoulos, "Statistical Broadband over Power Lines (BPL) Channel Modeling – Part 2: The Numerical Results of the Statistical Hybrid Model," *Progress in Electromagnetics Research C*, vol. 92, pp. 17-30, 2019. [Online]. Available: http://www.jpier.org/PIERC/pierc92/02.19012903.pdf

[4] A. G. Lazaropoulos, "Enhancing the Statistical Hybrid Model Performance in Overhead and Underground Medium Voltage Broadband over Power Lines Channels by Adopting Empirical Channel Attenuation Statistical Distribution," *Trends in Renewable Energy*, vol. 5, no. 2, pp. 181-217, 2019. [Online]. Available: http://futureenergysp.com/index.php/tre/article/view/96/pdf

[5] A. G. Lazaropoulos, "Towards Modal Integration of Overhead and Underground Low-Voltage and Medium-Voltage Power Line Communication Channels in the Smart Grid Landscape: Model Expansion, Broadband Signal Transmission Characteristics, and Statistical Performance Metrics (Invited Paper)," *ISRN Signal Processing*, vol. 2012, Article ID 121628, pp. 1-17, 2012. [Online]. Available: http://www.hindawi.com/isrn/sp/2012/121628/

[6] A. G. Lazaropoulos, "Towards Broadband over Power Lines Systems Integration: Transmission Characteristics of Underground Low-Voltage Distribution Power Lines," *Progress in Electromagnetics Research B*, vol. 39, pp. 89-114, 2012. [Online]. Available: http://www.jpier.org/PIERB/pierb39/05.12012409.pdf

[7] A. G. Lazaropoulos and P. G. Cottis, "Transmission characteristics of overhead medium voltage power line communication channels," *IEEE Trans. Power Del.*, vol. 24, no. 3, pp. 1164-1173, Jul. 2009.

[8] A. G. Lazaropoulos and P. G. Cottis, "Capacity of overhead medium voltage power line communication channels," *IEEE Trans. Power Del.*, vol. 25, no. 2, pp. 723-733, Apr. 2010.

[9] A. G. Lazaropoulos and P. G. Cottis, "Broadband transmission via underground medium-voltage power lines-Part I: transmission characteristics," *IEEE Trans. Power Del.*, vol. 25, no. 4, pp. 2414-2424, Oct. 2010.

[10] A. G. Lazaropoulos and P. G. Cottis, "Broadband transmission via underground medium-voltage power lines-Part II: capacity," *IEEE Trans. Power Del.*, vol. 25, no. 4, pp. 2425-2434, Oct. 2010.

[11] A. G. Lazaropoulos, "Broadband transmission and statistical performance properties of overhead high-voltage transmission networks," *Hindawi Journal of*

Computer Networks and Commun., 2012, article ID 875632, 2012. [Online]. Available: http://www.hindawi.com/journals/jcnc/aip/875632/

[12] P. Amirshahi and M. Kavehrad, "High-frequency characteristics of overhead multiconductor power lines for broadband communications," *IEEE J. Sel. Areas Commun.*, vol. 24, no. 7, pp. 1292-1303, Jul. 2006.

[13] T. Sartenaer, "Multiuser communications over frequency selective wired channels and applications to the powerline access network" *Ph.D. dissertation*, Univ. Catholique Louvain, Louvain-la-Neuve, Belgium, Sep. 2004.

[14] T. Calliacoudas and F. Issa, ""Multiconductor transmission lines and cables solver," An efficient simulation tool for plc channel networks development," presented at the *IEEE Int. Conf. Power Line Communications and Its Applications*, Athens, Greece, Mar. 2002.

[15] T. Sartenaer and P. Delogne, "Deterministic modelling of the (Shielded) outdoor powerline channel based on the multiconductor transmission line equations," *IEEE J. Sel. Areas Commun.*, vol. 24, no. 7, pp. 1277-1291, Jul. 2006.

[16] A. G. Lazaropoulos, "Virtual Indicative Broadband over Power Lines Topologies for Respective Subclasses by Adjusting Channel Attenuation Statistical Distribution Parameters of Statistical Hybrid Models – Part 3: The Case of Overhead Transmission Power Grids," *Trends in Renewable Energy*, vol. 5, no. 3, pp 282-306, Aug. 2019. DOI: 10.17737/tre.2019.5.3.00101

[17] S. Liu and L. J. Greenstein, "Emission characteristics and interference constraint of overhead medium-voltage broadband power line (BPL) systems," in *Proc. IEEE Global Telecommunications Conf.*, New Orleans, LA, USA, Nov./Dec. 2008, pp. 1-5.

[18] A. G. Lazaropoulos, "Underground Distribution BPL Connections with (N + 1)-hop Repeater Systems: A Novel Capacity Mitigation Technique," *Elsevier Computers and Electrical Engineering*, vol. 40, pp. 1813-1826, 2014.

[19] A. G. Lazaropoulos, "Review and Progress towards the Capacity Boost of Overhead and Underground Medium-Voltage and Low-Voltage Broadband over Power Lines Networks: Cooperative Communications through Two- and Three-Hop Repeater Systems," *ISRN Electronics*, vol. 2013, Article ID 472190, pp. 1-19, 2013. [Online]. Available: http://www.hindawi.com/isrn/electronics/aip/472190/

[20] A. G. Lazaropoulos, "Broadband over Power Lines (BPL) Systems Convergence: Multiple-Input Multiple-Output (MIMO) Communications Analysis of Overhead and Underground Low-Voltage and Medium-Voltage BPL Networks (Invited Paper)," *ISRN Power Engineering*, vol. 2013, Article ID 517940, pp. 1-30, 2013. [Online]. Available: http://www.hindawi.com/isrn/power.engineering/2013/517940/

[21] A. G. Lazaropoulos, "Deployment Concepts for Overhead High Voltage Broadband over Power Lines Connections with Two-Hop Repeater System: Capacity Countermeasures against Aggravated Topologies and High Noise Environments," *Progress in Electromagnetics Research B*, vol. 44, pp. 283-307, 2012. [Online]. Available: http://www.jpier.org/PIERB/pierb44/13.12081104.pdf

[22] N. Suljanović, A. Mujčić, M. Zajc, and J. F. Tasič, "Approximate computation of high-frequency characteristics for power line with horizontal disposition and

middle-phase to ground coupling," *Elsevier Electr. Power Syst. Res.*, vol. 69, pp. 17-24, Jan. 2004.

[23] OPERA1, D5: Pathloss as a function of frequency, distance and network topology for various LV and MV European powerline networks. IST Integrated Project No 507667, Apr. 2005.

[24] N. Suljanović, A. Mujčić, M. Zajc, and J. F. Tasič, "High-frequency characteristics of high-voltage power line," in *Proc. IEEE Int. Conf. on Computer as a Tool*, Ljubljana, Slovenia, Sep. 2003, pp. 310-314.

[25] N. Suljanović, A. Mujčić, M. Zajc, and J. F. Tasič, "Power-line high-frequency characteristics: analytical formulation," in *Proc. Joint 1st Workshop on Mobile Future & Symposium on Trends in Communications*, Bratislava, Slovakia, Oct. 2003, pp. 106-109.

[26] W. Villiers, J. H. Cloete, and R. Herman, "The feasibility of ampacity control on HV transmission lines using the PLC system," in *Proc. IEEE Conf. Africon*, George, South Africa, Oct. 2002, vol. 2, pp. 865-870.

[27] P. Amirshahi, "Broadband access and home networking through powerline networks" Ph.D. dissertation, Pennsylvania State Univ., University Park, PA, May 2006.

[28] OPERA1, D44: Report presenting the architecture of plc system, the electricity network topologies, the operating modes and the equipment over which PLC access system will be installed, IST Integr. Project No 507667, Dec. 2005.

[29] J. Anatory, N. Theethayi, R. Thottappillil, M. M. Kissaka, and N. H. Mvungi, "The influence of load impedance, line length, and branches on underground cable Power-Line Communications (PLC) systems," *IEEE Trans. Power Del.*, vol. 23, no. 1, pp. 180-187, Jan. 2008.

[30] J. Anatory, N. Theethayi, and R. Thottappillil, "Power-line communication channel model for interconnected networks-Part II: Multiconductor system," *IEEE Trans. Power Del.*, vol. 24, no. 1, pp. 124-128, Jan. 2009.

[31] J. Anatory, N. Theethayi, R. Thottappillil, M. M. Kissaka, and N. H. Mvungi, "The effects of load impedance, line length, and branches in typical low-voltage channels of the BPLC systems of developing countries: transmission-line analyses," *IEEE Trans. Power Del.*, vol. 24, no. 2, pp. 621-629, Apr. 2009.

[32] T. Banwell and S. Galli, "A novel approach to accurate modeling of the indoor power line channel—Part I: Circuit analysis and companion model," *IEEE Trans. Power Del.*, vol. 20, no. 2, pp. 655-663, Apr. 2005.

[33] W. Villiers, J. H. Cloete, L. M. Wedepohl, and A. Burger, "Real-time sag monitoring system for high-voltage overhead transmission lines based on power-line carrier signal behavior," *IEEE Trans. Power Del.*, vol. 23, no. 1, pp. 389-395, Jan. 2008.

[34] A. G. Lazaropoulos, "Smart Energy and Spectral Efficiency (SE) of Distribution Broadband over Power Lines (BPL) Networks – Part 1: The Impact of Measurement Differences on SE Metrics," *Trends in Renewable Energy*, vol. 4, no. 2, pp. 125-184, Aug. 2018. [Online]. Available: http://futureenergysp.com/index.php/tre/article/view/76/pdf

[35] A. G. Lazaropoulos, "Broadband Performance Metrics and Regression Approximations of the New Coupling Schemes for Distribution Broadband over

Power Lines (BPL) Networks," *Trends in Renewable Energy*, vol. 4, no. 1, pp. 43-73, Jan. 2018. [Online]. Available: http://futureenergysp.com/index.php/tre/article/view/59/pdf

[36] A. G. Lazaropoulos, "New Coupling Schemes for Distribution Broadband over Power Lines (BPL) Networks," *Progress in Electromagnetics Research B*, vol. 71, pp. 39-54, 2016. [Online]. Available: http://www.jpier.org/PIERB/pierb71/02.16081503.pdf

[37] A. G. Lazaropoulos, "A Panacea to Inherent BPL Technology Deficiencies by Deploying Broadband over Power Lines (BPL) Connections with Multi-Hop Repeater Systems," *Bentham Recent Advances in Electrical & Electronic Engineering*, vol. 10, no. 1, pp. 30-46, 2017.

[38] A. G. Lazaropoulos, "The Impact of Noise Models on Capacity Performance of Distribution Broadband over Power Lines Networks," *Hindawi Computer Networks and Communications*, vol. 2016, Article ID 5680850, 14 pages, 2016. doi:10.1155/2016/5680850. [Online]. Available: http://www.hindawi.com/journals/jcnc/2016/5680850/

[39] A. G. Lazaropoulos, "Capacity Performance of Overhead Transmission Multiple-Input Multiple-Output Broadband over Power Lines Networks: The Insidious Effect of Noise and the Role of Noise Models (Invited Paper)," *Trends in Renewable Energy*, vol. 2, no. 2, pp. 61-82, Jun. 2016. [Online]. Available: http://futureenergysp.com/index.php/tre/article/view/23

[40] A. G. Lazaropoulos, "Smart Energy and Spectral Efficiency (SE) of Distribution Broadband over Power Lines (BPL) Networks – Part 2: L1PMA, L2WPMA and L2CXCV for SE against Measurement Differences in Overhead Medium-Voltage BPL Networks," *Trends in Renewable Energy*, vol. 4, no. 2, pp. 185-212, Aug. 2018. [Online]. Available: http://futureenergysp.com/index.php/tre/article/view/77/pdf

[41] A. G. Lazaropoulos, "Factors Influencing Broadband Transmission Characteristics of Underground Low-Voltage Distribution Networks," *IET Commun.*, vol. 6, no. 17, pp. 2886-2893, Nov. 2012.

Trends in Renewable Energy
OPEN ACCESS ISSN: 2376-2144
Peer-Reviewed Article futureenergysp.com/index.php/tre

Virtual Indicative Broadband over Power Lines Topologies for Respective Subclasses by Adjusting Channel Attenuation Statistical Distribution Parameters of Statistical Hybrid Models (Class Maps) – Part 3: The Case of Overhead Transmission Power Grids

Athanasios G. Lazaropoulos*

School of Electrical and Computer Engineering / National Technical University of Athens / 9 Iroon Polytechniou Street / Zografou, GR 15780

Received June 21, 2019; Accepted August 12, 2019; Published August 16, 2019

In [1], [2], the theoretical framework and the numerical results concerning the class mapping of overhead and underground medium voltage broadband over power lines (OV and UN MV BPL) topologies have been presented on the basis of the recently proposed initial statistical hybrid model (iSHM), modified statistical hybrid model (mSHM) and class map definition procedure. In this paper, all the recent findings regarding the statistical channel modeling and class mapping are first applied to transmission BPL networks; say, OV high voltage (HV) BPL topologies. The numerical results of OV HV BPL networks are compared against the respective ones of OV and UN distribution networks revealing significant similarities and differences. Finally, the impact of considering minimum or maximum capacity value instead of the average one during the definition procedure is investigated as well as the behavior of the total simulation time of class mapping.

Keywords: Smart Grid; Broadband over Power Lines (BPL) networks; Power Line Communications (PLC); Distribution Power Grids; Capacity; Statistics; Modeling

1. Introduction

As the BPL channel modeling is concerned for the distribution and transmission Broadband over Power Lines (BPL) networks, BPL channel models have typically followed either a bottom-up approach or a top-down approach or appropriate synergies of the aforementioned approaches until now [3]-[25]. Recently, statistical channel models have been proposed for BPL networks [26]-[33]. Among them, statistical hybrid models (SHMs) are based on the formality and validity of the deterministic hybrid model, which interconnects the bottom-up and top-down approach and has extensively been validated in transmission and distribution BPL networks [5]-[10], [13], [15], [16], [20], [34], while SHMs results are considered as the filtered deterministic hybrid model results through a set of proper channel attenuation statistical distributions (CASDs). Initial SHM (iSHM), which has been proposed in [28], [29], applies well-known CASDs of the communications research fields, such as Gaussian,

*Corresponding author: AGLazaropoulos@gmail.com

Tr Ren Energy, 2019, Vol.5, No.3, 282-306. doi: 10.17737/tre.2019.5.3.00101

Lognormal, Wald, Weibull and Gumbel CASDs [35], while modified SHM (mSHM), which has been proposed in [30], exploits the Empirical CASD. As already been mentioned in [28]-[30], CASD parameters, which are CASD maximum likelihood estimators (MLEs) and CASD cumulative density functions (CDFs) for iSHM and mSHM, respectively, can characterize each real distribution BPL topology while virtual distribution BPL topologies can be defined by appropriately adjusting the aforementioned CASD parameters [1], [2]. The significance of the combined operation of SHMs with the definition procedure of the virtual indicative distribution BPL topologies, which has been presented in [28], [29], mitigates the underrepresentation of the distribution BPL topology classes during the BPL statistical channel modelling and the graphical representation of the distribution BPL topology classes and subclasses in terms of their average capacity through the proposed class maps. In this paper, all the recent findings concerning iSHM, mSHM, CASDs, CASD parameters, definition procedure and class maps are first applied to OV HV BPL topologies in this paper. The results for the transmission BPL networks are compared against the ones of distribution BPL networks. Interesting similarities and differences can be unveiled between the distribution and transmission BPL networks since the different BPL signal transmission characteristics can influence in different ways the behavior of CASDs and, thus, of iSHM and mSHM. Also, an interesting contribution to the definition procedure is the impact examination of applying maximum and minimum capacity value of the distribution BPL topology subclasses instead of the average one. Finally, the theoretical approach of the total simulation time of iSHM and mSHM class mapping is here graphically investigated in terms of the time complexity when different number of spacings, that is a critical factor of class mapping for the accuracy of the x- and y-axis, are applied during the iSHM and mSHM class mapping.

The rest of this paper is organized as follows: In Section II, the OV HV MTL configuration with the set of indicative OV HV BPL topologies of the main topology subclasses are presented. In Section III, the numerical results concerning the application of iSHM and mSHM are demonstrated as well as the respective CASD parameter analysis, definition procedure and class maps. Also, a comparative analysis is given between the distribution and transmission BPL topologies. Section IV concludes this paper.

2. OV HV MTL Configurations and Respective BPL Topologies

Similarly to [1], a small briefing concerning the adopted OV HV MTL configuration is given while the topological characteristics of the indicative OV HV BPL topologies of the main subclasses are reported.

2.1 OV HV MTL Configurations

In Fig. 1, the typical OV HV MTL configuration that is used in the present work is illustrated. The MTL configuration of this paper is a typical OV 400kV double-circuit configuration with phase lines of radius $r_{\mathrm{p}}^{\mathrm{OVHV}}$ that hang at typical heights $h_{\mathrm{p}}^{\mathrm{OVHV}}$ above ground –*i.e.*, conductors 1, 2, 3, 4, 5, and 6–. These six phase conductors are divided into three bundles. Each bundle is spaced by $\Delta_{\mathrm{p1}}^{\mathrm{OVHV}}$ while the phase conductors of each bundle

are connected by non-conducting spacers and are separated by Δ_{p2}^{OVHV}. Apart from the phase conductors, two parallel neutral conductors hang at heights h_n^{OVHV} –i.e, conductors 7 and 8–. Neutral conductors are of radius r_n^{OVHV} and are spaced each other by Δ_n^{OVHV}.

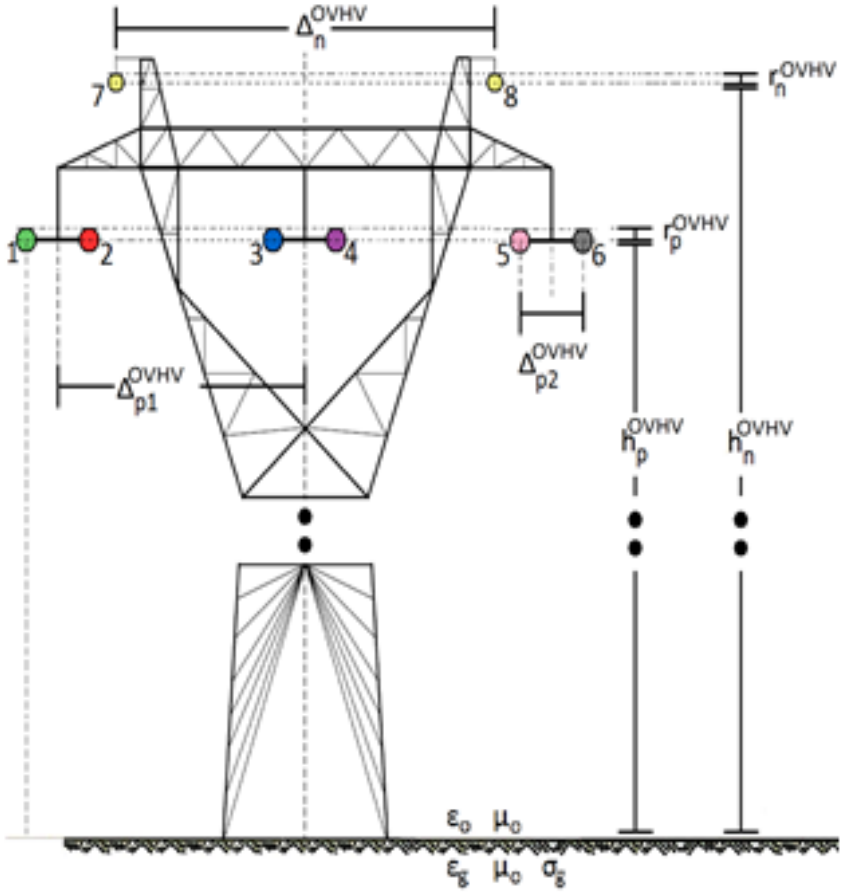

Fig. 1. Typical OV HV MTL configuration [9].

All phase and neutral conductors are Aluminium-conductor steel-reinforced (ACSR) [4], [9], [36]-[39]. The exact dimensions concerning the radii, spacings and heights are given in [9].

Similarly to distribution BPL networks, the ground is considered imperfect and as the reference conductor. A realistic scenario, which is adopted in this paper, holds that the conductivity of the ground is assumed σ_g=5mS/m while its relative permittivity ε_{rg}=13 [4]-[6], [9], [13], [40]-[44].

2.2 OV HV BPL Topologies and Respective Topology Subclasses and Classes

Transmission BPL topologies adopt the network architecture of distribution BPL topologies. Actually, transmission BPL networks are divided into cascaded BPL topologies of typical lengths of 25km. Similarly to distribution BPL topologies, each transmission BPL topology is bounded by its transmitting and receiving end while

different number of branches $k,\ k=1,\cdots,N$, distribution cable lengths $L_k,\ k=1,\cdots,N+1$ and branch lengths $L_{bk},\ k=1,\cdots,N$ are encountered between the transmitting and receiving end [5]-[10], [34].

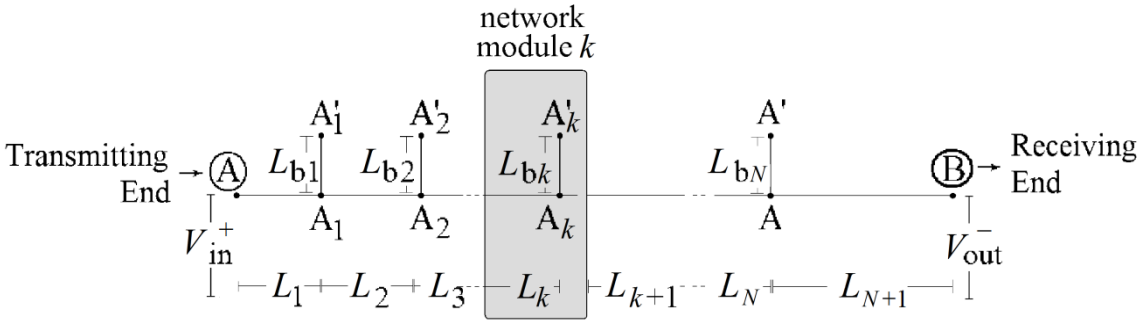

Fig. 2. Typical OV HV BPL topology with N branches [1].

As the BPL signal transmission across the transmission BPL topologies is concerned, the following five indicative OV HV BPL topologies of the main subclasses of the respective transmission BPL topology classes are examined, namely [4], [9], [45]: (i) A typical OV HV BPL urban topology (simply denoted as urban case A); (ii) An aggravated OV HV BPL urban topology (simply denoted as urban case B); (iii) A typical suburban OV HV BPL topology (simply denoted as suburban case); (iv) A typical OV HV BPL rural topology (simply denoted as rural case); and (v) The "LOS" transmission along the same end-to-end distance $L=L_1+\ldots+L_{K+1}$=25km. This topology corresponds to Line of Sight transmission of wireless channels (simply denoted as "LOS" case). The topological characteristics of the aforementioned five indicative OV HV BPL topologies of the main subclasses are reported in Table 1.

Table 1. Indicative OV HV BPL Topologies of the Main Subclasses and Respective BPL Topology Classes

OV HV BPL Topology Class	**BPL Topology Number (and BPL Topology Subclass Number) (l)**	**BPL Topology Name (and BPL Topology Subclass Name)**	**Number of Branches**	**Length of Distribution Lines**	**Length of Branching Lines**
Typical OV HV BPL urban topology class	OV HV 1	Urban case A (main subclass)	3	L_1=1,150m, L_2=12,125m, L_3=8,425m, L_4=3,300m	L_{b1}=27,600m, L_{b2}=17,200m, L_{b3}=33,100m
Aggravated OV HV BPL urban topology class	OV HV 2	Urban case B (main subclass)	4	L_1=125m, L_2=3,950m, L_3=3,275m, L_4=13,875m, L_5=3,775m	L_{b1}=19,000m, L_{b2}=22,700m, L_{b3}=17,100m, L_{b4}=18,000m
OV HV BPL suburban topology class	OV HV 3	Suburban case (main subclass)	2	L_1=9,025m, L_2=12,750m, L_3=3,225m	L_{b1}=46,800m, L_{b2}=13,400m
OV HV BPL rural topology class	OV HV 4	Rural case (main subclass)	1	L_1=3,750m, L_2=21,250m	L_{b1}=21,100m
OV HV BPL "LOS" topology class	OV HV 5	"LOS" case (main subclass)	0	L_1=25,000m	-

3. Numerical Results and Discussion

In this Section, numerical results concerning the statistical channel attenuation modeling of transmission BPL networks are first presented. First, CASD parameters of iSHM and mSHM are computed for the indicative OV HV BPL topologies of the main subclasses of Table 1. Second, the maximum, average and minimum of OV HV BPL topology main subclass capacities for the CASDs of iSHM and mSHM are presented while the percentage change and the average absolute percentage change for the indicative OV HV BPL topologies of the main subclasses of Table 1 are reported. Third, since CASD parameters of iSHM and mSHM are well defined, the definition procedure of iSHM and mSHM is presented by focusing on the class mapping through two scenarios, namely: (i) iSHM definition procedure for OV HV BPL topologies; and (ii) mSHM definition procedure for OV HV BPL topologies. Fourth, observations regarding the simulation time of the aforementioned two scenarios are given. Note that the operation settings that are required for the fine operation of the statistical modeling in OV HV BPL networks are the same with the ones of OV MV BPL topologies that are reported in Secs.2.1-2.4 of [2] for the deterministic hybrid model, iSHM, mSHM and definition procedure, respectively.

3.1 CASD MLEs of iSHM and mSHM of OV HV BPL Classes for the Default Operation Settings

The Business Process Modeling Notation (BPMN) diagrams of iSHM and mSHM, that describe the operation flowcharts of iSHM and mSHM, are given in Figs. 1(a) and 1(b) of [30], respectively. By comparing these flowcharts, the main difference between iSHM and mSHM is concentrated on the definition of the respective CASD parameters. As already been presented, the CASD parameters of iSHM are the CASD MLEs of Table 2 while the CASD parameter of mSHM is the Empirical CDF for given indicative BPL topology.

As the default operation settings are assumed, in Table 2, MLEs of the Gaussian, Lognormal, Wald, Weibull and Gumbel CASDs of iSHM are reported for the indicative OV HV BPL topologies of main subclasses of Table 1. With reference to Table 2, in Fig. 3(a), CDFs of the five channel attenuation statistical distributions (say, Gaussian, Lognormal, Wald, Weibull and Gumbel distributions) of the iSHM and of the Empirical CASD of the mSHM are plotted versus the coupling scheme channel attenuation difference for the case of the OV HV BPL urban case A. In Figs. 3(b)-(d), same plots with Fig. 3(a) are given bur for the case of the OV HV BPL urban case B, suburban case and rural case, respectively.

Table 2
iSHM CASD MLEs of Indicative OV HV BPL Topologies for the Default Operation Settings

Topology Name	BPL Topology Class Description	iSHM									
		Gaussian MLEs		Lognormal MLEs		Wald MLEs		Weibull MLEs		Gumbel MLEs	
		$\hat{\mu}_{MLE}^{Gaussian}$	$\hat{\sigma}_{MLE}^{Gaussian}$	$\hat{\mu}_{MLE}^{Lognormal}$	$\hat{\sigma}_{MLE}^{Lognormal}$	$\hat{\mu}_{MLE}^{Wald}$	$\hat{\lambda}_{MLE}^{Wald}$	$\hat{\alpha}_{MLE}^{Weibull}$	$\hat{\beta}_{MLE}^{Weibull}$	$\hat{a}_{MLE}^{Gumbel}$	$\hat{\epsilon}_{MLE}^{Gumbel}$
Urban case A	Typical OV HV BPL urban topology class	10.52	1.82	2.24	1.69	10.52	0	11.04	4.49	11.44	2.09
Urban case B	Aggravated OV HV BPL urban topology class	14.27	2.88	2.63	0.35	14.27	0.026×10^{3}	15.38	4.48	15.81	4.28
Suburban case	OV HV BPL suburban topology class	6.96	1.68	1.91	0.24	6.96	0.11×10^{3}	7.62	4.37	7.83	1.81
Rural case	OV HV BPL rural topology class	3.56	1.16	1.13	1.63	3.56	0	3.88	2.60	4.25	2.19
"LOS" case	OV HV BPL "LOS" transmission class	1×10^{-11}	0	-25.33	0	0	2.62×10^{3}	0	∞	0	0

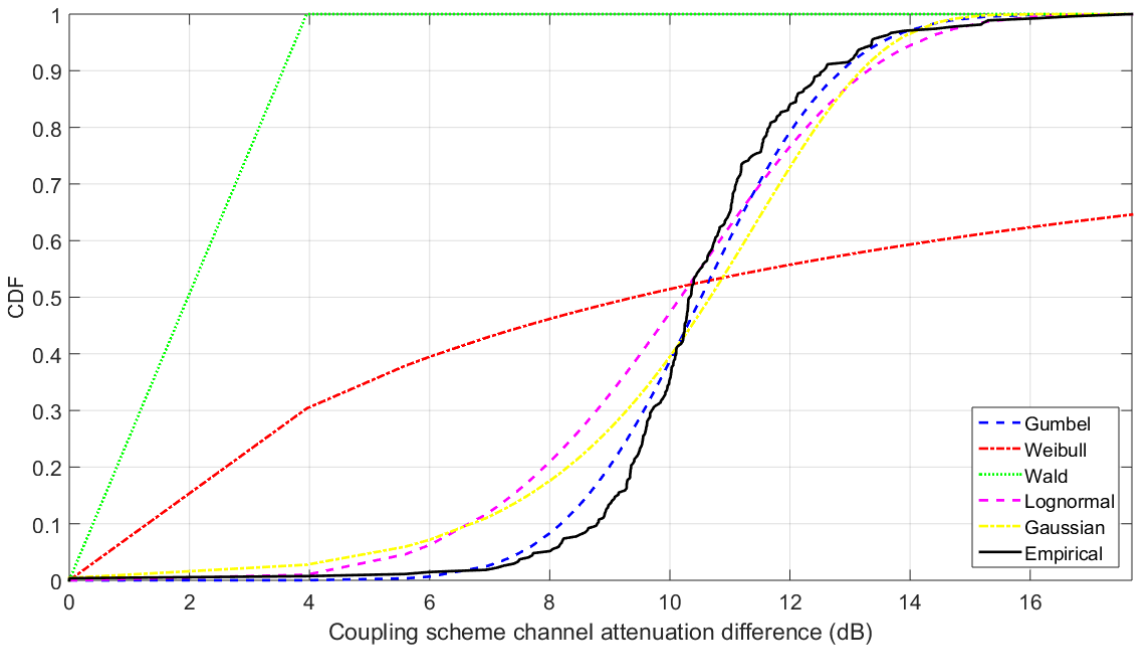
CDF
Coupling scheme channel attenuation difference (dB)
Gumbel
Weibull
Wald
Lognormal
Gaussian
Empirical

(a)

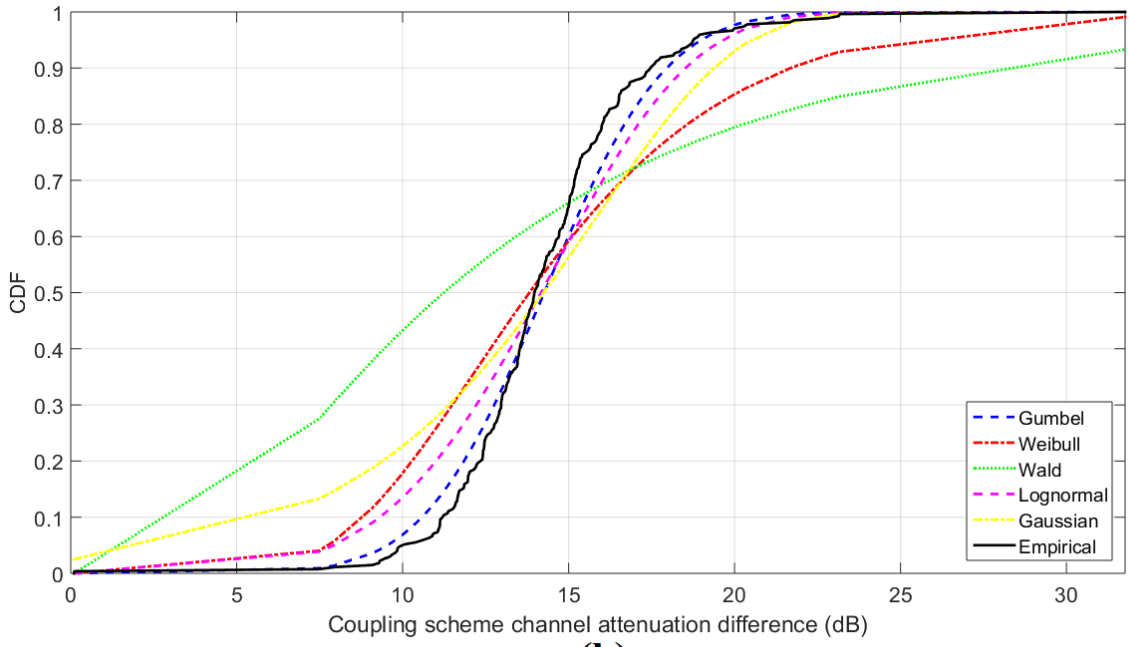
CDF
Coupling scheme channel attenuation difference (dB)
Gumbel
Weibull
Wald
Lognormal
Gaussian
Empirical

(b)

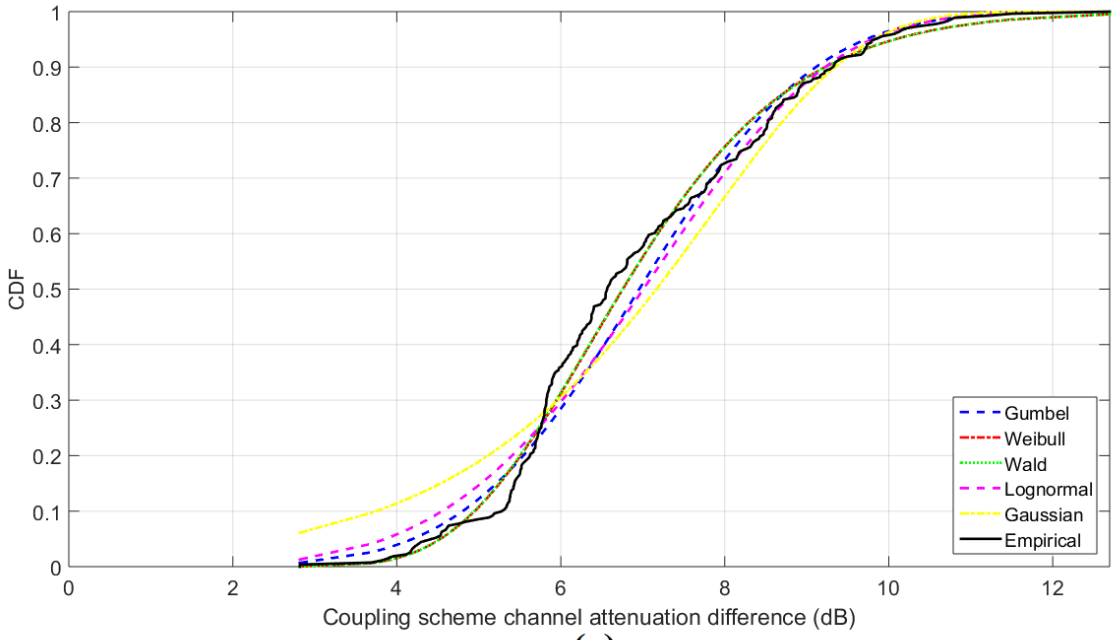

(c)

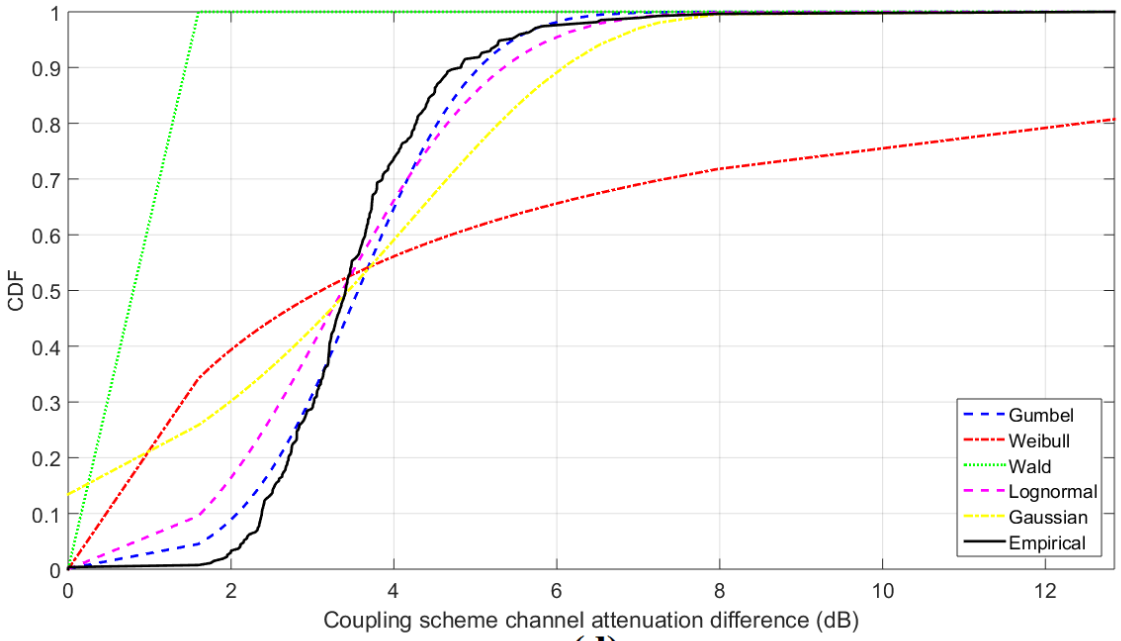

(d)

Fig. 3. CDFs of the indicative OV HV BPL topologies of Table 1 versus coupling scheme channel attenuation difference in the 3-30MHz frequency band when WtG[1] coupling scheme is deployed for CASDs of iSHM and mSHM. (a) Urban case A. (b) Urban case B. (c) Suburban case. (d) Rural case.

By comparing Table 2 with Table 1 of [29] and by observing Figs. 3(a)-(d), several comparative observations concerning CASD MLEs of iSHM and the CDF behavior of the CASDs of iSHM and mSHM can be presented, namely:

- Similarly to distribution BPL networks, as the complexity of the OV HV BPL topologies increase so do $\hat{\mu}_{\mathbf{MLE}}^{\mathbf{Gaussian}}$, $\hat{\mu}_{\mathbf{MLE}}^{\mathbf{Lognormal}}$, $\hat{\mu}_{\mathbf{MLE}}^{\mathbf{Wald}}$, $\hat{a}_{\mathbf{MLE}}^{\mathbf{Weibull}}$ and $\hat{a}_{\mathbf{MLE}}^{\mathbf{Gumbel}}$. Conversely to distribution BPL topologies, $\hat{\sigma}_{\mathbf{MLE}}^{\mathbf{Gaussian}}$, $\hat{\sigma}_{\mathbf{MLE}}^{\mathbf{Lognormal}}$, $\hat{\beta}_{\mathbf{MLE}}^{\mathbf{Weibull}}$ and $\hat{\epsilon}_{\mathbf{MLE}}^{\mathbf{Gumbel}}$ of OV HV BPL topologies receive significantly lower values than the respective ones of OV MV BPL topologies thus indicating that the variance of coupling scheme channel attenuation differences of OV HV BPL topologies remain lower than the respective ones of OV MV BPL topologies.
- $\hat{\mu}_{\mathbf{MLE}}^{\mathbf{Gaussian}}$, $\hat{\mu}_{\mathbf{MLE}}^{\mathbf{Lognormal}}$, $\hat{\mu}_{\mathbf{MLE}}^{\mathbf{Wald}}$, $\hat{a}_{\mathbf{MLE}}^{\mathbf{Weibull}}$ and $\hat{a}_{\mathbf{MLE}}^{\mathbf{Gumbel}}$ of OV HV BPL topologies receive values that are comparable to the respective ones of OV MV BPL topologies. This event indicates that the capacities of the main subclasses of OV HV BPL networks are expected to have: (i) comparable values to the capacities of the main subclasses of OV MV BPL networks; and (ii) comparable iSHM class maps to ones of OV MV BPL networks. Anyway, the capacities of the main subclasses determine the ones of the respective BPL topology classes.
- In contrast with Figs. 3(a), 3(b) and 3(d), CASD CDFs of Fig. 3(b) start to increase from a value different than zero. Actually, coupling scheme channel attenuation differences of OV HV BPL urban case A, urban case B and rural case present rare deep spectral notches that reach down to zero and, thus, their CASD CDFs start from zero. Anyway, this type of spectral notches is not present in OV HV BPL suburban case and for that reason its CASD CDFs start from approximately 3dB coupling scheme channel attenuation difference. Note that the coupling scheme channel attenuation differences of OV HV BPL topologies are restricted to range above zero since OV HV "LOS" case is characterized by the minimum coupling scheme channel attenuation due to the lack of branches across the transmission path.
- When the CASD CDF starts to increase at zero coupling scheme channel attenuation difference, certain CASD CDFs fail to follow the Empirical CASD CDF. In the cases of Figs. 3(a), 3(b) and 3(d), Wald and Weibull CASD CDFs present significant differences from the Empirical CDF since Wald CASD CDF expects to early handle the majority of data while Weibull CASD CDF expects to later handle the majority of data with respect to the aforementioned figures. Due to the previous observation, Wald CASD CDF early reaches up to 1 but Weibull CASD CDF later reaches up to 1. It is expected that these CDF deviations will also entail capacity deviations in OV HV BPL topologies and subclasses. In Fig. 3(c), CASD CDFs present similar behavior as the lack of zero coupling scheme channel attenuation difference forces CASD CDFs to almost coincide.
- By comparing Figs. 3(a)-(d) with respective Figs. 4(a)-(d) of [30], there are no coupling scheme channel attenuation difference horizontal steps in Empirical CDFs during the study of OV HV BPL topologies. In contrast with OV MV BPL topologies, there is no pattern regarding the depth, the extent and the location of spectral notches of OV HV BPL topologies and this has as a result a variety of values regarding the coupling scheme channel attenuation differences that further implies smooth Empirical CDFs with no horizontal steps.

In accordance with [2], [29], [30], it has been proven that the capacity performance success does not solely depend on the realism of random coupling scheme channel attenuation differences of the distribution BPL topology members, which are produced by the random number generator module of Phase D of iSHM and mSHM –see Figs. (2) and 2(b) of [1]–. In the following subsections, the capacity estimation performance, which is assessed by applying the metrics of capacity, capacity percentage change and average absolute capacity percentage change, is going to be investigated for the different CASDs of iSHM and mSHM.

3.2 CASD Capacities and Capacity Estimation Performance Metrics of OV HV BPL Main Subclasses for the Default Operation Settings

As the default operation settings are assumed, CASD parameters of iSHM and mSHM are reported in Table 2 and in Figs. 3(a)-(d), respectively. With respect to Table 1 and 2, each OV HV BPL topology main subclass is enriched with 100 topology members per each CASD through the random number generator of Phase D as described in [28]. Similarly to [29], [30], each OV HV BPL topology subclass can be described by the maximum, average and minimum capacity of its topology members while the corresponding capacity estimation performance metrics, say, capacity percentage change and average absolute capacity percentage change, can be computed. In accordance with [2], [29], although the graphical analysis can be very descriptive regarding the capacity estimation performance of CASDs of iSHM and mSHM, the capacity estimation performance of CASDs can also be examined by simply applying capacity estimation performance metrics of percentage change and average absolute percentage change. Therefore, the percentage change and the average absolute percentage change of each CASD of iSHM and mSHM are given in Table 3 per each indicative OV HV BPL topology main subclasses. Also, the capacity of the indicative OV HV BPL topologies of main subclasses of Table 1 is also reported in the first column of the Table.

Table 3
Percentage Change between the Average Capacity of the OV HV BPL Topology Class and the Capacity of the Indicative Topology of the Respective Class for the Five Examined CASDs of iSHM and the Empirical CASD of mSHM when the Default Operation Settings are assumed (say, WtG^1/StP^1 coupling scheme and FCC Part 15)
(grey background: best results, black background: unsuccessful capacity estimation)

Indicative OV HV BPL Topology Name (OV HV Capacity in Mbps)	**BPL Topology Class Description**	**Percentage Change (%)**					
		iSHM					**mSHM**
		Gaussian	**Lognormal**	**Wald**	**Weibull**	**Gumbel**	**Empirical**
Urban case A (187)	Typical BPL urban class	-0.0088	-15.44	50.57	2.13	1.38	0.15
Urban case B (153)	Aggravated BPL urban	0.0031	-1.73	5.52	1.46	5.01	0.38
Suburban case (218)	BPL suburban class	0.0025	-0.015	-0.0056	0.067	0.64	0.074

Rural case (249)	BPL rural class	-0.0045	-13.41	12.86	0.42	0.98	0.078
Average Absolute Percentage Change (%)		**0.012**	**7.65**	**17.24**	**1.02**	**2.00**	**0.17**

By comparing Table 3 with Table 3 of [29] and Table 3 of [30], significant similarities and differences that can be also explained by the study of Figs. 1(a)-(d) of [29] and Figs. 6(a)-(d) of [30] can be pointed out for the behavior of CASD capacity performance in OV HV BPL networks, namely:

- CASD capacity estimation performance for OV HV BPL subclasses presents significant similarities with the one of OV MV BPL topologies but also several differences. Although the typical transmission path of OV HV BPL topologies is typically equal to 25km and is significantly greater than the 1km typical transmission path of OV MV BPL topologies, the capacities of the indicative OV HV BPL topologies are slightly smaller than the respective capacities of the indicative OV MV BPL topologies. Actually, OV HV BPL topologies are characterized by a stronger "LOS" attenuation mechanism than the one of OV MV BPL topologies while the multipath aggravation in OV HV BPL topologies remains approximately the same with the one of OV MV BPL topologies [10].
- As already been mentioned in [29] for the distribution BPL subclasses, from the graphical perspective, a successful CASD capacity estimation performance should satisfy the following criteria: (i) capacity range of each transmission BPL topology subclass comprises the capacity of its respective indicative transmission BPL topology; and (ii) the average capacity value of the examined transmission BPL topology subclass remains very close to the respective one of the indicative transmission BPL topology. Without significant differences, the average capacity of each OV HV BPL topology subclass can be assumed to be equal to the capacity of its representative OV HV BPL topology. From the capacity estimation metric perspective, the lower the percentage change and average absolute percentage change in absolute values remain the better the capacity estimation performance is.
- Similarly to OV MV BPL topology subclasses, Weibull and Empirical CASDs succeed in satisfying either the aforementioned criteria for a successful capacity graphical estimation or the 3% threshold of percentage change and average absolute percentage change in all the OV HV BPL topology subclasses examined. But, apart from Weibull and Empirical CASDs, Gaussian CASD also succeeds in successfully estimating capacity of OV HV BPL subclasses with excellent performance. As the other CASDs are concerned, Lognormal, Wald and Gumbel fail in two, three and one OV HV BPL topology subclasses, respectively. More analytically, Lognormal CASD presents a mixed capacity estimation behavior since it successfully estimates the capacity of OV HV BPL urban case B and suburban case subclasses. In accordance with [29], [30], Wald CASD is more suitable for estimating capacities of BPL subclasses that are characterized by intense "LOS" attenuation and, for that reason, Wald CASD presents the best

results when UN MV BPL topology subclasses are examined. In OV HV BPL subclasses, Wald CASD only succeeds in estimating the capacity of OV HV BPL suburban case subclass. Conversely, Gumbel CASD can be considered as a general purpose CASD which prefers OV HV BPL subclasses of low multipath aggravation.

- By recognizing the similarities and the differences of CASD performance, it is evident that OV HV BPL topologies can be treated as a middle condition between OV MV and UN MV BPL topologies. More specifically, since OV HV BPL topologies suffer from both high "LOS" attenuation due to the high 25km "LOS" transmission path and intense multipath aggravation, Gaussian CASD behaves as the suitable CASD for these complicated communications environments. In fact, Gaussian CASD is the middle solution between the Weibull and Wald CASDs of OV MV and UN MV BPL topologies, respectively. With reference to Table 3, the average absolute percentage change of Gaussian, Weibull and Wald CASD is equal to 0.012% (best), 1.02% (successful capacity estimation) and 17.24% (unsuccessful capacity estimation), respectively. Here, it should be noted that Empirical CASD of mSHM

3.3 iSHM and mSHM Class Mapping for OV HV BPL Classes for the Default Operation Settings

The definition procedures of iSHM and mSHM have been presented in [1] for the distribution BPL classes. For the case of OV HV BPL classes, two scenarios regarding the class mapping are here presented, namely: (i) iSHM definition procedure for OV HV BPL topologies; and (ii) mSHM definition procedure for OV HV BPL topologies.

As already been mentioned in Sec.3.2, Gaussian and Empirical CASDs are considered to execute successful capacity estimations because the average capacity values of the examined transmission BPL topology subclasses remain very close to the capacities of the respective indicative transmission BPL topologies. Apart from the average capacity value of the examined transmission BPL topology subclass, the minimum and maximum capacities of each transmission BPL topology subclass surround the capacity of its respective indicative transmission BPL topology while all three capacity values lie very close among them for the CASDs that execute successful capacity estimations in accordance with Figs. 1(a)-(d) of [29] and Figs. 6(a)-(d) of [30]. In this paper, the shift impact on the OV HV BPL topology class borderlines of iSHM and mSHM class maps is going to be examined when the minimum and the maximum capacities of each transmission BPL topology subclass are assumed to be applied instead of the average capacity of each subclass. The latter argument implies that the steps FL1.08 and FL2.08 of Figs. 3(a) and 3(b) of [1] that deal with the definition procedure of iSHM and mSHM, respectively, are going to be modified; instead of the computation of the average capacity of each virtual transmission BPL topology subclass, the minimum and maximum capacities are going to be considered.

As the iSHM class map scenario is concerned, with reference to Table 3, Gaussian CASD presents the best capacity estimation metric results among the other CASDs in OV HV BPL topologies. For the five indicative OV HV BPL topologies of the

main subclasses of Table 1, the respective $\hat{\mu}_{\mathbf{MLE}}^{\mathbf{Gaussian}}$ and $\hat{\sigma}_{\mathbf{MLE}}^{\mathbf{Gaussian}}$, which are the Gaussian CASD MLEs, are reported in Table 2 while the respective capacities are given in the first column of Table 3. Based on the Gaussian CASD MLEs and capacities of the five indicative OV HV BPL topologies of the main subclasses, the spacings for the horizontal and vertical axis are equal to $\frac{14.27-1\times10^{-11}}{10}=1.427$ and $\frac{2.88-0}{10}=0.288$, respectively, while the capacity borders between the adjacent distribution BPL topology classes $CBo_l^{\mathbf{G,C}}, l=1,2,3,4$ are equal to 169Mbps, 202Mbps, 233Mbps and 281Mbps, respectively.

The iSHM class map of OV HV BPL topologies is plotted in Fig. 4(a) with respect to $\hat{\mu}_{\mathbf{MLE}}^{\mathbf{Gaussian}}$ and $\hat{\sigma}_{\mathbf{MLE}}^{\mathbf{Gaussian}}$ for the default operation settings when the minimum capacity of each OV HV BPL topology subclass of step FL1.08 of Fig.3(a) of [1] is considered instead of the average capacity. In the same class map, the Gaussian CASD MLEs of the five indicative OV HV BPL topologies of the main subclasses of Table 1 with the corresponding capacities are also shown. In Figs. 4(b) and 4(c), same plots with Fig. 4(a) are demonstrated but for the case of average and maximum capacities, respectively.

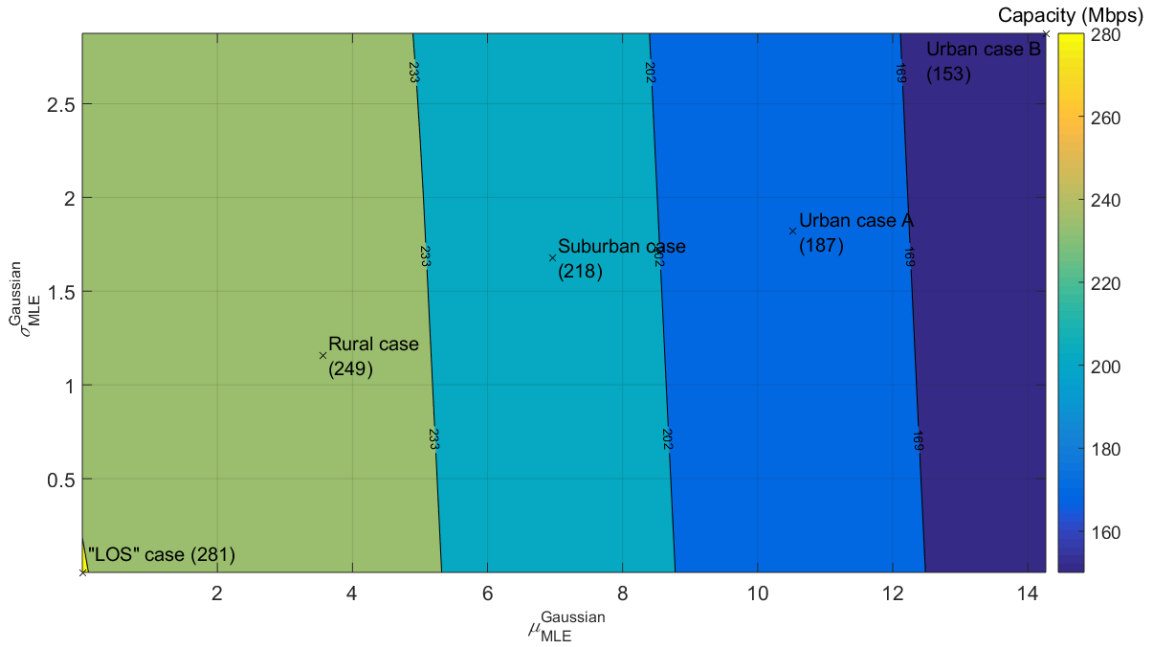
Capacity (Mbps)
280
260
240
220
200
180
160
Urban case B
(153)
Urban case A
(187)
Suburban case
(218)
Rural case
(249)
"LOS" case (281)
233
202
169
$\sigma_{MLE}^{Gaussian}$
$\mu_{MLE}^{Gaussian}$
2
4
6
8
10
12
14
0.5
1
1.5
2
2.5

(a)

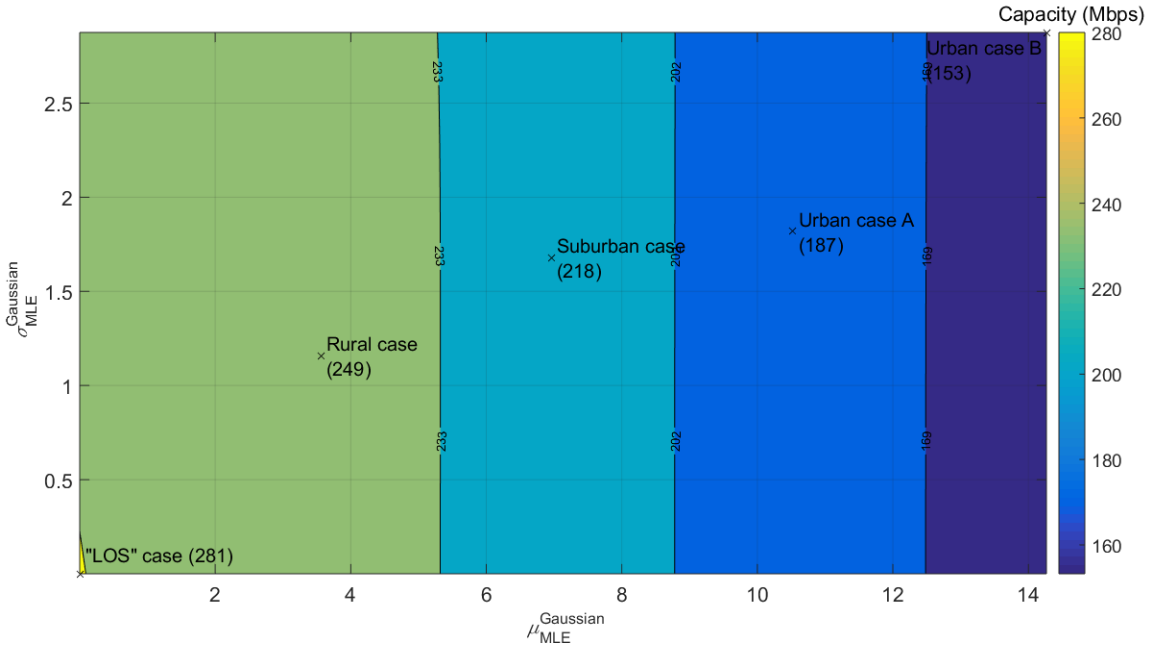
Capacity (Mbps)
280
260
240
220
200
180
160
Urban case B
(153)
Urban case A
(187)
Suburban case
(218)
Rural case
(249)
"LOS" case (281)
233
202
169
$\sigma_{MLE}^{Gaussian}$
$\mu_{MLE}^{Gaussian}$
2
4
6
8
10
12
14
0.5
1
1.5
2
2.5

(b)

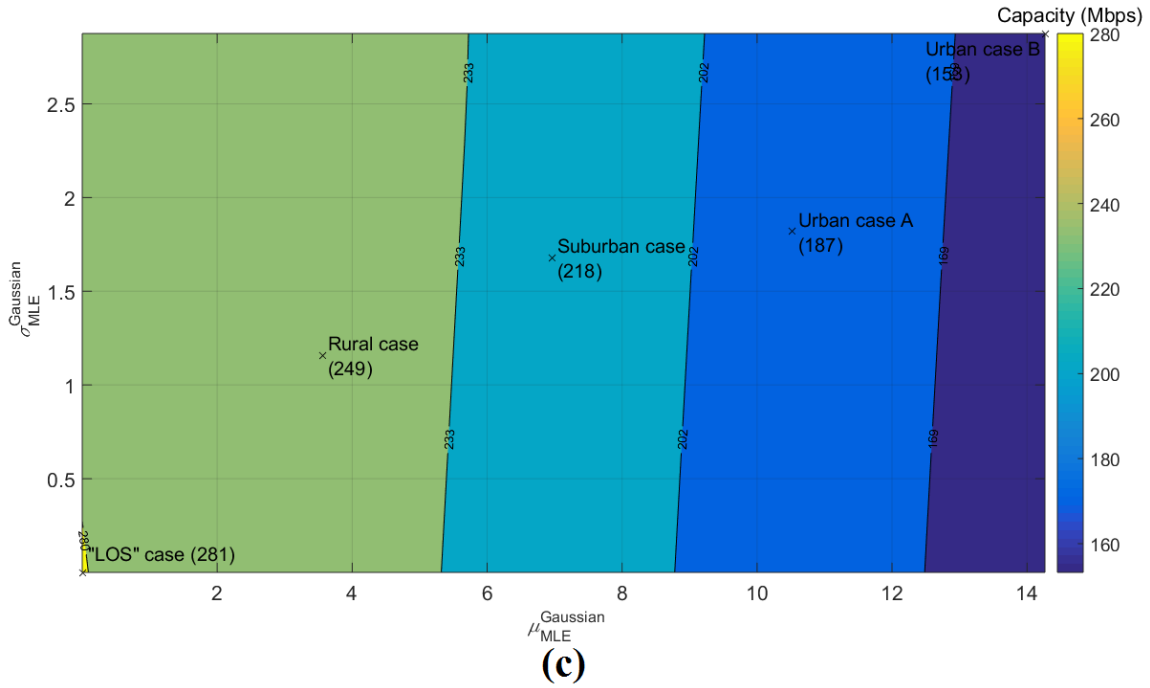

(c)

Fig. 4. iSHM class map of the OV HV BPL topologies in the 3-30MHz frequency band when WtG[1] coupling scheme is deployed and FCC Part 15 is applied. (a) Minimum capacities of OV HV BPL topology subclasses. (b) Average capacities of OV HV BPL topology subclasses. (c) Maximum capacities of OV HV BPL topology subclasses.

As the mSHM class map scenario is concerned, in accordance with [1], [2], all the four indicative OV HV BPL topologies of the main subclasses of Table 1, except for the OV HV "LOS" case, are examined separately during the preparation of mSHM class maps. Since the behavior of different indicative OV HV BPL topologies of the main subclasses has been examined in [2], only one of the indicative OV HV BPL topologies of the main subclasses is going to be examined in this paper, say, the OV HV BPL urban case A. As the horizontal shifts, vertical shifts, horizontal shift spacings and vertical shift spacings of the mSHM class maps of OV HV BPL topologies are considered, these are assumed to receive the same values with the respective ones of the mSHM class maps of OV MV and UN MV BPL topologies, which are reported in [2]; say, the maximum and minimum horizontal shift is assumed to be equal to 30dB and -30dB, respectively, while the maximum and minimum vertical shift is assumed to be equal to 1 and 0, respectively. The capacity borders between the adjacent OV HV BPL topology classes $CBo_l^{G,C}, l = 1, 2, 3, 4$ are equal to the respective capacity borders during the preparation of the iSHM class maps.

The mSHM class map of OV HV BPL topologies is plotted in Fig. 5(a) with respect to the horizontal shift h_shift and vertical shift v_shift for the default operation settings when the minimum capacity of each OV HV BPL topology subclass of step FL2.08 of Fig.3(b) of [1] is assumed. In the same 2D contour plot, the capacity borders between the adjacent transmission BPL topology classes and the capacity of the reference indicative OV HV BPL urban case A of Table 1 are also shown. In Figs. 5(b) and 5(c), same plots with Fig. 5(a) are demonstrated but for the case of average and maximum capacities, respectively.

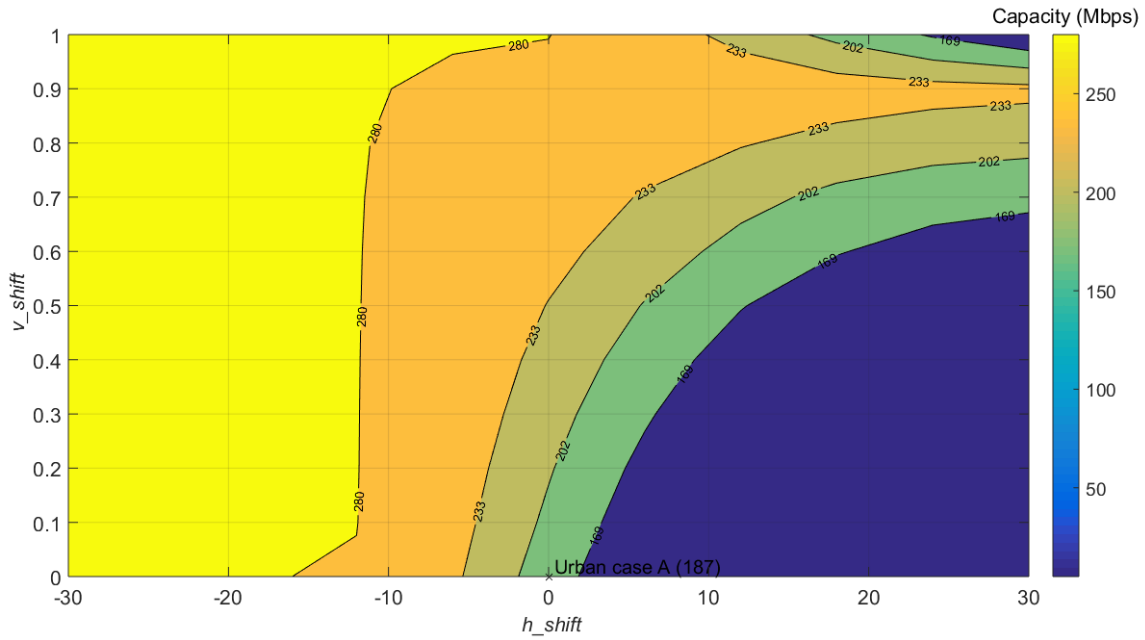
Capacity (Mbps)
v_shift
h_shift
Urban case A (187)

(a)

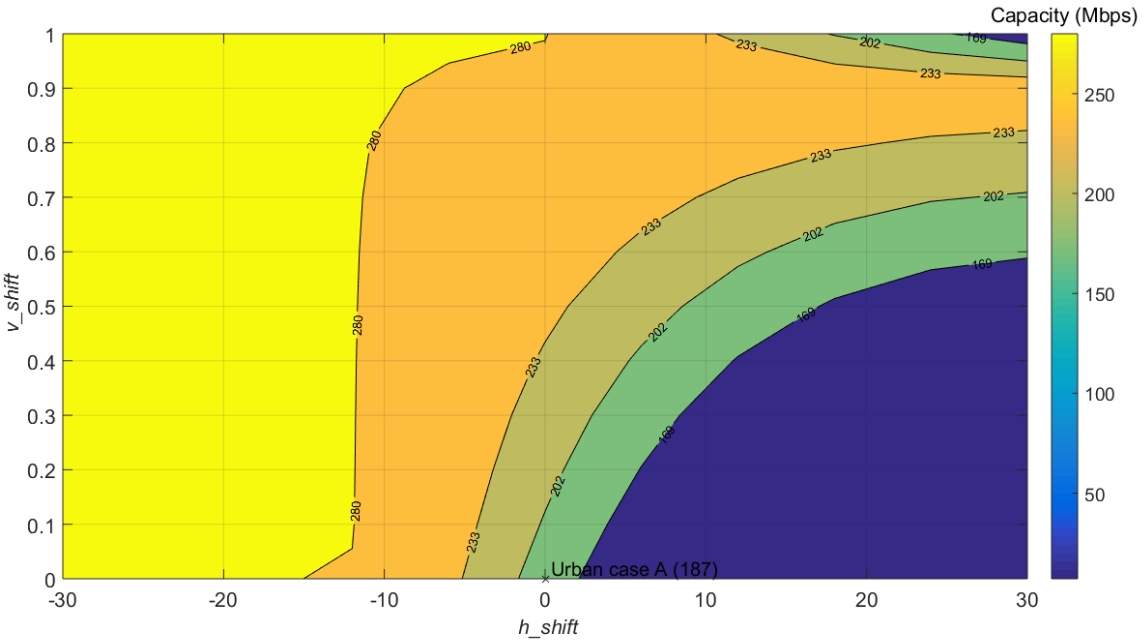
Capacity (Mbps)
v_shift
h_shift
Urban case A (187)

(b)

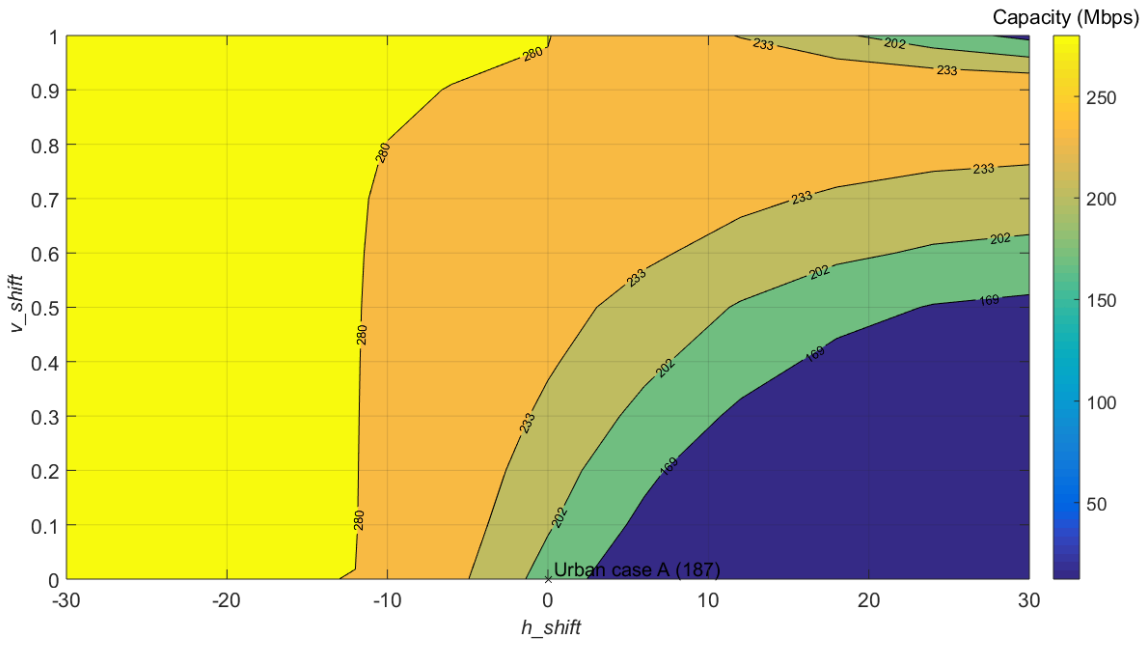

Fig. 5. mSHM class map of the OV HV BPL topologies in the 3-30MHz frequency band when StP[1] coupling scheme is deployed and FCC Part 15 is applied for reference indicative OV HV BPL urban case A. (a) Minimum capacities of OV HV BPL topology subclasses. (b) Average capacities of OV HV BPL topology subclasses. (c) Maximum capacities of OV HV BPL topology subclasses.

By observing Figs. 4(a)-(c) and Figs. 5(a)-(c), several interesting conclusions can be reported concerning the iSHM and mSHM class maps, namely:

- By comparing iSHM class maps of OV HV BPL topologies against iSHM class maps of OV MV and UN MV BPL topologies, which are presented in [2], iSHM class maps of OV HV BPL topologies present more similarities to the iSHM class maps of UN MV BPL topologies due to the existence of five almost rectangle capacity areas between the computed borders; say, the slope of the capacity area borderlines relative to the horizontal axis is almost equal to 90 degrees. As the mSHM class maps of OV HV BPL topologies are concerned, these are similar in format to the mSHM class maps of OV MV and UN MV BPL topologies, which are presented in [2]. Anyway, the mSHM class maps are characterized by a large left capacity area of respective "LOS" case capacity value while a large capacity degrading area at the bottom right side of the class maps occurs.
- Similarly to $\hat{\alpha}_{\mathrm{MLE}}^{\mathrm{Weibull}}$ and $\hat{\mu}_{\mathrm{MLE}}^{\mathrm{Wald}}$ of OV MV and UN MV BPL topology subclasses, respectively, in iSHM class maps of [2], as the multipath environment of the examined OV HV BPL topologies becomes more intense with frequent and deep spectral notches, this has as a result the value increase of $\hat{\mu}_{\mathrm{MLE}}^{\mathrm{Gaussian}}$ and $\hat{\sigma}_{\mathrm{MLE}}^{\mathrm{Gaussian}}$. Hence, OV HV BPL urban topologies tend to be located at the right areas of the class map while the OV HV BPL rural topologies tend to be located at the left areas.

- By comparing Figs. 4(a)-(c) of iSHM class maps, there are differences concerning the slope of the capacity area borderlines when the minimum, the average and the maximum capacity of each transmission BPL topology subclass are considered, respectively. Actually, when the minimum capacity of the OV HV BPL topology subclasses is assumed, the slope of the capacity area borderlines relative to the horizontal axis becomes more than 90 degrees whereas the slope of the capacity area borderlines relative to the horizontal axis becomes less than 90 degrees when the maximum capacity of the OV HV BPL topology subclasses is considered. This is due to the fact that $\hat{\sigma}_{\mathrm{MLE}}^{\mathrm{Gaussian}}$ of eq. (A3) of [28] can be treated as the variance of the normal distribution that describes the deviation of a random coupling scheme channel attenuation difference from its mean while $\hat{\mu}_{\mathrm{MLE}}^{\mathrm{Gaussian}}$ of eq.(A2) of [28] describes the mean. Hence, as $\hat{\sigma}_{\mathrm{MLE}}^{\mathrm{Gaussian}}$ increases for given $\hat{\mu}_{\mathrm{MLE}}^{\mathrm{Gaussian}}$, so decreases the minimum capacity of the OV HV BPL topology subclasses that anyway depends on the coupling scheme channel attenuation thus having as effect the shift of the capacity areas to the left. The opposite effect holds for the study of the maximum capacity of the OV HV BPL topology subclass, where the increase of $\hat{\sigma}_{\mathrm{MLE}}^{\mathrm{Gaussian}}$ triggers the increase of the maximum capacity of the OV HV BPL topology subclasses.
- Similarly to the iSHM class map of Fig. 4(b), mSHM class maps of Fig. 5(b) can support a plethora of virtual OV HV BPL topology subclasses by simply identifying the five capacity areas and by setting the corresponding pair of horizontal and vertical shifts of the coupling scheme channel attenuation of the reference OV HV BPL topology; say OV HV BPL urban case A.
- By comparing Figs. 5(a)-(c), it is obvious that the selection among the minimum, average and maximum capacity of each OV HV BPL topology subclass has very small impact on the location of capacity area borderlines of mSHM class maps (*i.e.*, the shift of the capacity area borderlines is almost zero) and this is due to the definition procedure of mSHM, which has been presented in [1]. By comparing steps FL1.06 of iSHM of Fig.3(a) of [1] and FL2.06 of mSHM of Fig.3(b) of [1], the modification of CASD MLEs of iSHM and the creation of CASD MLE pairs have as a result the definition of new virtual CDFs that are characterized by different CDF characteristics than the indicative CDF ones. Conversely, the definition of horizontal and vertical shifts of mSHM and the creation of Empirical CDF shift pair have as a result the definition of new virtual CDFs that are related in format to the representative Empirical CDF. Note that the successful capacity estimation performance of Empirical CASD implies that the average capacity value of all the examined OV HV BPL topology subclasses remain close to the respective minimum and maximum capacity values, as already been mentioned in Sec.3.2, and the latter observation combined with the simple linear modifications of the representative Empirical CDF through the horizontal and vertical shifts is reflected on the capacity range of all the examined OV HV BPL topology subclasses and, thus, on the small impact on the location of capacity area borderlines of mSHM class maps.

With reference to Table 3, although the capacity performance metrics of Gaussian CASD of iSHM and Empirical CASD of mSHM reveal the capacity estimation success of the aforementioned CASDs, the metrics of Gaussian CASD are better than the ones of

Empirical CASD. However, a possible trade-off between the capacity estimation performance and the simulation time, which has been proposed in [2], should be examined in this paper for the OV HV BPL topologies; say, the simulation time of Gaussian CASD capacity estimation performance is examined against the respective one of Empirical CASD in Sec.3.4.

3.4 iSHM and mSHM Class Map Simulation Times for OV HV BPL Classes for the Default Operation Settings

The trade-off between the capacity performance metrics and the simulation time of class mapping, which has been proposed in [2], for given CASD is investigated for OV HV BPL classes in this Section. Already been identified in Table 3, different CASDs achieve various capacity estimation performances with respect to the percentage change and the average absolute percentage change. Despite the capacity estimation performance, a reliable CASD should, at the same time, be a successful one and also be characterized by short simulation times of class mapping so that it can provide fast and reliable results thus having practical interest. In [30], it has been shown that Wald CASD of iSHM performs the best capacity estimation performance among all CASDs of iSHM and mSHM but Empirical CASD of mSHM that also performs an excellent capacity estimation performance has almost 30 times shorter simulation time than the Wald CASD. As the OV HV BPL topologies are concerned, in Fig. 6, the simulation time of class mapping is plotted against the number of spacings for the Gaussian CASD of iSHM and Empirical CASD of mSHM when OV HV BPL urban case A is assumed.

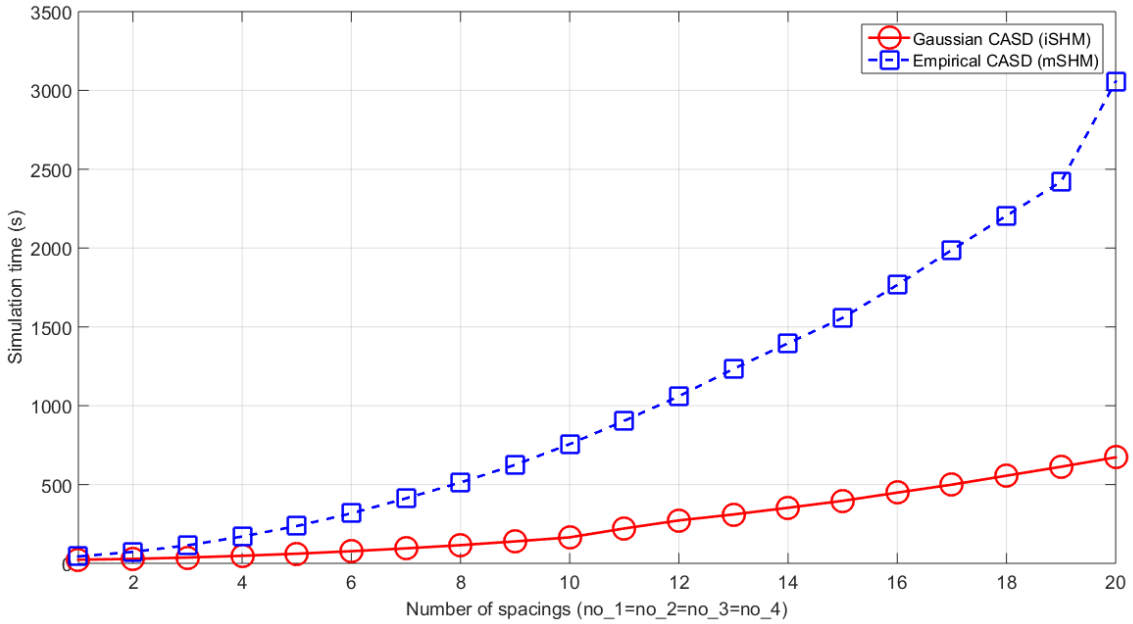

Fig. 6. Class map simulation time of the OV HV BPL urban case A in the 3-30MHz frequency band for WtG[1] coupling scheme and FCC Part 15 when different CASDs are applied and different number of spacings is used.

Note that the number of spacings (*i.e.*, no_1, no_2, no_3 and no_4) of the default operation settings is assumed to be equal to 10 either for the iSHM class maps or the mSHM class maps. From Fig. 6, the simulation time of the Gaussian CASD and Empirical CASD is equal to 164.9s and 756.3s, respectively, when the default operation settings are assumed. If the aforementioned simulation times are compared against the ones of Table 1 of [2] where the default operation settings have also been adopted, it is clear that the Empirical CASD simulation time of OV HV BPL class mapping is almost equal to the simulation time of the Empirical CASD OV MV and UN MV BPL class mapping since the larger part of the simulation time is consumed during the SHM phases and steps of the definition procedure rather than the deterministic hybrid model. As the Gaussian CASD is examined, its simulation time of OV HV BPL class mapping is significantly low and remains the lowest among the simulation times of Table 1 of [2] when the default operation settings are assumed. This indicates that the Gaussian CASD remains a reliable CASD for the preparation of the OV HV BPL class maps since it succeeds in providing the best capacity estimation results at the best simulation time.

But the main concern of the preparation of Fig. 6 is to explain the impact of the number of spacings on the simulation time of class mapping. Briefly presented in [2], the class mapping complexity is quadratic and this fact is verified in Fig. 6 either for Empirical CASD or the Gaussian CASD; *e.g.*, the expected simulation time for 20 segments is almost four times greater than the expected simulation time for 10 segments. Small differences are due to the simulation time required for the operation of the other SHM phases, steps of the definition procedure rather and the deterministic hybrid model. Regardless of the number of spacings, Gaussian CASD presents significantly lower simulation times in comparison with the one of the Empirical CASD. Hence, there is no trade-off relation between the simulation time and the capacity estimation performance in OV HV BPL topologies hence Gaussian CASD can be treated as the most reliable CASD among the examined CASDs in iSHM and mSHM for the OV HV BPL networks.

4. Conclusions

In this paper, the numerical results concerning the application of SHM (i.e, both iSHM and mSHM) to OV HV BPL topologies have first been presented. Initially, the CASD parameters of iSHM and mSHM have been computed for the indicative OV HV BPL topologies of the main subclasses. Then, with respect to the percentage change and the average absolute percentage change, Gaussian CASD of iSHM and Empirical CASD of mSHM have been reported. Gaussian CASD can be considered as the middle solution between the Weibull CASD and Wald CASD that are anyway considered as the most successful iSHM CASD for the OV MV and UN MV BPL topologies, respectively, and this is due to the fact that the transmission characteristics of OV HV BPL topologies can be treated as the mix of transmission characteristics of OV MV and UN MV BPL topologies. Moreover, on the basis of the Gaussian CASD and the Empirical CASD, the definition procedure, which has already been reported for distribution BPL topologies, has first applied to transmission BPL

topologies. The iSHM and mSHM class maps of OV HV BPL topologies have first been presented while the differences between distribution and transmission BPL topologies have been highlighted. In this paper, the impact of considering the maximum, the average and the minimum values of BPL topology subclasses instead of only the average value has been highlighted and explained. Furthermore, the trade-off between the simulation time and the capacity estimation performance has been checked if it is valid in OV HV BPL topologies. Already been identified in UN MV BPL topologies, the aforementioned trade-off is not valid in OV HV BPL topologies where Gaussian CASD can be considered the most reliable CASD; say, Gaussian CASD achieves better capacity performance metrics and simulation time than the respective ones of Empirical CASD. Finally, the impact of the number of spacings on the simulation time has been demonstrated validating the quadratic time complexity, which has theoretically explained in [2]. After the application of SHM to transmission BPL networks, new virtual transmission BPL topologies and topology subclasses can be defined that can help towards various smart grid simulation scenarios that involve power line communications technology.

CONFLICTS OF INTEREST

The author declares that there is no conflict of interests regarding the publication of this paper.

References

[1] A. G. Lazaropoulos, "Virtual Indicative Broadband over Power Lines Topologies for Respective Subclasses by Adjusting Channel Attenuation Statistical Distribution Parameters of Statistical Hybrid Models – Part 1: Theory," *Trends in Renewable Energy*, vol. 5, no. 3, pp 237-257, Aug. 2019. DOI: 10.17737/tre.2019.5.3.0099

[2] A. G. Lazaropoulos, "Virtual Indicative Broadband over Power Lines Topologies for Respective Subclasses by Adjusting Channel Attenuation Statistical Distribution Parameters of Statistical Hybrid Models – Part 2: Numerical Results for the Overhead and Underground Medium-Voltage Power Grids," *Trends in Renewable Energy*, vol. 5, no. 3, pp 258-281, Aug. 2019. DOI: 10.17737/tre.2019.5.3.00100

[3] A. G. Lazaropoulos, "Review and Progress towards the Capacity Boost of Overhead and Underground Medium-Voltage and Low-Voltage Broadband over Power Lines Networks: Cooperative Communications through Two- and Three-Hop Repeater Systems," *ISRN Electronics*, vol. 2013, Article ID 472190, pp. 1-19, 2013. [Online]. Available: http://www.hindawi.com/isrn/electronics/aip/472190/

[4] A. G. Lazaropoulos, "Deployment Concepts for Overhead High Voltage Broadband over Power Lines Connections with Two-Hop Repeater System: Capacity Countermeasures against Aggravated Topologies and High Noise

Environments," *Progress in Electromagnetics Research B*, vol. 44, pp. 283-307, 2012. [Online]. Available: http://www.jpier.org/PIERB/pierb44/13.12081104.pdf

[5] A. G. Lazaropoulos and P. G. Cottis, "Transmission characteristics of overhead medium voltage power line communication channels," *IEEE Trans. Power Del.*, vol. 24, no. 3, pp. 1164-1173, Jul. 2009.

[6] A. G. Lazaropoulos and P. G. Cottis, "Capacity of overhead medium voltage power line communication channels," *IEEE Trans. Power Del.*, vol. 25, no. 2, pp. 723-733, Apr. 2010.

[7] A. G. Lazaropoulos and P. G. Cottis, "Broadband transmission via underground medium-voltage power lines-Part I: transmission characteristics," *IEEE Trans. Power Del.*, vol. 25, no. 4, pp. 2414-2424, Oct. 2010.

[8] A. G. Lazaropoulos and P. G. Cottis, "Broadband transmission via underground medium-voltage power lines-Part II: capacity," *IEEE Trans. Power Del.*, vol. 25, no. 4, pp. 2425-2434, Oct. 2010.

[9] A. G. Lazaropoulos, "Broadband transmission and statistical performance properties of overhead high-voltage transmission networks," *Hindawi Journal of Computer Networks and Commun.*, 2012, article ID 875632, 2012. [Online]. Available: http://www.hindawi.com/journals/jcnc/aip/875632/

[10] A. G. Lazaropoulos, "Towards Modal Integration of Overhead and Underground Low-Voltage and Medium-Voltage Power Line Communication Channels in the Smart Grid Landscape: Model Expansion, Broadband Signal Transmission Characteristics, and Statistical Performance Metrics (Invited Paper)," *ISRN Signal Processing*, vol. 2012, Article ID 121628, pp. 1-17, 2012. [Online]. Available: http://www.hindawi.com/isrn/sp/2012/121628/

[11] D. G. Della amd S. Rinaldi, "Hybrid Communication Network for the Smart Grid: Validation of a Field Test Experience," *IEEE Trans. Power Del.*, vol. 30, no. 6, pp. 2492-2500, 2015.

[12] F. Versolatto and A. M. Tonello, "An MTL theory approach for the simulation of MIMO power-line communication channels," *IEEE Trans. Power Del.*, vol. 26, no. 3, pp. 1710-1717, Jul. 2011.

[13] P. Amirshahi and M. Kavehrad, "High-frequency characteristics of overhead multiconductor power lines for broadband communications," *IEEE J. Sel. Areas Commun.*, vol. 24, no. 7, pp. 1292-1303, Jul. 2006.

[14] L. Stadelmeier, D. Schneider, D. Schill, A. Schwager, and J. Speidel, "MIMO for inhome power line communications," presented at the *Int. Conf. on Source and Channel Coding*, Ulm, Germany, Jan. 2008.

[15] T. Sartenaer, "Multiuser communications over frequency selective wired channels and applications to the powerline access network" *Ph.D. dissertation*, Univ. Catholique Louvain, Louvain-la-Neuve, Belgium, Sep. 2004.

[16] T. Calliacoudas and F. Issa, ""Multiconductor transmission lines and cables solver," An efficient simulation tool for plc channel networks development," presented at the *IEEE Int. Conf. Power Line Communications and Its Applications*, Athens, Greece, Mar. 2002.

[17] S. Galli and T. Banwell, "A deterministic frequency-domain model for the indoor power line transfer function," *IEEE J. Sel. Areas Commun.*, vol. 24, no. 7, pp. 1304-1316, Jul. 2006.

[18] S. Galli and T. Banwell, "A novel approach to accurate modeling of the indoor power line channel-Part II: Transfer function and channel properties," *IEEE Trans. Power Del.*, vol. 20, no. 3, pp. 1869-1878, Jul. 2005.

[19] A. Pérez, A. M. Sánchez, J. R. Regué, M. Ribó, R. Aquilué, P. Rodréguez-Cepeda, and F. J. Pajares, "Circuital and modal characterization of the power-line network in the PLC band," *IEEE Trans. Power Del.*, vol. 24, no. 3, pp. 1182-1189, Jul. 2009.

[20] T. Sartenaer and P. Delogne, "Deterministic modelling of the (Shielded) outdoor powerline channel based on the multiconductor transmission line equations," *IEEE J. Sel. Areas Commun.*, vol. 24, no. 7, pp. 1277-1291, Jul. 2006.

[21] T. Sartenaer and P. Delogne, "Powerline cables modelling for broadband communications," in Proc. *IEEE Int. Conf. Power Line Communications and Its Applications*, Malmö, Sweden, Apr. 2001, pp. 331-337.

[22] C. R. Paul, *Analysis of Multiconductor Transmission Lines*. New York: Wiley, 1994.

[23] J. A. B. Faria, *Multiconductor Transmission-Line Structures: Modal Analysis Techniques*. New York: Wiley, 1994.

[24] H. Meng, S. Chen, Y. L. Guan, C. L. Law, P. L. So, E. Gunawan, and T. T. Lie, "Modeling of transfer characteristics for the broadband power line communication channel," *IEEE Trans. Power Del.*, vol. 19, no. 3, pp. 1057-1064, Jul. 2004.

[25] A. Semlyen and B. Gustavsen, "Phase-domain transmission-line modeling with enforcement of symmetry via the propagated characteristic admittance matrix," *IEEE Trans. Power Del.*, vol. 27, no. 2, pp. 626-631, Apr. 2012.

[26] A. M. Tonello and F. Versolatto, "Bottom-up statistical PLC channel modeling—Part I: Random topology model and efficient transfer function computation," *IEEE Transactions on Power Delivery*, vol. 26, no. 2, pp. 891-898, 2011.

[27] A. M. Tonello and F. Versolatto, "Bottom-up statistical PLC channel modeling—Part II: Inferring the statistics," *IEEE transactions on Power Delivery*, vol. 25, no. 4, pp. 2356-2363, 2010.

[28] A. G. Lazaropoulos, "Statistical Broadband over Power Lines Channel Modeling – Part 1: The Theory of the Statistical Hybrid Model," *Progress in Electromagnetics Research C*, vol. 92, pp. 1-16, 2019. [Online]. Available: http://www.jpier.org/PIERC/pierc92/01.19012902.pdf

[29] A. G. Lazaropoulos, "Statistical Broadband over Power Lines (BPL) Channel Modeling – Part 2: The Numerical Results of the Statistical Hybrid Model," *Progress in Electromagnetics Research C*, vol. 92, pp. 17-30, 2019. [Online]. Available: http://www.jpier.org/PIERC/pierc92/02.19012903.pdf

[30] A. G. Lazaropoulos, "Enhancing the Statistical Hybrid Model Performance in Overhead and Underground Medium Voltage Broadband over Power Lines Channels by Adopting Empirical Channel Attenuation Statistical Distribution," *Trends in Renewable Energy*, vol. 5, no. 2, pp. 181-217, 2019. [Online]. Available: http://futureenergysp.com/index.php/tre/article/view/96/pdf

[31] T. Oliveira, A. Picorone, C. Zeller, S. Netto, and M. Ribeiro, "Statistical Modeling of Brazilian In-Home PLC Channel Features," *Journal of Communication and Information Systems*, vol. 34, no. 1, pp. 154-168, 2019.

[32] T. R. Oliveira, C. B. Zeller, S. L. Netto, and M. V. Ribeiro, "Statistical modeling of the average channel gain and delay spread in in-home PLC channels," in *Proc. in IEEE International Symposium on Power Line Communications and Its Applications*, pp. 184-188, Mar. 2015.

[33] J. A. Cortes, F. J. Canete, L. Dıez, and J. L. G. Moreno, "On the statistical properties of indoor power line channels: Measurements and models," in *Proc. IEEE International Symposium on Power Line Communications and Its Applications*, pp. 271-276, Apr. 2011.

[34] A. G. Lazaropoulos, "Towards Broadband over Power Lines Systems Integration: Transmission Characteristics of Underground Low-Voltage Distribution Power Lines," *Progress in Electromagnetics Research B*, vol. 39, pp. 89-114, 2012. [Online]. Available: http://www.jpier.org/PIERB/pierb39/05.12012409.pdf

[35] A. Heathcote, S. Brown, and D. Cousineau, "QMPE: Estimating Lognormal, Wald, and Weibull RT distributions with a parameter-dependent lower bound," *Behavior Research Methods, Instruments, & Computers*, vol. 36, no. 2, pp. 277-290, 2004.

[36] N. Suljanović, A. Mujčić, M. Zajc, and J. F. Tasič, "Approximate computation of high-frequency characteristics for power line with horizontal disposition and middle-phase to ground coupling," *Elsevier Electr. Power Syst. Res.*, vol. 69, pp. 17-24, Jan. 2004.

[37] N. Suljanović, A. Mujčić, M. Zajc, and J. F. Tasič, "High-frequency characteristics of high-voltage power line," in *Proc. IEEE Int. Conf. on Computer as a Tool*, Ljubljana, Slovenia, Sep. 2003, pp. 310-314.

[38] N. Suljanović, A. Mujčić, M. Zajc, and J. F. Tasič, "Power-line high-frequency characteristics: analytical formulation," in *Proc. Joint 1st Workshop on Mobile Future & Symposium on Trends in Communications*, Bratislava, Slovakia, Oct. 2003, pp. 106-109.

[39] W. Villiers, J. H. Cloete, and R. Herman, "The feasibility of ampacity control on HV transmission lines using the PLC system," in *Proc. IEEE Conf. Africon*, George, South Africa, Oct. 2002, vol. 2, pp. 865-870.

[40] P. Amirshahi, "Broadband access and home networking through powerline networks" Ph.D. dissertation, Pennsylvania State Univ., University Park, PA, May 2006.

[41] M. D'Amore and M. S. Sarto, "A new formulation of lossy ground return parameters for transient analysis of multiconductor dissipative lines," *IEEE Trans. Power Del.*, vol. 12, no. 1, pp. 303-314, Jan. 1997.

[42] P. Amirshahi and M. Kavehrad, "Medium voltage overhead powerline broadband communications; Transmission capacity and electromagnetic interference," in *Proc. IEEE Int. Symp. Power Line Commun. Appl.*, Vancouver, BC, Canada, Apr. 2005, pp. 2-6.

[43] M. D'Amore and M. S. Sarto, "Simulation models of a dissipative transmission line above a lossy ground for a wide-frequency range-Part I: Single conductor configuration," *IEEE Trans. Electromagn. Compat.*, vol. 38, no. 2, pp. 127-138, May 1996.

[44] M. D'Amore and M. S. Sarto, "Simulation models of a dissipative transmission line above a lossy ground for a wide-frequency range-Part II: Multi-conductor

configuration," *IEEE Trans. Electromagn. Compat.*, vol. 38, no. 2, pp. 139-149, May 1996.

[45] A. G. Lazaropoulos, "A Panacea to Inherent BPL Technology Deficiencies by Deploying Broadband over Power Lines (BPL) Connections with Multi-Hop Repeater Systems," *Bentham Recent Advances in Electrical & Electronic Engineering*, vol. 10, no. 1, pp. 30-46, 2017.

Trends in Renewable Energy
OPEN ACCESS ISSN: 2376-2144
Peer-Reviewed Article futureenergysp.com/index.php/tre

Impact of Sunshine Duration and Clearness Index on Diffuse Solar Radiation Estimation in Mountainous Climate

Samuel Chukwujindu Nwokolo[1*], Christiana Queennet Otse[2*]

[1]*Department of Physics, Faculty of Physical Sciences, University of Calabar, Calabar, Nigeria*
[2]*Department Estate Management, Faculty of Environmental Design and Management, Obafemi Awolowo University, Ile-Ife, Nigeria*

Received November 15, 2019; Accepted November 25, 2019; Published November 30, 2019

In this paper, measured data of solar radiation was applied to develop forty-three (43) empirical models for estimation of monthly average diffuse solar radiation using clearness index, sunshine duration and a combination of them as predictors. The data covered a period of two years from May 2015 to April 2017 and was measured at Mehran University of Engineering and Technology, Hyderabad, Pakistan. Through a comprehensive statistical performance analysis, 43 dimensional models developed were tested for constructing the most accurate regression model to predict the monthly mean daily diffuse solar radiation in Hyderabad, Pakistan. On the whole, the model 42 – a hybrid of sunshine duration and clearness index predictors of diffuse fraction outperformed the remaining models proposed in this study. The best model (model 42) was then compared with 5 models and 5 measured data of diffuse solar radiation available in the literature and the NASA database by applying statistical indicators such as MBE, MPE, RMSE, RRMSE, R^2 and GPI. Through the analysis, the hybrid of sunshine duration and clearness index predictors of diffuse fraction model (model 42) was selected as the most appropriate model. The study concluded that the proposed hybrid model can serve as a baseline for the design of photovoltaic systems and estimate the monthly mean daily diffuse solar radiation on the horizontal surface for Hyderabad, Pakistan and other locations with similar local climate conditions.

Keywords: Diffuse solar radiation; Empirical models; Classification; Functional forms; Hyderabad; Pakistan

1. Introduction

Since the beginning of the 19th century, the exploitation of conventional fuels is increasingly moving towards the development of industrialization and modern life style. It has resulted in various health hazards, environmental pollution, disruption of ecosystems such as crop and animal diversity, increased global warming and many more factors which drive the earth towards a dark future. Thus, the world needs a smart energy source that is unlimited in reserve and can be applied without major contributions to atmospheric pollution and greenhouse effect.

As reported by the literature [1], the earth has been already presenting numerous signs of global climate change as follows. NASA Goddard Institute for space studies

**Correspondence:* sam31628@gmail.com, otsec@yahoo.com

Tr Ren Energy, 2019, Vol.5, No.3, 307-332. doi: 10.17737/tre.2019.5.3.00107

reported that the average temperature has climbed 0.8 degrees Celsius across the globe since 1880 and much of this in recent decades. The UN Intergovernmental Panel on Climate Change (IPCC) recorded that the last two decades of the 20th century have been the hottest in 400 years and possibly the warmest for several millennia [2]. The multinational Arctic Climate Impact Assessment reported that the Arctic is sensitive to atmospheric pollution and greenhouse effect. According to a report compiled between 2000 and 2004, the average temperatures in Alaska, Western Canada, and Eastern Russia have twice the global average. According to the IPCC 2007 report, based on the work of about 2,500 scientists in more than 130 countries, humans have caused all or most of the current planetary warming often called anthropogenic climate change. Industrialization, deforestation, and pollution have greatly increased atmospheric concentration of water vapor, carbon dioxide, methane, nitrous oxide, and all greenhouse gases that help trap heat near the Earth's surface. In fact, some experts worry that the natural cycles in Earth's orbits can alter the planet's exposure to sunlight, which may explain the current trend. Earth has indeed experienced warming and cooling cycles roughly every hundred thousand years due to these orbital shifts, but such changes have occurred over the span of several centuries. Nowadays change has taken place over the past 100 years or less.

It is therefore imperative for human beings to set a different course in its need for energy. For example, those involve less intrusive sources such as renewable energy sources, which do not harm the planet but still are inexhaustible.

In order to correct these anomalies, researchers, scientists, governmental and non-governmental organizations are striving tirelessly on renewable energy, which should be commercially viable, pollutant free, easy to access, and must be widespread in nature [3]. As a result of its minimal or zero impact on the environment and ecosystem which eventually poses no health hazards to man and animals, renewable energies such as solar energy, wind energy, hydro power, tidal energy and biofuels are more suitable compared to fossil fuel sources of energy, as these are generated from natural processes such as sunlight, wind, rain and numerous forms of biomass [4]. These smart energy sources are not only renewable but also have the ability to sustain ecology and the environment, as they are eco-friendly and do not contribute to global warming and production of greenhouse gases [3].

Solar energy among other renewable energy types has remained the most viable source, which has the capacity to sustain and maintain all activities and processes, support life of animals, heat the atmosphere and lands, generate wind, drive the water cycle, warm the ocean, generate fossil fuels, and support life of plants [3].

Solar energy is not only primarily derived from solar radiation reaching the earth's surface, but it remains important in many industrial and application areas, such as exciting electrons in a photovoltaic cell, solar heating, solar architecture, molten salt power plants and supplying energy to natural processes [3]. It also plays a major role in de-carbonizing the global economy and improving costs of greenhouse gas emitter [5]. Much more, solar radiation level is equally used to determine the type of photovoltaic technology (such as network-connected systems (on-grid), network-connected home systems, network-connected solar power plants, off-grid, hybrid systems and independent systems for economic purposes), concentrated solar power technology (like dish stirring, parabolic trough, linear Fresnel or central tower), and photovoltaic thermal (PVT, such as air-based PVT, water-based PVT, bifluid based PVT, PVT nanofluid based, PVT based phase change materials, PVT refrigerant based, PVT heat pipe based and PVT with heat pump) that should be installed at a particular site. It could also serve as a baseline for

estimating and understanding the diurnal fluctuations in multiple solar radiation parameters such as direct normal irradiance, diffuse horizontal irradiation, ground reflected solar radiation, evaporation and reference evapotranspiration.

In fact, despite the influence of the government, scientists, researchers and investors have explored solar energy as a type of renewable energy using the above-mentioned various technologies, but fundamentally, the potential of solar energy has not been fully utilized [3]. For example, the energy emitted by the sun is so high that when only 0.1% of solar energy reaching the ground is converted into electricity with only 10% efficiency, the power output will be 17,300 GW, which is 7 of the global average instantaneous power consumption in 2012 [6-8].

These are significant and potential solar radiation reaching the Earth's surface in the form of solar energy, measurement of solar radiation and its components such as diffuse solar radiation and direct normal irradiance is limited, because there are very few standard weather stations can measure. Routinely, the data for these parameters is not available in the site of interest. However, other meteorological and atmospheric variables such as ambient temperature, cloud cover, rainfall regimes, and relative humidity are often measured routinely in most weather stations across the globe, as a result of its direct application in agricultural sciences and meteorology.

Due to the cost implication, maintenance, expertise needed for ground and satellite-derived technique of measuring solar radiation data (especially in rural and developing countries), prediction of solar radiation over a particular location using mathematical models has been initiated by solar energy researchers. Mathematical modeling serves as an alternative technique of generating data of solar radiation and its components without instrumentation network that would otherwise be needed.

Some researchers have stressed that accurate determination of diffuse solar radiation is important in design and performance analysis of solar energy projects, such as for designing and sizing photovoltaic sources as the future alternative energy [9-11]. For instant, Khorasanizadeh *et al.* [12] revealed that the impact of diffuse solar radiation to the annual solar energy is nearly 20% in Tabass, Iran.

It has been observed that in different locations across the globe, ground measurement of diffuse solar radiation is either scare or absent, whereas ground measurement of global solar radiation and weather parameters such as sunlight hours and precipitation are often available as a result of their traditional use in building and construction industries, agriculture, and meteorology. By applying mathematical correlations, diffuse solar radiation can be obtained as far as global solar radiation and other popularly measured meteorological parameters are available. For this reason, solar energy researchers across the globe have developed numerous empirical models in most metropolitan cities, because most meteorological and weather stations are often situated in these locations. From the mid-19th century, solar energy researchers have developed various empirical models for estimating diffuse solar radiation employing popularly measured variables. These variables include minimum and maximum temperature, hours of solar radiation and relative humidity [13-18]. Several researchers have equally developed regression models for estimating the monthly mean daily diffuse solar radiation employing the clearness index [4, 6, 9,13, 19-31] or applying sunshine hour fraction [28, 30, 32-36] or with combination. of them [18, 37-41]. Despotovic *et al.* [42] observed that the empirical models using both clearness index and sunshine duration offer better estimation of diffuse solar radiation in the main five climate zones according to Koppen-Geiger climate classification

In spite of the vast number of studies on empirical models for estimating solar radiation across the globe, there is no recorded study in Hyderabad, Pakistan. The main objective of this study was to estimate forty-three models employed for estimating diffuse solar radiation using sunshine duration, clearness index and both of the predictors, obtain the best performing model using statistical indicators (such as mean bias error (MBE), mean percentage error (MPE), root mean square error (RRMSE), coefficient of determination (R^2) and global performance indicator (GPI)), and compare the selected best models with five models developed from the literature and five ground measured diffuse solar radiation in the literature together with satellite data obtained from NASA database for estimating diffuse solar radiation in Hyderabad, Pakistan.

2. Materials and Methods

2.1 Study Area

Hyderabad lying along the Indus River is the second largest city of Sindh province and the 8th largest city in Pakistan (Fig. 1). It has a relatively mountainous climate which is slightly more pleasant than other parts of Central Sindh throughout the year. Summer and winter are the two main seasons, while spring and autumn are very short. The period from mid-April to late June is the hottest time of the year with temperatures as high as 48.5 °C. Winters are usually warm, around 25 °C during the day time and often below 10 °C at night, and are the best time to visit the city. The highest ever recorded temperature in Hyderabad was 48.5 °C in 1991, while the lowest was 1 °C in 2012 [43, 44].

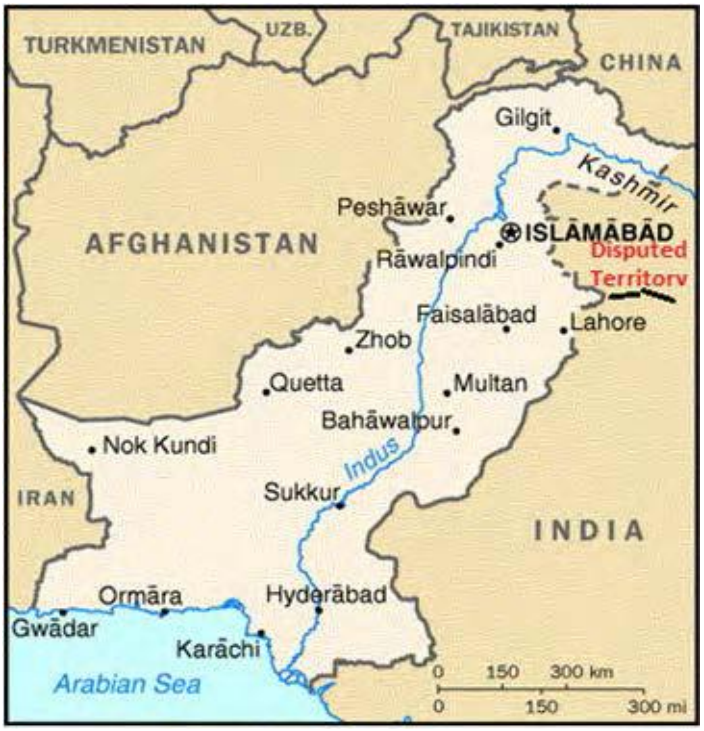

Fig. 1. Map of Pakistan showing the study site. Hyderabad at the southern part of the figure [43].

2.2 Acquisition of Data

Under the present study, the measured global solar radiation and its components (diffuse and direct solar radiation) together with other meteorological parameters were measured by the Energy Sector Management Assistance Program of The World Bank Group at Mehran University of Engineering and Technology (M-UET), Hyderabad, Pakistan [45]. The measurements were performed for a period of two years (May, 2015 - April, 2017) so as to determine regional solar radiation and other meteorological variables. However, the monthly mean daily sunshine hours (for sunshine fraction in Equation 4) were based on the 30-year period (1981-1990) using the same geographical information as M-UET were obtained from the International Water Management Institute (IWWI) website [46]. The characteristics and specification of solar and other meteorological parameter instrument used are provided in Table 1. The obtained raw data (10 minutes summarization interval values) were post-processed in order to obtain daily values of global, diffuse and direct solar radiation data and other meteorological parameters such as air temperature, relative humidity, wind speed and wind direction. The data obtained was further averaged for a month so as to calculate the monthly mean values. The measured monthly mean daily values thus obtained and sunshine hours are shown in Table 2.

Table 1. Characteristics of the used solar and meteorological instruments [45].

Sensor manufacturer	Height orientation	Sensor type	Model	Serial number
CSPS	2m	RSI	Twin-RSI	CSPS.ms.14.001-0015
Kipp & Zonen	2m	Pyranometer	CMP10	140572
Campbell Scientific	2m	Temperature and Humidity	CS215	E12267
Setra	2m	Barometric pressure	Setra 278	6015966
NRG	10m	Anemometer	NRG40C	1795-00229369
NRG	10m	Wind direction	NRG200	

Table 2. Monthly and yearly averages of measured meteorological data for Hyderabad, Pakistan

Month/Mean	H	Hb	Hd	RH	T	WS	WD	AP	S
January	14.33	14.75	6.18	60.58	17.59	3.35	153.62	1009.97	8.88
February	18.96	20.78	6.32	36.58	21.56	3.34	168.53	1008.45	9.27
March	22.02	19.48	8.36	40.93	26.92	4.02	185.86	1003.96	9.48
April	24.84	19.00	10.29	39.56	31.33	5.28	202.47	999.12	9.91
May	26.07	19.14	10.84	50.85	33.42	7.00	211.71	995.46	10.51
June	24.78	15.90	11.97	54.57	33.67	6.29	197.65	992.00	9.45
July	22.22	10.72	13.28	65.46	31.75	7.71	213.75	991.05	7.43
August	21.98	13.39	11.26	67.25	30.56	6.52	204.56	993.60	7.67
September	22.49	20.28	8.11	61.58	30.28	5.87	200.81	997.89	9.35
October	19.24	19.91	6.40	54.38	29.46	4.11	184.60	1002.79	9.89
November	16.03	18.11	5.76	42.13	24.40	3.09	166.63	1007.28	9.37
December	14.71	18.71	5.02	47.63	20.24	2.84	166.74	1009.29	8.90
Monthly Mean	20.64	17.51	8.65	51.79	27.60	4.95	188.08	1000.89	9.18
Annual Mean	7503.759	6359.958	3153.287	18590.04	10125.66	1792.051	68239.03	366458.5	-

Where monthly values and mean of global (H), diffuse (H_d) and direct (H_b) solar radiation are in $MJm^{-2}day^{-1}$ between May, 2015 – April 2017, annual mean of global (H), diffuse (H_d) and direct (H_b) solar radiation are in $MJm^{-2}year^{-1}$ in 2016 only, RH represents relative humidity in (%), T stands for air temperature in (^oC), WS designates wind speed in (m/s), WD represents wind direction in (0 – 360), AP stands for Ambient air pressure in (hPa) and S represents monthly mean sunshine hours downloaded from IWMI website [46] in hrs.

2.3 Basic Parameters

The fundamental requirements such as maximum possible sunshine hours (S_o) and extraterrestrial solar radiation on the horizontal surface (H_o) are significant for the prediction of diffuse solar radiation expressed as mathematically as given by Yaniktepe and Gene [47]:

$$H_O = \frac{24}{\pi} I_{SC}\left(1 + 0.033\cos\frac{360n}{365}\right) \times \left(\cos\phi\cos\delta\sin\omega_S + \frac{2\pi\omega_S}{360}\sin\phi\sin\delta\right) \quad (1)$$

Where the mean sunrise hour angle (ω_S) can be evaluated as:

$$\omega_s = \cos^{-1}\left[-\tan\delta\tan\phi\right] \quad (2)$$

The solar declination (δ) is given by Yaniktepe and as Genc [47] as:

$$\delta = 23.45\sin\left[\frac{360(n+284)}{365}\right] \quad (3)$$

where I_{SC} is the solar constant, ϕ is the latitude and n the number of days of the year starting from first January.

The maximum possible sunshine duration is calculated as:

$$S_o = \frac{2}{15}\cos^{-1}\left[-\tan\delta\tan\phi\right] \quad (4)$$

where other symbols retain their usual meaning.

2.4 Statistical Modeling

Estimation of diffuse component of global solar radiation involves modeling the monthly mean diffuse fraction or diffuse coefficient as a function of monthly mean sunshine fraction, clearness index and combination of sunshine fraction and clearness index. This could be attributed to the fact that lower fluctuations are often observed in monthly mean values of solar radiation from one month to another as component to daily values of solar radiation [22]. Hence, better estimation capacity is observed in monthly mean models [22].

Peers and researchers have stressed that validating training dataset using the same dataset of training might lead to partially validated results [21, 48], thus, an independent validation dataset which involves that validating patterns have not been previously applied for training dataset is often employed. However, as a result of the short-term measure employed in this study (2 years), the present study employed dataset during May, 2015 - April, 2016 to develop the models for the station while validation dataset during May, 2016 - April, 2017 was used to test the models. This measure was employed to prevent the models from over fitting and to determine the estimation capacity of the developed models.

In diffuse solar radiation estimation, an empirical model uses diffuse fraction (H_d/H) or diffuse coefficient (H_d/H_o) with other easily measurable parameters. Moreover, since the first primitive work of Liu and Jordan [49] that estimated the mean diffuse solar radiation, numerous solar energy researchers have proposed several models in order to elaborate the Liu and Jordan model's functional form. The relationships representing the diffuse radiation are classified into three main classes: (1) sunshine duration-based models, (2) clearness index-based models, and (3) sunshine and clearness index-based models [50]. Owing to these classifications, the diffuse fraction (H_d/H), and diffuse coefficient (H_d/H_o) correlations were used in estimating the diffuse solar radiation in Hyderabad, Pakistan.

2.4.1 Clearness Index-Based Models

According to Nwokolo and Ogbulieze [50], models of the monthly mean diffuse fraction (H_d/H) and the diffuse coefficient (H_d/H_o) is a function of the clearness index; such that

$$\left(\frac{H_d}{H}, \frac{H_d}{H_o}\right) \approx f\left(\frac{H}{H_o}\right) \tag{5}$$

The proposed models under this class is shown in Table 3a.

2.4.2 Sunshine Duration-Based Models

Numerous models have been widely applied sunshine fraction (S/S_o) in associating the ratio of diffuse solar radiation (H_d) to often expressed as diffuse fraction (H_d/H), and the monthly average diffuse coefficient (H_d/H_o) to sunshine fraction or combination of both. Varying degrees of polynomial functions such as linear and quadratic, logarithmic and exponential models are applied for this study. Where S is the monthly mean daily hours of sunshine; such that

$$\left(\frac{H_d}{H}, \frac{H_d}{H_o}\right) \approx f\left(\frac{S}{S_o}\right) \tag{6}$$

The developed models under this class is shown in Table 3b.

2.4.3 Sunshine Duration and Clearness Index-Based Models

Under this class, the monthly mean diffuse fraction (H_d/H) and the diffuse coefficient (H_d/H_o) are function of the clearness index and sunshine fraction; such that

$$\left(\frac{H_d}{H}, \frac{H_d}{H_o}\right) \approx f\left(\frac{H}{H_o}, \frac{S}{S_o}\right) \tag{7}$$

The developed models under this class is shown in Table 3c.

2.5 Comparison of Models

In order to check the capacity and accuracy of the estimated data from the measured data in this study, numerous statistical indicators are applied [22-24, 42]. These metrics include mean bias error (MBE), mean percentage error (MPE), root mean square error (RMSE), relative root mean square error (RRMSE) and coefficient of determination (R^2) as presented in equation (8 - 12).

$$MBE = \frac{1}{n}\sum_{i=1}^{n}\left(H_d^{est} - H_d^{mea}\right) \tag{8}$$

$$MPE = \frac{100}{n}\sum_{i=1}^{n}\left(\frac{H_d^{mea} - H_d^{est}}{H_d^{mea}}\right) \tag{9}$$

$$RMSE = \left[\frac{1}{n}\sum_{i=1}^{n}\left(H_d^{est} - H_d^{mea}\right)^2\right]^{1/2} \tag{10}$$

Table 3a. Monthly mean diffuse solar radiation models under clearness index-based models

S/N	Parameters	Type	Regression relations	Model
1	$\frac{H}{H_o}$	Linear	$\frac{H_d}{H} = 1.646 - 1.957\left(\frac{H}{H_o}\right)$	1
2	$\frac{H}{H_o}$	Quadratic	$\frac{H_d}{H} = 6.062 - 16.466\left(\frac{H}{H_o}\right) + 11.8676\left(\frac{H}{H_o}\right)^2$	2
3	$\frac{H}{H_o}$	Polynomial	$\frac{H_d}{H} = 4.581 - 9.196\left(\frac{H}{H_o}\right) + 6.442\left(\frac{H}{H_o}\right)^3$	3
4	$\frac{H}{H_o}$	Polynomial	$\frac{H_d}{H} = 3.841 - 6.773\left(\frac{H}{H_o}\right) + 5.235\left(\frac{H}{H_o}\right)^4$	4
5	$\frac{H}{H_o}$	Linear	$\frac{H_d}{H_o} = 0.721 - 0.735\left(\frac{H}{H_o}\right)$	5
6	$\frac{H}{H_o}$	Quadratic	$\frac{H_d}{H_o} = 2.680 - 7.173\left(\frac{H}{H_o}\right) + 5.265\left(\frac{H}{H_o}\right)^2$	6
7	$\frac{H}{H_o}$	Polynomial	$\frac{H_d}{H_o} = 2.025 - 3.952\left(\frac{H}{H_o}\right) + 2.862\left(\frac{H}{H_o}\right)^3$	7
8	$\frac{H}{H_o}$	Polynomial	$\frac{H_d}{H_o} = 1.698 - 2.878\left(\frac{H}{H_o}\right) + 2.329\left(\frac{H}{H_o}\right)^4$	8
9	$In\frac{H}{H_o}$	Logarithmic	$\frac{H_d}{H_o} = 0.049 - 0.451\left(In\frac{H}{H_o}\right)$	9
10	$In\frac{H}{H_o}$	Logarithmic	$\frac{H_d}{H} = -0.143 - 1.199\left(In\frac{H}{H_o}\right)$	10
11	$\exp\frac{H}{H_o}$	Exponential	$\frac{H_d}{H} = 2.401 - 1.058\left(\exp\frac{H}{H_o}\right)$	11
12	$\exp\frac{H}{H_o}$	Exponential	$\frac{H_d}{H} = 4.912 - 8.495\left(\exp\frac{H}{H_o}\right) + 7.690\left(\exp\frac{H}{H_o}\right)^2$	12
13	$\exp\frac{H}{H_o}$	Exponential	$\frac{H_d}{H_o} = 1.004 - 0.397\left(\exp\frac{H}{H_o}\right)$	13
14	$\exp\frac{H}{H_o}$	Exponential	$\frac{H_d}{H_o} = 2.109 - 3.668\left(\exp\frac{H}{H_o}\right) + 3.382\left(\exp\frac{H}{H_o}\right)^2$	14

Table 3b. Monthly mean diffuse solar radiation models under sunshine duration-based models

S/N	Parameters	Type	Regression relations	Model
15	$\frac{S}{S_0}$	Linear	$\frac{H_d}{H} = 0.973 - 0.733\left(\frac{S}{S_o}\right)$	15
16	$\frac{S}{S_0}$	Quadratic	$\frac{H_d}{H} = 1.394 - 1.952\left(\frac{S}{S_o}\right) + 0.860\left(\frac{S}{S_o}\right)^2$	16
17	$\frac{S}{S_0}$	Polynomial	$\frac{H_d}{H} = 1.246 - 1.328\left(\frac{S}{S_o}\right) + 0.390\left(\frac{S}{S_o}\right)^3$	17
18	$\frac{S}{S_0}$	Polynomial	$\frac{H_d}{H} = 1.172 - 1.122\left(\frac{S}{S_o}\right) + 0.263\left(\frac{S}{S_o}\right)^4$	18
19	$\frac{S}{S_0}$	Linear	$\frac{H_d}{H_o} = 0.500 - 0.317\left(\frac{S}{S_o}\right)$	19
20	$\frac{S}{S_0}$	Quadratic	$\frac{H_d}{H_o} = 0.274 + 0.336\left(\frac{S}{S_o}\right) - 0.461\left(\frac{S}{S_o}\right)^2$	20
21	$\frac{S}{S_0}$	Polynomial	$\frac{H_d}{H_o} = 0.348 + 0.015\left(\frac{S}{S_o}\right) - 0.217\left(\frac{S}{S_o}\right)^3$	21
22	$\frac{S}{S_0}$	Polynomial	$\frac{H_d}{H_o} = 0.385 - 0.092\left(\frac{S}{S_o}\right) - 0.152\left(\frac{S}{S_o}\right)^4$	22
23	$In\frac{S}{S_o}$	Logarithmic	$\frac{H_d}{H_o} = 0.197 - 0.219\left(In\frac{S}{S_o}\right)$	23
24	$\exp\frac{S}{S_o}$	Exponential	$\frac{H_d}{H_o} = 0.594 - 0.156\left(\exp\frac{S}{S_o}\right)$	24
25	$\exp\frac{S}{S_o}$	Exponential	$\frac{H_d}{H_o} = 0.493 - 0.010\left(\exp\frac{S}{S_o}\right) - 0.140\left(\exp\frac{S}{S_o}\right)^2$	25
26	$In\,S/S_o$, $\exp S/S_o$	Exponential and logarithmic	$\frac{H_d}{H_o} = 0.897 + 0.170\left(In\frac{S}{S_o}\right) - 0.275\left(\exp\frac{S}{S_o}\right)$	26
27	$In\frac{S}{S_o}$	logarithmic	$\frac{H_d}{H} = 0.270 - 0.514\left(In\frac{S}{S_o}\right)$	27
28	$In\frac{S}{S_o}$	logarithmic	$\frac{H_d}{H} = 0.270 - 0.257\left(In\frac{S}{S_o}\right)^2$	28
29	$\exp\frac{S}{S_o}$	Exponential	$\frac{H_d}{H} = 1.184 - 0.357\left(\exp\frac{S}{S_o}\right)$	29

30	$\exp\frac{S}{S_o}$	Exponential	$\frac{H_d}{H} = 1.500 - 0.971\left(\exp\frac{S}{S_o}\right) + 0.519\left(\exp\frac{S}{S_o}\right)^2$	30
31	$In\,S/S_o$, $\exp S/S_o$	Exponential and logarithmic	$\frac{H_d}{H} = -0.114 + 0.150\left(\exp\frac{S}{S_o}\right) - 0.727\left(In\frac{S}{S_o}\right)$	31

Table 3c. Monthly mean diffuse solar radiation models under sunshine duration and clearness index-based models

S/N	Parameters	Regression relations	Model
32	$\frac{H}{H_o}, \frac{S}{S_o}$	$\frac{H_d}{H} = 1.368 - 0.942\left(\frac{H}{H_o}\right) - 0.4732\left(\frac{S}{S_o}\right)$	32
33	$\frac{H}{H_o}, \frac{S}{S_o}$	$\frac{H_d}{H} = 0.807 + 0.903\left(\frac{H}{H_o}\right) - 0.486\left(\frac{S}{S_o}\right) - 1.487\left(\frac{H}{H_o}\right)^2$	33
34	$\frac{H}{H_o}, \frac{S}{S_o}$	$\frac{H_d}{H} = 3.638 - 11.949\left(\frac{H}{H_o}\right) + 3.038\left(\frac{S}{S_o}\right) + 8.437\left(\frac{H}{H_o}\right)^2 - 2.322\left(\frac{S}{S_o}\right)^2$	34
35	$\frac{H}{H_o}, \frac{S}{S_o}$	$\frac{H_d}{H} = 3.748 - 10.977\left(\frac{H}{H_o}\right) + 1.329\left(\frac{S}{S_o}\right) + 7.667\left(\frac{H}{H_o}\right)^2 - 1.044\left(\frac{S}{S_o}\right)^3$	35
36	$\frac{H}{H_o}, \frac{S}{S_o}$	$\frac{H_d}{H} = 2.740 - 6.126\left(\frac{H}{H_o}\right) + 1.301\left(\frac{S}{S_o}\right) - 1.029\left(\frac{S}{S_o}\right)^3 + 4.036\left(\frac{H}{H_o}\right)^3$	36
37	$\frac{H}{H_o}, \frac{S}{S_o}$	$\frac{H_d}{H_o} = 0.557 - 0.136\left(\frac{H}{H_o}\right) - 0.279\left(\frac{S}{S_o}\right)$	37
38	$\frac{H}{H_o}, \frac{S}{S_o}$	$\frac{H_d}{H_o} = -0.627 + 3.758\left(\frac{H}{H_o}\right) - 0.306\left(\frac{S}{S_o}\right) - 3.139\left(\frac{H}{H_o}\right)^2$	38
39	$\frac{H}{H_o}, \frac{S}{S_o}$	$\frac{H_d}{H_o} = 1.325 - 5.105\left(\frac{H}{H_o}\right) + 2.125\left(\frac{S}{S_o}\right) + 3.705\left(\frac{H}{H_o}\right)^2 - 1.602\left(\frac{S}{S_o}\right)^2$	39
40	$\exp\frac{H}{H_o}, \frac{S}{S_o}$	$\frac{H_d}{H} = 1.524 - 0.228\left(\exp\frac{S}{S_o}\right) - 0.984\left(\frac{H}{H_o}\right)$	40
41	$\frac{H}{H_o}, \exp\frac{S}{S_o}$	$\frac{H_d}{H} = 1.260 - 0.230\left(\exp\frac{S}{S_o}\right) - 0.111\left(\frac{H}{H_o}\right) - 0.705\left(\frac{H}{H_o}\right)^2$	41
42	$\frac{H}{H_o}, \exp\frac{S}{S_o}$	$\frac{H_d}{H} = 3.459 + 0.886\left(\exp\frac{S}{S_o}\right) - 9.411\left(\frac{H}{H_o}\right) + 6.429\left(\frac{H}{H_o}\right)^2 - 0.870\left(\exp\frac{S}{S_o}\right)^2$	42
43	$\frac{H}{H_o}, In\frac{S}{S_o}$	$\frac{H_d}{H} = 0.880 - 0.890\left(\frac{H}{H_o}\right) - 0.338\left(In\frac{S}{S_o}\right)$	43

$$RRMSE = \frac{\left[\frac{1}{n}\sum_{i=1}^{n}\left(H_d^{est} - H_d^{mea}\right)^2\right]^{1/2}}{\frac{1}{n}\sum_{i=1}^{n}H_d^{mea}} \times 100 \quad (11)$$

$$R^2 = 1 - \frac{\sum_{i=1}^{n}\left(H_d^{mea} - H_d^{est}\right)^2}{\sum_{i=1}^{n}\left(H_d^{mea} - H_d^{avemea}\right)^2} \quad (12)$$

where n in this section represents the total number of available data point (12), H_d^{est} = estimated diffuse solar radiation, H_d^{mea} = measured diffuse solar radiation, and H_d^{avemea} = average of measured diffuse solar radiation.

In order to check and select the best model out of the 43 recommended models used in this study, a global performance indicator (GPI) was applied. Applying the GPI newly introduced by Bailek *et al.* [37] and Despotovic *et al.* [51] on the 43 models developed in this study undoubtedly revealed the best model. The established best model was then used to compare the five measured data and five diffuse solar radiation models reported in the literature from different locations across the globe as presented in Tables 4 - 5. This was established in order to check if the accuracy and application of the best model is limited to the site from which the model was developed. This technique was applied because peers and researchers from the time immemorial reported that diffuse solar radiation is dependent on local climate and geographical location [22-24, 42, 50]. Also, GPI was applied in this section for selecting the best performing model out of 43 models and for comparing with the literature because of the following: (1) The GPI combines the advantages of the statistical indicators presented in equation (8 - 12) in order to reveal the best performing model, and (2) with the application of GPI, a single value which consists of short- and long-term statistical performances together with the linearity of the models will be clearly observed and selected. However, Bailek *et al.* [37] stressed that the GPI is a relative unbounded value and a higher value of the GPI implies a better statistical performance and modeling quality. According to Despotovic *et al.* [51] and Jamil and Akhtar [22], the values of all selected statistical indicators need to be scaled down so that the scaled values lie between 0 and 1. These scaled values are subtracted from the median value of the corresponding scaled statistical indicators. Finally, the values obtained are summed applying appropriate weight factors.

This indicator (GPI) is defined mathematically as:

$$GPI = \sum_{i=1}^{5}\alpha_j\left(\bar{y}_i - \bar{y}_{ij}\right) \quad (13)$$

Where α_j equal -1 for the indicator R^2 only, whereas for other indicators (MBE, MPE, RMSE and RRMSE) is equal to 1. $\bar{y}_i$ is the median of scaled values of the indicators j, $\bar{y}_{ij}$ is the scaled value of indicator j for model i. The higher the values of GPI indicator, the better the accuracy of model.

Table 4. Monthly mean diffuse solar radiation models obtained from literature

Model	Parameters	Class	Regression relations	Reference
44	$\frac{H}{H_o}$	Clearness index-based model	$\frac{H_d}{H} = 1.0 - 1.13\left(\frac{H}{H_o}\right)$	Page [25]
45	$\frac{H}{H_o}$	Clearness index-based model	$\frac{H_d}{H} = 0.958 - 0.982\left(\frac{H}{H_o}\right)$	Iqbal [13]
46	$\frac{H}{H_o}$	Clearness index-based model	$\frac{H_d}{H} = 0.636 - 0.279\left(\frac{H}{H_o}\right) - 0.194\left(\frac{H}{H_o}\right)^2 - 0.383\left(\frac{H}{H_o}\right)^3$	Ibraham [28]
47	$\frac{H}{H_o}$	Clearness index-based model	$\frac{H_d}{H} = 1.390 - 4.027\left(\frac{H}{H_o}\right) + 5.531\left(\frac{H}{H_o}\right)^2 - 3.108\left(\frac{H}{H_o}\right)^3$	Liu & Jordan [49]
48	$\frac{H}{H_o}, \frac{S}{S_o}$	Clearness index and sunshine duration-based model	$\frac{H_d}{H_o} = 0.385 - 0.12\left(\frac{H}{H_o}\right) + 0.067\left(\frac{S}{S_o}\right)^2$	Maduekwe & Chendo [52]

Table 5. Measured monthly mean diffuse solar radiation obtained from the literature and the NASA website [62]

Lat.	Lon.	Ele.	Jan	Feb	Mar	Apr	May	Jun	Jul	Aug	Sep	Oct	Nov	Dec
Kerman, Iran between 1990-2005 Safaripour and Mehrabian [53]														
30.3 N	NA	NA	5.23	6.14	8.06	8.60	8.16	7.46	7.41	6.88	5.86	4.92	3.98	4.44
Aligarh Muslim University, Aligarh, India between 2013-2016 Jamil and Akhtar [22]														
27.9 N	78.1 E	NA	6.19	7.07	7.92	8.21	8.64	9.06	8.68	8.53	6.32	8.02	6.78	5.87
University of Tarapaca site of Arica-Parinacota, Chile between 2012-2014 Cornejo *et al.* [54]														
18.5 S	70.3 W	9 m	8.32	6.44	9.54	7.81	5.33	5.29	6.05	6.73	8.03	8.60	7.45	8.06
Las Rejas, Chile 2013-2014 Cornejo *et al.* [54]														
18.3 S	69.5 W	4391m	8.32	7.06	8.35	3.60	3.38	3.35	7.67	3.13	3.13	5.33	5.04	8.93
NASA, Hyderabad, Pakistan between 1983-2005 [55]														
65.4 N	68.3 E	60m	4.25	5.15	6.12	6.84	7.42	7.70	8.28	7.67	6.48	5.62	4.64	4.03

Where Lat. represents latitude positive north/south in degrees, Lon. stands for longitude positive east/west in degrees, Ele. denotes elevation in meters and monthly mean diffuse solar radiation obtained from literature and NASA (same geographical information as study site) are all in $MJm^{-2}day^{-1}$

3. Results and Discussion

In this section, the results of the measured data in the study site were compared with the following: (1) the developed 43 models in this study, (2) five measured data obtained from the literature together with the observed satellite data obtained from the NASA database, and (3) five models obtained from the literature and best performing model (model 42) as presented in Figs. 2 - 5, and their corresponding estimation statistical indicators are presented in Tables 6 – 7.

3.1 Analysis of Monthly and Yearly Solar Radiation Ground Observation

The results of the monthly and annual averages of the study site and the corresponding aggregate mean values for the duration of measurement (2 years) are

presented. It can be seen vividly that the mean monthly and yearly solar radiation and meteorological values for the two years of measurement are presented in Table 2.

The summer season is from March-August whereas the winter season starts in October and ends in January for Hyderabad, Pakistan. The winter months are characterized by overcast, heavy rainfall clouds, heavy frogs, high relative humidity, low temperature, low wind speed and direction, and the highest ambient air pressure as shown in Table 2. This gives rise to minimum values of 14.33 $MJm^{-2}day^{-1}$ and 14.75 $MJm^{-2}day^{-1}$ reported for global and direct solar radiation in the month of January, respectively, whereas the minimum diffuse solar radiation of 5.02 $MJm^{-2}day^{-1}$ was recorded in the month of December as shown in Table 2.

However, summer months are characterized by clear sky, high temperature and wind speed with low relative humidity and ambient air pressure. This culminates into high values of global solar radiation and its component. The maximum value for global solar radiation (24.84 $MJm^{-2}day^{-1}$) occurred in the month of April, direct normal irradiance (20.78 $MJm^{-2}day^{-1}$) occurred in the month of February, and diffuse solar radiation (13.28 $MJm^{-2}day^{-1}$) occurred in the month of July. These results are comparable to the report of Jamil and Akhtar [22-24] in the humid-subtropical climatic region of India.

The yearly averages of direct normal irradiance, global solar radiation and diffuse solar radiation calculated for the period of measurement May 2015-April 2016 are 6430.141 $MJm^{-2}year^{-1}$, and 7593.977 $MJm^{-2}year^{-1}$, respectively. For the interval of May 2015-April 2017, the calculated values of global solar radiation, direct normal irradiance and diffuse solar radiation are 7503.759 $MJm^{-2}year^{-1}$, and 3153.287 $MJm^{-2}year^{-1}$, respectively. While for only year 2016 (January-December), the calculated values of global solar radiation, direct normal irradiance and diffuse solar radiation are 7500.64 $MJm^{-2}year^{-1}$, 6350.196 $MJm^{-2}year^{-1}$, and 3139.756 $MJm^{-2}year^{-1}$, respectively. It could be observed that the yearly global solar radiation is higher than the yearly direct normal irradiance with about 15.2% between May 2015-April 2016, and 18.3% in year 2016 (January-December) as shown in Table 2. This implies that the site is more favorable for the installation of photovoltaic technology or flat solar collectors as the magnitude of direct normal irradiance is below the threshold of 7200 $MJm^{-2}year^{-1}$ in the months of January, June, July, August, November and December as presented in Table 2. It is therefore imperative to note that concentrated solar power should not be considered as a favorable technology in this station.

Avoiding the energy available for the development of solar power technologies in Hyderabad, Pakistan, various other factors and technical aspects reduce the actual use of solar energy captured [54, 56-62].

In Hyderabad, the global solar radiation is significantly higher than the direct normal irradiance as a result of higher attenuation effect of aerosols and water vapor on direct irradiance than the diffuse solar radiation component [54, 62]. Hyderabad is situated by the coast and it is highly affected by a high load of sea salt, and water drops aerosols and water vapor loads as the station is located in the University setting where thousands of people and building structures are located. As a result, atmospheric particles are able to absorb light beams of a specific wavelength. These particles convert electromagnetic radiation into heat and eventually into diffused solar radiation components. So, the direct normal irradiance is obtained from the relation:

$$H_b = H\cos z - H_d \quad (14)$$

where z is the zenith angle and other variables retain their usual meaning.

From equation (14), it is obvious that as the diffuse solar radiation component increases, the direct normal irradiance decreases and finally the global solar radiation remains at the same level.

3.2 Performance Evaluation

Developed models under the three classes of clearness index-based models, sunshine duration-based models and combination of the two predictors using either diffuse fraction or diffuse coefficient are now evaluated and results are shown in Fig. 2.

In clearness index-based models' class, diffuse fraction and diffuse coefficient are developed with only one predictor of the clearness index. Fourteen models are developed, with the restriction of the order of two in each input predictor. This could be attributed to the fact that the higher order equations have increased complexity. The numerous models developed are presented in Table 3a. The statistical indicators such as MBE, MPE, RMSE, RRMSE and R^2 have been evaluated for the developed models in the class. The results of the statistical indicators are presented in Table 6. MBE values lie in the range of -0.01057 to -0.00994 $MJm^{-2}day^{-1}$ with a minimum value observed for model 6 (-0.01057 $MJm^{-2}day^{-1}$). As observed from Table 6, models 1-14 under this class recorded negative values. This implies that models underestimated the measured data. However, the overestimation in the values is significantly small because the magnitude of MBE for this class is observably close to zero. MPE values lie in the range -0.08687 to -0.04886 $MJm^{-2}day^{-1}$ with the minimum value observed for model 13 (-0.08687 $MJm^{-2}day^{-1}$). RMSE values are observed to be small for all the developed models under this class with model 6 registering the minimum value of 0.177211 $MJm^{-2}day^{-1}$). In general, the RMSE range buried between 0.177211 to 0.194205 $MJm^{-2}day^{-1}$. Accordingly, the RRMSE value buried in the range 25.50065 to 28.04482 $MJm^{-2}day^{-1}$ with the minimum value 25.50065 registered for model 6. The coefficient of determination (R^2) has values in the range of 0.931 - 0.937 representing good fit of measured data. The highest value of R^2 was recorded for model 5 and model 13.

Under the sunshine duration-based models, the diffuse fraction and diffusion coefficient models are developed with only one predictor of the sunshine duration parameter. Seventeen models are proposed, with the restriction of the order of two in each input predictor. This is because, the higher order equations demonstrate increased complexity. Hence, several models proposed under this class are presented in Table 3b. From the statistical indicators evaluated under this class, the results are presented in Table 4. MBE value lies in the range of -0.0043 to 0.003714 $MJm^{-2}day^{-1}$ with the minimum value of -0.0043 $MJm^{-2}day^{-1}$ registered for model 26. As observed models 15, 17, 22, 25, 28, 29 and 30 recorded a positive value of MBE, indicating overestimation while the remaining models reported a negative value implying an underestimation. However, the overestimation and underestimation in the values is significantly small since the values of MBE for the proposed models reasonably close to zero. This trend is equally observed for the models developed in the humid-subtropical climate region of India [22]. MPE values lie in the range -0.07466 to 0.005151 $MJm^{-2}day^{-1}$ with the minimum value of -0.07466 $MJm^{-2}day^{-1}$ recorded for model 29. RMSE values recorded small values for all the developed models under this class with the minimum value of 0.134126 $MJm^{-2}day^{-1}$ registered for model 25, from range of values 0.13416 to 0.158558 $MJm^{-2}day^{-1}$. Accordingly, the RRMSE value buried in the range 19.01901 to 23.50345 with the minimum value of 19.01901 reported for model 26. The coefficient of

determination (R^2) has values in the range of 0.943 - 0.961 indicating good fit of the measured data. The highest value of R^2 is reported for models 20-22 and model 25-26.

Table 6. The statistical test indicators of all developed models for estimating the diffuse solar radiation at Hyderabad, Pakistan

Models	MBE	MPE	RMSE	RRMSE	R^2	GPI	Rank
Clearness index-based models							
1	-0.00908	-0.07739	0.192954	27.82833	0.933	-2.2996	43
2	-0.00886	-0.06974	0.178761	25.85036	0.932	-1.6650	19
3	-0.00892	-0.06916	0.179255	25.89493	0.932	-1.7088	20
4	-0.00820	-0.07808	0.179834	26.03971	0.932	-1.7190	21
5	-0.00874	-0.08011	0.188957	27.33110	0.937	-2.1183	38
6	-0.01057	-0.04886	0.177211	25.50065	0.931	-1.8717	29
7	-0.00994	-0.05646	0.177650	25.61745	0.931	-1.5319	14
8	-0.00746	-0.08654	0.178283	25.96952	0.932	-1.6400	17
9	-0.00824	-0.08428	0.187491	27.18009	0.936	-2.0729	36
10	-0.00932	-0.07219	0.190773	27.49131	0.934	-2.2654	41
11	-0.00878	-0.08250	0.194205	28.04482	0.932	-2.2969	42
12	-0.00878	-0.07119	0.179881	25.97848	0.932	-1.7402	23
13	-0.00827	-0.08687	0.189859	27.51315	0.937	-2.1177	37
14	-0.00767	-0.08411	0.178343	25.95240	0.932	-1.5986	14
Sunshine duration-based models							
15	0.00139	-0.05115	0.155966	23.25241	0.946	-2.1489	39
16	-0.00023	-0.04845	0.158277	23.40913	0.948	-1.9851	32
17	-0.00081	-0.06078	0.158309	23.46320	0.948	-1.9760	31
18	-0.00094	-0.03919	0.158589	23.38298	0.947	-1.9916	33
19	-0.00179	-0.03799	0.136359	19.24055	0.958	-1.3733	10
20	-0.00249	-0.01617	0.135120	19.06948	0.961	-1.8065	28
21	-0.00082	-0.04779	0.134612	19.16734	0.961	-1.8027	27
22	0.000452	-0.05150	0.134273	19.15748	0.961	-1.796	26
23	-0.00193	-0.04544	0.139213	19.66207	0.955	-1483	12
24	-0.00216	-0.02825	0.135648	19.13818	0.959	-1.3835	11
25	0.00196	-0.07009	0.134126	19.22668	0.961	-1.7812	25
26	-0.0043	0.005151	0.135586	19.01901	0.961	-1.7549	24
27	-0.00121	-0.03128	0.157561	23.29592	0.948	-1.52144	13
28	0.00079	-0.05283	0.15682	23.31739	0.948	-2.0489	35
29	0.003714	-0.07466	0.155199	23.31988	0.943	-2.2366	40
30	0.001417	-0.06818	0.158558	23.50345	0.947	-1.9659	30
31	-0.00187	-0.02838	0.158044	23.30298	0.948	-2.0032	34
Sunshine duration and clearness index-based models							
32	-0.00191	-0.04025	0.130386	17.70534	0.960	-1.2243	6
33	-0.00279	-0.02738	0.130494	17.57645	0.960	-1.250	7
34	-0.00188	-0.02298	0.110254	14.69178	0.967	-1.1409	4
35	-0.00129	-0.02979	0.10975	14.67827	0.967	-1.1179	3
36	-0.00186	-0.02261	0.109897	14.62919	0.967	-1.081	2
37	-0.00137	-0.04969	0.133455	18.50554	0.957	-1.2583	8
38	-0.00401	-0.01166	0.133968	18.05627	0.958	-1.2925	9
39	-0.00326	-0.00551	0.110418	14.61601	0.967	-1.1671	5
40	-0.00306	-0.02152	0.128539	17.31672	0.961	-1.7221	22
41	-0.00130	-0.04248	0.127048	17.16679	0.961	-1.5506	15
42	**-0.00395**	**0.00349**	**0.109462**	**14.41593**	**0.967**	**-1.0208**	**1**
43	-0.00192	-0.04698	0.135857	18.71394	0.958	-1.6455	18

Under sunshine duration and clearness index-based models, diffuse fraction and diffuse coefficient models are proposed with two predictors. Twelve models are developed, with the restriction of the order of three in each input predictor. This is as a

result of the fact that, the higher order equations have increased complexity. The numerous models developed are presented in Table 3c. From the statistical results, MBE, MPE and RMSE reported similar trends in signaling but varying magnitude as in clearness index-based models. Similar trend was reported for models developed in India [21] indicating that models employing clearness index and those combining clearness index and sunshine duration exhibit similar diurnal fluctuation.

Table 7. Test the best models to the models and measured data obtained from the literature and the NASA database [55]

Model/Site	MBE	MPE	RMSE	RRMSE	R^2	GPI	Rank	Reference
Models from the literature								
Model 23	-0.00193	-0.04544	0.139213	19.66207	0.955	0.2208	1	Present study
Model 44	-0.25264	2.799933	0.875162	116.391	0.953	-10.40736	6	Liu & Jordan [49]
Model 45	-0.22267	2.474549	0.771353	102.8651	0.953	-9.488693	4	Page [25]
Model 46	-0.13464	1.402934	0.466401	58.31886	0.951	-6.066975	3	Iqbal [13]
Model 47	-0.22582	2.494301	0.782266	103.6861	0.954	-9.583763	5	Ibrahim [28]
Model 48	0.063076	-1.03147	0.360443	56.31961	0.891	-0.416833	2	Maduekwu & Chendo [61]
Measured data from the literature together with the data from the NASA database								
Model 23 (best model)	-0.00193	-0.04544	0.139213	19.66207	0.955	0.1338	1	Present study
UTA, Chile	-0.11018	0.445126	0.861782	114.3659	0.376	-3.93826	4	Cornejo *et al.* [54]
Aligarh, India	-0.08497	0.598581	0.459634	57.5258	0.711	-0.848897	2	Jamil & Akhtar [22]
LR, Chile	-0.25168	2.062406	1.182753	153.1898	0.202	-4.854534	5	Cornejo *et al.* [54]
Kerman, Iran	-0.18323	1.938777	0.63473	80.59346	0.624	-3.826472	3	Safaripour & Mehrabian [53]
Hyderabad, Pakistan	-0.20368	2.248962	0.705552	93.48759	0.939	-5.857619	6	NASA Data [55]

Under this section, five (5) empirical models are often used by researchers in the literature, and four (4) measured data obtained equally from the literature and the NASA website were employed to check the applicability of the best models from the 45 proposed models. The results of the statistical indicators evaluated under this section are presented in Table 7. MBE values lie in the range of 0.25264 to 0.063076 on the five models obtained from the literature while the range of MBE on measured data obtained from satellite data from NASA website is -0.25168 to -0.08497. From the resulting matrices, only models 48 [52] have a positive value of MBE which indicates overestimation while the remaining models and measured data have a negative value leading to an underestimation. However, the overestimation and underestimation of these values is significantly small since the values of MBE for each of the proposed models are reasonably close to zero. MPE values lie in the range -1.03147 to 2.799933 and 0.445126 to 2.248962 with a minimum value of -1.03147 and 0.445126 for models from the literature (models 44-48) and measured data obtained from literature together with NASA data, respectively. Base on measured data obtained from the literature together with

NASA data, RMSE values are found to be minimum for model 48 and for Aligarh location India [22], respectively. Also, coefficient of determination (R^2) recorded values in the range of 0.891 to 0.956 and 0.202 to 0.939 with maximum values of 0.956 reported for models 47 [28] and 0.939 for NASA data on models from the literature and measured data together with NASA data, respectively.

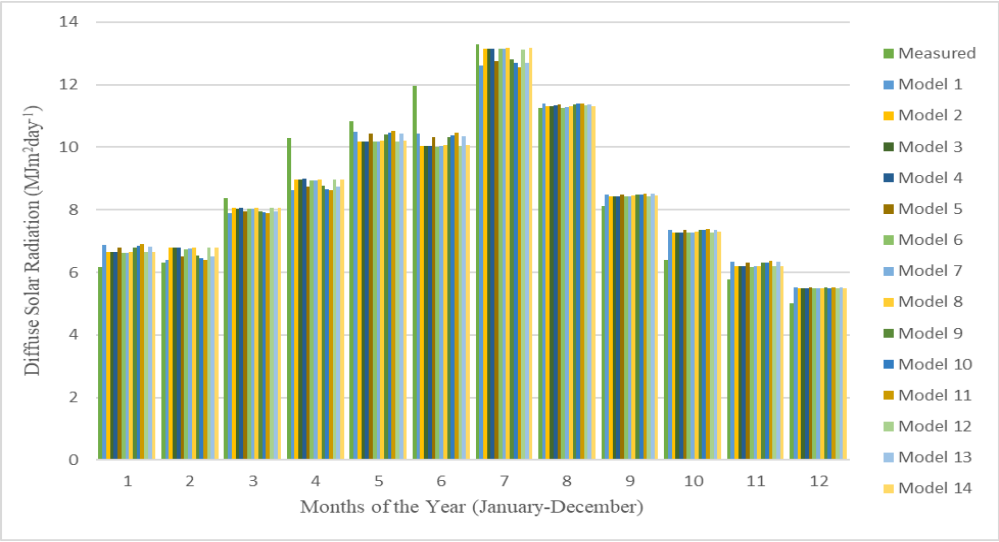

Fig. 2a. Clearness Index-based models for estimating diffuse solar radiation in Hyderabad, Pakistan

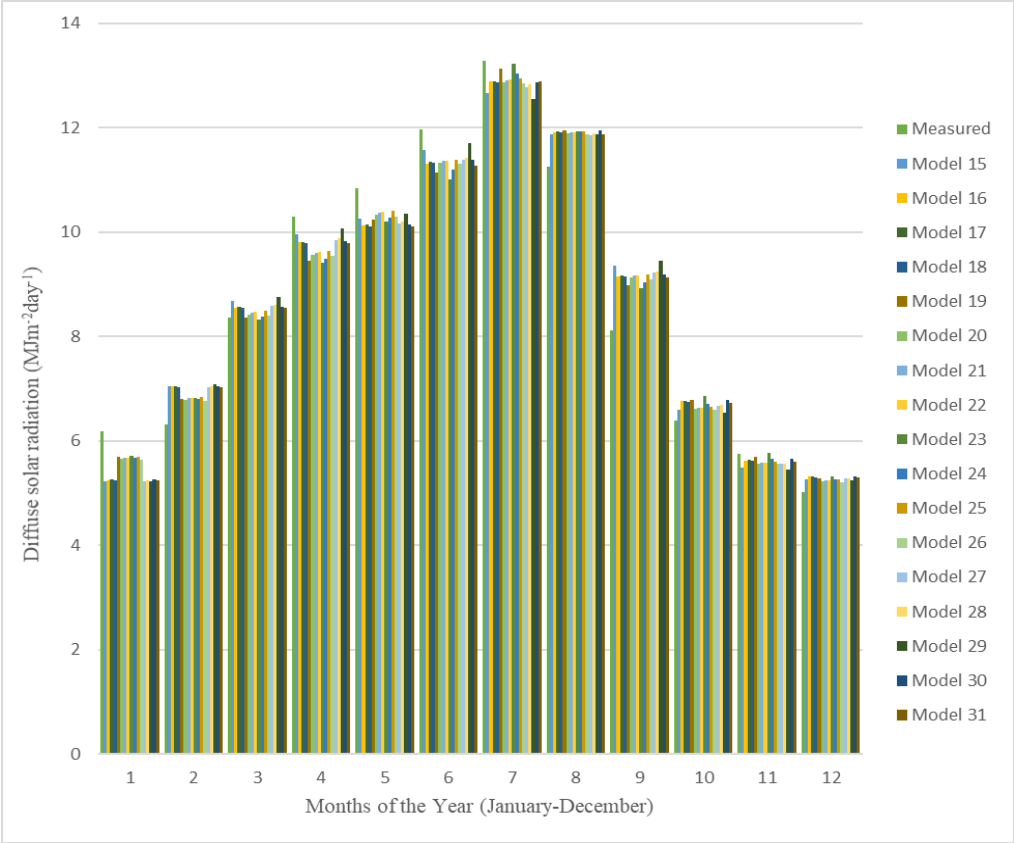

Fig. 2b. Sunshine duration-based models for estimating diffuse solar radiation in Hyderabad, Pakistan

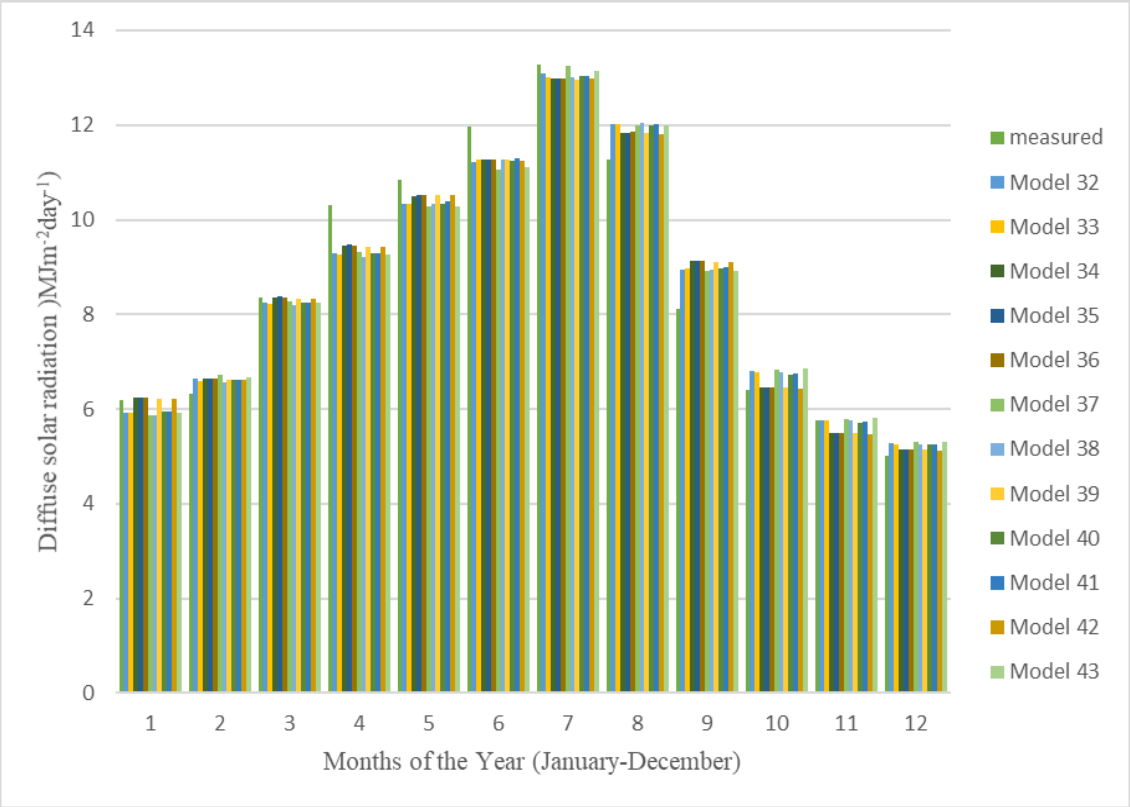

Fig. 2c. Hybrid of sunshine duration and clearness index-based models for estimating diffuse solar radiation in Hyderabad, Pakistan

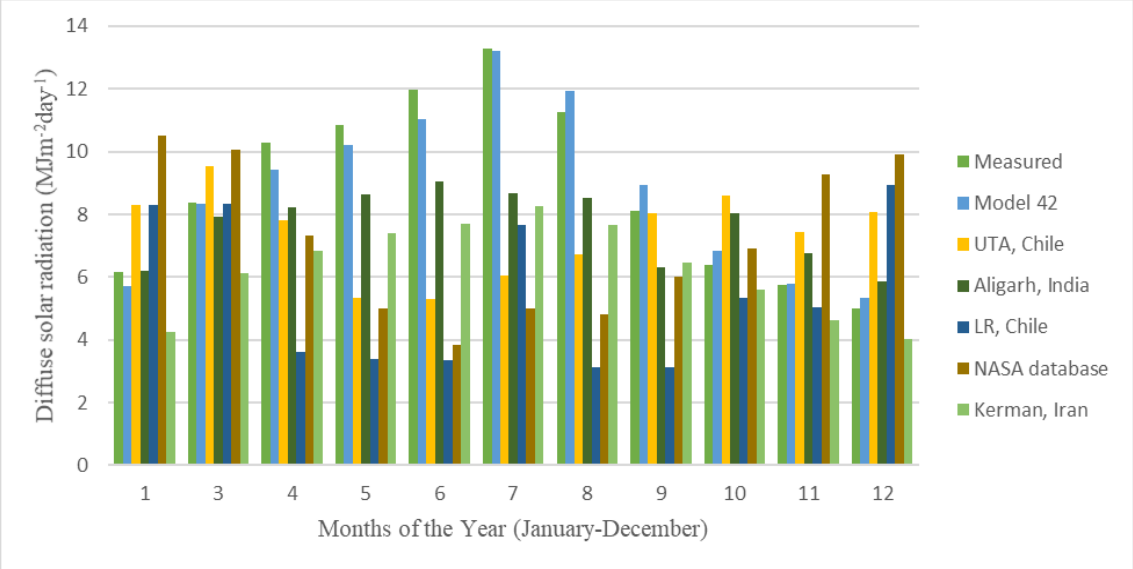

Fig. 3. Comparison between measured data from study site (Hyderabad) and the best performing model (model 42) together with measured the data obtained from the literature and the NASA database

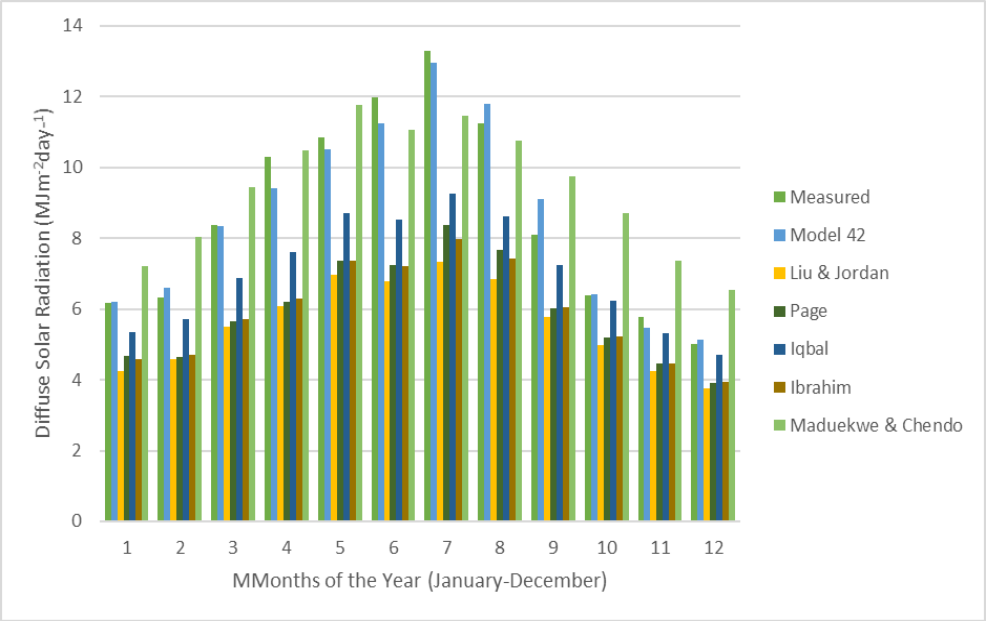

Fig. 4. Comparison between measured data from study site (Hyderabad) and the best performing model (model 42) together with models obtained from the literature

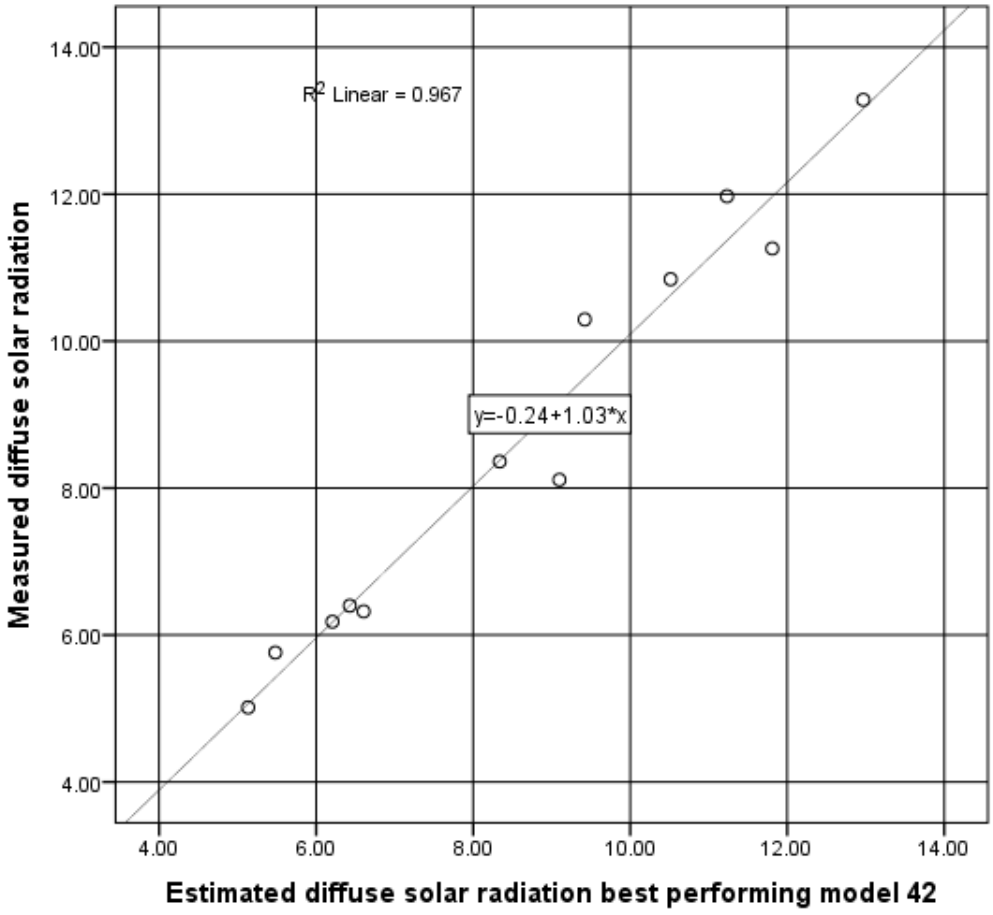

Fig. 5. Meanly mean variations of Hyderabad's best performing model after eliminating models from class 1 – 3 in $MJm^{-2}year^{-1}$

3.3 Global Performance Indicator and Ranking of Models

From the statistical indicators, it can be seen that different models from different classes come together with the models and measured data and satellite data obtained from the NASA database outperformed others. Thus, to avoid this variability and further improve the results of statistical analyses, global performance indicator (GPI) is applied.

As presented in Table 6, the GPI values of the proposed 43 models in this study classified under sunshine duration-based models, clearness index-based models and combination of both models are in the range of -2.2996 to -1.0208. The maximum GPI (-1.0208) and the minimum ranking of models were recorded for model 42 which is a hybrid of sunshine duration and clearness index predictors of variable dependent variable. It can be equally observed in Table 6 that hybrid of sunshine duration and clearness index predictors recorded as the best ranking model. This indicates that model 42 and hybrid of sunshine duration and clearness index predictors yielded the best performing model and class, respectively, in Hyderabad, Pakistan. Similar results were obtained in the literature [6, 20, 24, 41-42, 38-40].

In order to achieve the objective of the study, the best model (model 42) selected using GPI metric was applied to compare with five (5) models and five (5) measured data obtained from the literature and the NASA database. This is to check if the accuracy and applicability of the best model are limited from which the model was developed, as researchers and peers reported that diffuse solar radiation and other components of global solar radiation are dependent on local climate and regional geography.

As presented in Table 7, the maximum GPI and the minimum scores of the five (5) models and five (5) measured data from the literature together with satellite data obtained from the NASA database are compared with the best performing model in Hyderabad, Pakistan station (*i.e.*, model 42). After thorough analysis using statistical indicators, GPI and ranking of models (Table 7), the best model (model 42) can be employed for estimating diffuse solar radiation in Kerman, Iran and Algarh, India while UTA and LR stations located in Chile require local calibration of model 42 to actually fit the measured data. In general, model 42 is best suited to fitt data at stations Aligarh, India followed by Kerman, Iran while other stations such as UTA and LR located in Chile need local calibration to actually fit the measured values in Hyderabad. However, it can be observed that model 42 did not fit the calculated data from the NASA database despite the fact that the data employed for modeling 42 and that of NASA possess the same geographical information. This could be attributed to the fact that NASA data is estimated under 20% error from existing models in the literature and different locations compared to the study site. Also, comparing models 42 with 5 models in the literature revealed that model 42 actually predicted values obtained from Iqbal's model [13] and Maduekwu & Chendo's models [52] while other models such as Liu & Jordan [49], Page [25], and Ibrahim [28] required local calibration to actually fit the values of model 42. On the whole, Iqbal's model is best suited to fit the values of the best performing model in Hyderabad (model 42), followed by Maduekwu & Chendo's model.

4. CONCLUSIONS

The knowledge of diffuse solar radiation is important for the design and development of solar system. In this study, forty-three models were analyzed, which

proposed correlations for the diffuse component of global solar radiation. The performance of these models was compared to measured diffuse solar radiation of Hyderabad station by applying various statistical indicators such as MBE, MPE, RMSE, RRMSE, R^2 and GPI. The diffuse fraction and diffuse coefficient were employed as the dependent variable to correlate with the sunshine duration fraction, clearness index and a combination of them. From the results of the statistical indicators, GPI and ranking of the models, model 42 - a hybrid of sunshine duration and clearness index-based models employing diffuse fraction dependent variable outperformed the remaining models proposed in this study. Moreover, the performance of the best model (model 42) was calculated equally with respect to a set of five (5) models and five (5) measured data of diffuse solar radiation presented in the literature together with satellite data obtained from the NASA database. The developed best model (model 42) in this study recorded favorable accurate results in comparison to these existing models and measured data of diffuse solar radiation in the literature and the NASA database with the lowest statistical indicators. The models were then categorized into rankings in descending GPI values so as to ascertain the best performer. From the results, model 42 recorded the highest value of GPI and was ranked first. Hence, it is concluded that the hybrid of sunshine duration and clearness index-based models of diffuse fraction:

$$\left(\frac{H_d}{H} = 3.459 + 0.886 \left(\exp \frac{S}{S_o} \right) - 9.411 \left(\frac{H}{H_o} \right) + 6.429 \left(\frac{H}{H_o} \right)^2 - 0.870 \left(\exp \frac{S}{S_o} \right)^2 \right)$$

is selected as the most accurate generalized model for estimating solar radiation on the horizontal surface in Hyderabad of Pakistan, other locations such as Aligarh in India, Kerman in Iran, Iqbal's model and Maduekwu and Chendo's model, and in any location with similar climate conditions, in the absence of measured data.

This generalized model can be employed by solar energy engineers in terms of site selection and techno-economic performance quantification of solar energy applications such as photovoltaic technologies.

Nomenclature

$kt=H/H_o$	Monthly average clearness index (dimensionless)
H	Global solar radiation on the horizontal surface ($MJm^{-2}day^{-1}$)
H_o	Monthly extraterrestrial solar radiation on the horizontal surface ($MJm^{-2}day^{-1}$)
S_o	Maximum sunshine duration (hrs)
n	Number of days of the year
I_{SC}	Solar constant in W/m^2
H_d	Monthly mean diffuse solar radiation ($MJm^{-2}day^{-1}$)
T_{ave}	Mean monthly maximum temperature (^oC)
P	monthly mean atmospheric pressure at the site (hPa)
P_o	the standard atmospheric pressure at the sea level (1013 hPa)
S	Monthly mean sunshine hours (hrs)
S/S_o	sunshine fraction (dimensionless)
T_d	Monthly average dew point temperature
RH	Monthly mean relative humidity (%)

Greek Letters

ϕ latitude (degrees)
δ solar declination angle (degrees)
ω_s sunset hour angle (degrees)

ACKNOWLEDGMENTS

The author is grateful to the Energy Sector management Assistance Program power by the World Bank Group for providing the data used in this research. My thanks also go to all the authors cited in this paper for their research works that has made this research possible.

CONFLICTS OF INTEREST

The author declares that there is no conflict of interests regarding the publication of this paper.

REFERENCES

[1] Pandey, C.K., Katiyar, A.K. (2013) Solar radiation: models and measurement techniques, *Journal of Energy*, Article ID 305207. DOI: 10.1155/2013/305207
[2] The Intergovernmental Panel on Climate Change (IPCC), https://www.ipcc.ch/ (accessed on 11/29/2019)
[3] Nwokolo, S.C. (2017) A comprehensive review of empirical models for estimating global solar radiation in Africa. *Renewable and Sustainable Energy Reviews*, 78, 955-995.
[4] Mohanty, S., Patra, P.K., Sahoo, S.S. (2016) Prediction and application of solar radiation with soft computing over traditional and conventional approach – A comprehensive review. *Renewable and Sustainable Energy Reviews*, 56, 778-796.
[5] Besharat, F., Dehghan, A., Faghih, A.R. (2013) Empirical models for estimating global solar radiation: A review and case study. *Renewable and Sustainable Energy Reviews*, 21, 798-821.
[6] Khorasanizadeh, H., Mohammadi, K. (2016) Diffuse solar radiation on a horizontal surface: Reviewing and categorizing the empirical models. *Renewable and Sustainable Energy Reviews*, 53, 338-362.
[7] Thirugnanasambabdam, M., Iniyan, S., Goic, A. (2010) A review of solar thermal technologies. *Renewable and Sustainable Energy Reviews*, 14, 312-322.
[8] Ullah, K.R., Saidur, R., Piing, H.W., Akikur, R.K., Shouvo, N.H. (2013) A review of solar thermal refrigeration and cooling methods. *Renewable and Sustainable Energy Reviews*, 24, 499-513.

[9] Bailek, N., Bouchouicha, K., Al-Mostafa, Z., El-Shimy, M., Aoun, N., Slimani, A., Al-Shehri, S. (2018) A new empirical model for forecasting the diffuse solar radiation over Sahara in the Algerian Big South. *Renewable Energy,* 117, 530-537.
[10] Lorenzo, E. (1994) *Solar electricity: Engineering of photovoltaic systems*. Earthscan/James & James.
[11] Bouzid, Z., Ghellai, N. (2015) Estimation of solar radiation on inclined surface and design method for an autonomous photovoltaic system. Application to Algeria, in *2015 3rd International Renewable and Sustainable Energy Conference (IRSEC), IEEE*, pp. 1-6.
[12] Khorasanizadeh, H., Mohammedi, K., Mostafaeipour, A. (2014) Establishing a diffuse solar radiation model for determining the optimum tilt angle of solar surfaces in Tabass, Iran. *Energy Conversion and Management*, 78, 805-814.
[13] Iqbal, M. (1979) A study of Canadian diffuse and total solar radiation data-monthly average daily horizontal radiation. *Solar Energy,* 22, 81-86.
[14] Erbs, D., Klein, S., Duffie, J. (1982) Estimation of the diffuse radiation fraction for hourly, daily and monthly-average global solar radiation. *Solar Energy*, 28, 293-302.
[15] Sabbagh, J., Sayigh, A., El-Salam, E. (1977) Estimation of the total radiation from meteorological data. *Solar Energy*, 19, 307-311.
[16] De Miguel, A., Bilbao, J., Aguiar, R., Kambezidis H, Negro E. (2001) Diffuse solar irradiation model evaluation in the North Mediterranean belt area. *Solar Energy*, 70, 143-153.
[17] Paliatsos, A., Kambezidis, H., Antoniou, A. (2003) Diffuse solar radiation at a location in the Balkan Peninsula. *Renewable Energy*, 28, 2147-2156.
[18] Li, H., Bu, X., Lian, Y., Zhao, L., Ma, W. (2012) Further investigation of empirically derived models with multiple prediction in estimating monthly average daily diffuse solar radiation over China. *Renewable Energy*, 44, 469-473.
[19] Tasdemiroglu, E., Server, R. (1991) Estimation of monthly average daily horizontal diffuse radiation in Turkey. *Energy*, 16, 787-790.
[20] Li, H., Ma, W., Wang, X., Lian, Y. (2011) Estimating monthly average daily diffuse solar radiation with multiple predictors: a case study. *Renewable Energy,* 36, 1944-1948.
[21] Jamil, B., Siddiqui, A.T. (2015) Generalized models for estimation of diffuse solar radiation based on clearness index and sunshine duration in India: Applicability under different climate zones. *Journal of Atmospheric and Solar-Terrestrial Physics*, 157-158, 16-34.
[22] Jamil, B., Akhtar, N. (2017) Estimation of diffuse solar radiation in humid-subtropical climate region of India: comparison of diffuse fraction and diffusion coefficient models. *Energy*, 131, 149-164.
[23] Jamil, B., Akhtar, N. (2017) Empirical models for estimation of diffuse solar radiation based on measured data for humid-subtropical climatic region of India. *Journal of Renewable and Sustainable Energy*, 9, 033702. DOI: 10.1063/1.4983177
[24] Jamil, B., Akhtar, N. (2017) Comparison off empirical models to estimate monthly mean diffuse solar radiation from measured data: case study for humid-subtropical climatic region of India. *Renewable and Sustainable Energy Reviews,* 77, 1326-1342.
[25] Page, J.K. (1961) The estimation of monthly mean values of daily total short-wave radiation on vertical and inclined surfaces from sunshine records for latitude 40N – 40S, in *Proceedings of UN Conference on New Sources of Energy*, pp. 378-390.

[26] Angstrom, A. (1924). Solar and terrestrial radiation. *Quarterly Journal of Royal Meteorological Society*, 50, 121-5.
[27] Barbaro, S., Cannata, G., Coppolino, S., Leone, C., Sinagre, E. (1981) Diffuse solar radiation statistics for Italy. *Solar Energy*, 26, 429-435.
[28] Ibrahim, S.M.A. (1985) Diffuse solar radiation in Cairo, Egypt. *Energy Conversion and Management*, 25, 69-72.
[29] Orgill, J.F., Hollands, K.G.T. (1977) Correlation equation for hourly diffuse radiation on a horizontal surface. *Solar Energy*, 19, 357-359.
[30] Tiris, M., Tiris, C., Ture, I.E. (1996) Correlations of monthly-average daily global, diffuse and beam radiations with hours of bright sunshine in Gebze, Turkey. *Energy Conversion and Management*, 37, 1417-1421.
[31] Nfaoui, H., Buret, J. (1993) Estimation of daily and monthly direct, diffuse and global solar radiation in Rabat (Moricco). *Renewable Energy*, 3, 923-930.
[32] El-Sebaii, A., Al-Hazmi, F., Al-Ghamdi, A., Yaghmour, S.J. (2010) Global, direct and diffuse solar radiation on horizontal and tilted surfaces in Jeddah, Saudi Arabia. *Applied Energy*, 87, 568-576.
[33] Jain, P. (1990) A model for diffuse and global irradiation on horizontal surfaces. *Solar Energy*, 45, 301-308.
[34] Khogali, A., Ramadan, M., Ali, Z., Fattah Y. (1983) Global and diffuse solar irradiation in Yemen (YAR). *Solar Energy*, 31, 55-62.
[35] Said, R., Mansor, M., Abuain, T. (1998) Estimation of global and diffuse radiation at Tripoli. *Renewable Energy*, 14, 221-227.
[36] Boukelia, T.E., Mecibah, M.S., Meriche, I.E. (2014) General models for estimation of the monthly mean daily diffuse solar radiation (case study: Algeria). *Energy Conversion and Management*, 81, 211-219.
[37] Nwokolo, S.C. & Ogbulezie, J.C. (2018)A qualitative review of empirical model for estimating diffuse solar radiation from experimental data in Africa. *Renewable and sustainable Energy Reviews*, 92, 353-393
[38] Jiang, Y. (2009) Estimation of monthly mean daily diffuse radiation in China. *Applied Energy*, 86, 1458-1464.
[39] Trabea, A.A. (1999) A multiple linear correlation for diffuse radiation from global solar radiation and sunshine data over Egypt. *Renewable Energy*, 17, 411-420.
[40] Gopinathan, K., Soler, A. (1999) Diffuse radiation models and monthly-average, daily, diffuse data for a wide latitude range. *Energy*, 20, 657-667.
[41] Elminir, H.K., Azzam, Y.A., Younes, F.J. (2007) Prediction of hourly and daily diffuse fraction using neural network as compared to linear regression models. *Energy*, 32, 1513-1523.
[42] Despotovic, M., Nedic, V., Despotovic, D., Cvetanovic, S. (2016) Evaluation of empirical models for predicting monthly mean horizontal diffuse solar radiation. *Renewable and Sustainable Energy Reviews*, 56, 246-260.
[43] Ahmad, A., Khan, N.A. (2014) Renewable Energy Resource Mapping of Pakistan. https://www.esmap.org/sites/esmap.org/files/ESMAP_SAR_EAP_Renewable_Energy_Resource_Mapping_Pakistan.pdf (accessed on 12/1/2019)
[44] Stökler, S. and Schillings, C. (2015) *Solar Modeling Report Pakistan #1*, World Bank Group, Washington DC, USA. http://documents.worldbank.org/curated/en/200771468096863184/pdf/95710-REVISED-ESM.pdf (accessed on 12/1/2019)

[45] Pakistan – Solar radiation measurement data (2014-2017), https://africaopendata.org/dataset/pakistan-solar-measurement-wbg-esmap (accessed on 12/1/2019)
[46] International Water Management Institute, http://www.iwmi.cgiar.org/ (accessed on 12/1/2019)
[47] Yaniktepe, B., Genc, Y.A. (2015) Estimating new model for predicting the global solar radiation on horizontal surface. *International Journal of Hydrogen Energy*, 40, 15278-15283.
[48] Mohandes, M., Balghonaim, A., Kassas, M., Rehman, S., Halawani, T.O. (2000) Use of radial basis function for estimating monthly mean daily solar radiation. *Solar Energy*, 68, 161-168.
[49] Liu, B.Y.H, Jordan, R.C. (1960) The interrelationship and characteristics distribution of direct, diffuse and total solar radiation. *Solar Energy*, 4, 1-4.
[50] Nwokolo, S.C., Ogbulezie, J.C. (2018) A qualitative review of empirical models for estimating diffuse solar radiation from experimental data in Africa. *Renewable & Sustainable energy Reviews*, 92, 353-393.
[51] Despotovic, M., Nedic, V., Despotvic, D., Cvetanovic, S. (2015) Review and statistical analysis of different global solar radiation sunshine models. *Renewable and Sustainable Energy Reviews*, 52, 1868-1880.
[52] Maduekwe, A.A., Chendo, M.A.C. (1995) Predicting the component of the total hemispherical solar radiation from sunshine duration measurement in Lagos, Nigeria. *Renewable Energy*, 6, 807-812.
[53] Safaripour, M.H., Mehrabian, M.A. (2011) Predicting the direct, diffuse, and global solar radiation on a horizontal surface and comparing with real data. *Heat Mass Transfer*, 47, 1537-1551.
[54] Cornejo, L., Martin-Pornares, L., Alarcon, D., Blanco, J., Polo, J. (2017) A thorough analysis of solar irradiation measurements in the region of Rrica Parinacota, Chile. *Renewable Energy*, 112, 1197-208.
[55] National Aeronautics and Space Administration, https://www.nasa.gov/ (accessed on 12/1/2019)
[56] Liu, M., Tay, N.H.S., Bell, S., Belusko, M., Jacob, R., Will, G., Saman, W., Bruno, F. (2016) Review on concentrated solar power plants and new development in high temperature thermal energy storage technologies. *Renewable and Sustainable Energy Reviews*, 53, 1411-1432.
[57] Zhang, H.L., Baeyens, J., Degreve, J., Caceres, G. (2013) Concentrated solar power plants: review and design methodology. *Renewable and Sustainable Energy Reviews*, 22, 466-481.
[58] Zondag, H.A. (2008) Flat-plate PV-thermal collectors and systems: a review. *Renewable and Sustainable Energy Reviews*, 12, 891-959.
[59] Singh, G.K. (2013) Solar power generation by PV (photovoltaic) technology: a review *Energy*, 53, 1-13.
[60] Dubey, S., Sarvaiya, J.N., Seshadri, B. (2013) Temperature dependent photovoltaic (pv) efficiency and its effect on PV production in the world – a review. *Energy Procedia*, 33, 311-321.
[61] Jordehi, A.R. (2016) Parameter estimation of solar photovoltaic (PV) cells: a review. *Renewable and Sustainable Energy Reviews*, 61, 354-371.
[62] Polo, J., Estalayo, G. (2015) Impact of atmospheric aerosol loads on concentrated solar power production in arid-desert sites. *Solar Energy*, 115, 621-631.

CALL FOR PAPERS

Trends in Renewable Energy

ISSN Print: 2376-2136 ISSN online: 2376-2144

http://futureenergysp.com/index.php/tre/

Trends in Renewable Energy (TRE) is an open accessed, peer-reviewed semi-annual journal publishing reviews and research papers in the field of renewable energy technology and science. The aim of this journal is to provide a communication platform that is run exclusively by scientists. This journal publishes original papers including but not limited to the following fields:

- ✧ Renewable energy technologies
- ✧ Catalysis for energy generation, Green chemistry, Green energy
- ✧ Bioenergy: Biofuel, Biomass, Biorefinery, Bioprocessing, Feedstock utilization, Biological waste treatment,
- ✧ Energy issues: Energy conservation, Energy delivery, Energy resources, Energy storage, Energy transformation, Smart Grid
- ✧ Environmental issues: Environmental impacts, Pollution
- ✧ Bioproducts
- ✧ Policy, etc.

We publish the following article types: peer-reviewed reviews, mini-reviews, technical notes, short-form research papers, and original research papers.

The article processing charge (APC), also known as a publication fee, is fully waived for the Trends in Renewable Energy.

Call for Editorial Board Members

We are seeking scholars active in a field of renewable energy interested in serving as volunteer Editorial Board Members.

Qualifications

Ph.D. degree in related areas, or Master's degree with a minimum of 5 years of experience. All members must have a strong record of publications or other proofs to show activities in the energy related field.

If you are interested in serving on the editorial board, please email CV to editor@futureenergysp.com.